

Shear Strength of Short Shear-Critical Reinforced Concrete Columns

By

Omar Shemy

April 2021



Department of Civil Engineering
McGill University, Montréal

A thesis submitted to McGill University in partial fulfillment of the requirements of the degree
of Master of Engineering

© Omar Shemy, 2021

Abstract

This research program was aimed at investigating the adequacy of the shear design provisions in North America regarding the reliable estimation of the shear strength of shear-critical short columns. Four short columns, each with different amounts of shear reinforcement, were tested under monotonic loading and a constant axial compressive load. Additionally, the observed column responses were compared with three types of prediction models: sectional analyses, truss-and-arch models, and non-linear finite element analyses. It was concluded that the use of sectional design models resulted in conservative predictions. Models considering the formation of concrete strut action gave very good predictions. Non-linear finite element analyses gave the most accurate predictions of the shear strength of the columns and also provided predictions of the complete behaviour. The strut or arch effect is an important phenomenon for reinforced concrete columns with small aspect ratios or high axial loads. It was determined that sectional design models can be adjusted to capture the effect of strut action in short columns.

Résumé

Ce programme de recherche visait à étudier l'adéquation des dispositions de conception de cisaillement en Amérique du Nord en ce qui concerne l'estimation fiable de la résistance au cisaillement des colonnes courtes critiques au cisaillement. Quatre colonnes courtes, chacune avec différentes quantités d'armature de cisaillement, ont été testées sous une charge monotone et une charge de compression axiale constante. De plus, les réponses des colonnes observées ont été comparées à trois types de modèles de prédiction: les analyses en coupe, les modèles en treillis et en arc et les analyses par éléments finis non linéaires. Il a été conclu que l'utilisation de modèles de conception en coupe a donné lieu à des prédictions prudentes. Les modèles prenant en compte la formation d'une action de jambe de force concrète ont donné de très bonnes prévisions. Les analyses par éléments finis non linéaires ont donné les prédictions les plus précises de la résistance au cisaillement des poteaux et ont également fourni des prédictions du comportement complet. L'effet d'entretoise ou d'arc est un phénomène important pour les poteaux en béton armé avec de petits rapports d'aspect ou des charges axiales élevées. Il a été déterminé que les modèles de conception en coupe peuvent être ajustés pour capturer l'effet de l'action des jambes de force dans de courtes colonnes.

Acknowledgements

The research in this thesis would have taken far longer to complete without the encouragement from many others. It is a delight to acknowledge those who have supported me over the last two years.

First and foremost, the author would like to thank Professor Denis Mitchell, thank you, genuinely, for your mentorship, guidance and for always leading by example. Thank you for your encouragement and support throughout the course of this research. The author would also like to thank Dr. William D. Cook for his considerable assistance to this research program, especially throughout the experimental and analysis phase.

Many thanks to Rico Massa for his valuable assistance during all aspects of the construction and testing of the columns, his eagerness to help and above all being a great friend. The help provided by Asher Collins, Jacob Burke and Mairvat Amin was also invaluable. Appreciation is also extended to John Bartczak and William Boyd Dumais for their assistance.

To Mom and Dad, thank you, for investing in me your lifetime, and doing everything in your capacity to give me the best education possible, since day one. I hope I pay back a fraction of the constant love and support you surround me with, by making you proud.

To all my friends, thank you for the unconditional love.

The financial assistance provided by McGill University and NSERC throughout this research program was greatly appreciated.

Table of Contents

ABSTRACT	II
RÉSUMÉ	III
ACKNOWLEDGEMENTS	IV
TABLE OF CONTENTS	V
LIST OF FIGURES	VIII
LIST OF TABLES	XI
1 INTRODUCTION	1
1.1 Problem Description	1
1.2 Previous Research	4
1.3 Research Objectives	5
1.4 Outline of the Thesis	5
2 LITERATURE REVIEW AND PREVIOUS RESEARCH	7
2.1 Modified Compression Field Theory (MCFT)	7
2.1.1 Background	7
2.1.2 MCFT	8
2.2 Sectional Design Models	11
2.2.1 Canadian Highway Bridge Design Code (CSA, 2019)	12
2.2.2 Response 2000	14
2.2.3 ACI Committee 318 (2019) Code Equations	14
2.3 Non-Linear Finite Element Analysis	16
2.3.1 VecTor2	16
2.3.2 Crack Widths and Spacing	17
2.4 Previous Research	18
2.4.1 Watanabe and Ichinose (1991)	18
2.4.2 Truss and Strut Model by Priestley et al. (1994)	20
2.4.3 Truss-Arch Model by Pan and Li (2013)	22
3 EXPERIMENTAL PROGRAM	28

3.1 Introduction	28
3.2 Details of Specimens	28
3.2.1 Geometric Design	28
3.2.2 Reinforcing Steel Design.....	29
3.2.3 Specimen M1	32
3.2.4 Specimen M2	33
3.2.5 Specimen M3	34
3.2.6 Specimen M4	35
3.3 Construction.....	36
3.4 Material properties	38
3.4.1 Concrete.....	38
3.4.2 Reinforcing Steel	40
3.5 Test Setup and Instrumentation	42
3.5.1 Test Setup	43
3.5.2 Instrumentation	47
3.6 Experimental Procedure	53
4 EXPERIMENTAL RESULTS.....	54
4.1 Introduction	54
4.2 Response of Specimen M1.....	55
4.2.1 Shear-Deflection Response	55
4.2.2 Shear Failure	57
4.2.3 Crack Widths	59
4.2.4 Measured Strains	61
4.3 Response of Specimen M2.....	67
4.3.1 Shear-Deflection Response	67
4.3.2 Shear Failure	69
4.3.3 Crack Widths	71
4.3.4 Measured Strains	73
4.4 Response of Specimen M3.....	79
4.4.1 Shear-Deflection Response	79
4.4.2 Shear Failure	81
4.4.3 Crack Widths	83
4.4.4 Measured Strains	85
4.5 Response of Specimen M4.....	91
4.5.1 Shear-Deflection Response	91
4.5.2 Shear Failure	93
4.5.3 Crack Widths	95
4.5.4 Measured Strains	97
5 ANALYSIS OF RESULTS	103

5.1 Discussion and Comparison of Experimental Results	103
5.1.1 Shear-Deflection Responses.....	103
5.1.2 Crack Widths	104
5.2 Predicted Shear Capacities from Sectional Analyses	108
5.2.1 Shear Resistance Predicted Using Canadian Highway Bridge Design Code	108
5.2.2 Shear Resistance Predicted Using Response 2000	111
5.2.3 Shear Resistance Predicted Using ACI Committee 318 (2019) Provisions	113
5.2.4 Comparison of Shear Resistance Predictions from Sectional Design Models	114
5.3 Predicted Behaviour from Truss and Strut or Arch Models.....	115
5.3.1 Approach of Priestley et al. (1994)	115
5.3.2 Truss-Arch Model by Pan and Li (2013).....	116
5.3.3 CHBDC General Method with Concrete Strut	118
5.3.4 Comparison of Shear Resistance Predictions from Truss and Strut Models	120
5.4 Shear Response Predicted using Non-Linear Finite Element Analysis	122
5.4.1 Finite Element Model	122
5.4.2 Comparison with Experimental Results	125
5.5 Experimental and Prediction Shear Strength Summary	129
6 CONCLUSIONS	132
REFERENCES	133

List of Figures

Figure 1.1: Damaged Column during 1995 Kobe Earthquake (Yoshimura and Nakamura, 2003)	2
Figure 1.2: Shear failure of bridge column in the 2010 Chile Earthquake (Mitchell et al., 2011)	2
Figure 2.1: Equations of modified compression field theory (Bentz and Collins, 2006)	8
Figure 2.2: Simplified diagonal crack widths compared to MCFT (Bentz and Collins, 2006)	10
Figure 2.3: The CSA A23.3 2004 theta equation compared to upper and lower bounds	11
Figure 2.4: Free body diagram of shear resistance components (Bentz and Collins, 2006)	12
Figure 2.5: The ACI 45° truss model.....	14
Figure 2.6: Truss-arch model by Ichinose (1992): (a) truss model; (b) arch	18
Figure 2.7: Degradation factor with displacement ductility (Priestley et al., 1994)	20
Figure 2.8: Contribution of axial force to column shear strength (Priestley et al., 1994).....	21
Figure 2.9: Variable angle truss model (Pan and Li, 2013)	23
Figure 2.10: Critical section (Pan and Li, 2013)	24
Figure 2.11: Arch model, columns with fixed-fixed ends.....	26
Figure 3.1: Geometry of column specimens	28
Figure 3.2: Detailing of typical column cross section.....	29
Figure 3.3: Detailing of specimen M1	32
Figure 3.4: Reinforcing steel of specimen M1	32
Figure 3.5: Detailing of specimen M2	33
Figure 3.6: Reinforcing steel for specimen M2	33
Figure 3.7: Detailing of specimen M3	34
Figure 3.8: Reinforcing steel for specimen M3	34
Figure 3.9: Detailing of specimen M4	35
Figure 3.10: Reinforcing steel for specimen M4	35
Figure 3.11: Placing of wall reinforcement cage above formwork for final assembly	36
Figure 3.12: Specimens M1 and M2 in formwork before casting	37
Figure 3.13: Casting of specimens	37
Figure 3.14: Casting of cylinders.....	37
Figure 3.15: Typical concrete compressive stress-strain relationships for batch 1 and 2	40
Figure 3.16: Typical tensile stress-strain relationships for reinforcing bars	41
Figure 3.17: Illustration of McGill University testing frame	44
Figure 3.18: Photograph of McGill University custom testing frame.....	45
Figure 3.19: Column in upright position	46
Figure 3.20: Deformation of a column test specimen.....	46
Figure 3.21: Load cell locations.....	47
Figure 3.22: LVDT and string potentiometer locations	49
Figure 3.23: LVDT schematics closeup	50
Figure 3.24: Typical LVDT configuration for specimens M2, M3 and M4	50
Figure 3.25: LVDT configuration for specimen M1	51
Figure 3.26: Strain gauge configuration for M1 (left) and M2 (right)	52
Figure 3.27: Strain gauge configuration for M3 (left) and M4 (right)	52
Figure 4.1: Shear versus deflection response of specimen M1	56
Figure 4.2: Axial load versus applied shear for specimen M1.....	57
Figure 4.3: Shear failure of specimen M1	58
Figure 4.4: Specimen M1 in final displaced position	58
Figure 4.5: Shear versus maximum crack widths for west side of specimen M1.....	59
Figure 4.6: Shear versus maximum crack widths for east side of specimen M1	60

Figure 4.7: Crack pattern and widths at a shear of 225 kN for specimen M1.....	60
Figure 4.8: Crack pattern and widths at peak shear of 339 kN for specimen M1.....	61
Figure 4.9: Shear versus strain for transverse hoops in specimen M1	62
Figure 4.10: Shear versus strain for top longitudinal bar in specimen M1	63
Figure 4.11: Shear versus strain for bottom longitudinal bar in specimen M1	63
Figure 4.12: Average bar elongation strains for specimen M1	64
Figure 4.13: Principal strain and angle from specimen M1 rosette	65
Figure 4.14: Shear versus deflection response of specimen M2	68
Figure 4.15: Axial load versus applied shear for specimen M2.....	69
Figure 4.16: Shear failure of specimen M2	70
Figure 4.17: Specimen M2 in final displaced position	70
Figure 4.18: Shear versus maximum crack widths for west side of specimen M2.....	71
Figure 4.19: Shear versus maximum crack widths for east side of specimen M2	72
Figure 4.20: Crack pattern and widths at a shear of 226 kN for specimen M2.....	72
Figure 4.21: Crack pattern and widths at a shear of 363 kN for specimen M2.....	73
Figure 4.22: Shear versus strain for transverse hoops in specimen M2	74
Figure 4.23: Shear versus strain for top longitudinal bar in specimen M2	75
Figure 4.24: Shear versus strain for bottom longitudinal bar in specimen M2	75
Figure 4.25: Average bar elongation strains for specimen M2	76
Figure 4.26: Principal strain and angle from specimen M2 rosettes	77
Figure 4.27: Shear versus deflection of specimen M3.....	80
Figure 4.28: Applied load versus applied shear for specimen M3	81
Figure 4.29: Shear failure of specimen M3	82
Figure 4.30: Specimen M3 in final displaced position	82
Figure 4.31: Shear versus maximum crack widths for west side of specimen M3.....	83
Figure 4.32: Shear versus maximum crack widths for east side of specimen M3	84
Figure 4.33: Crack pattern and widths at a shear of 242 kN for specimen M3.....	84
Figure 4.34: Crack pattern and width at a shear of 384 kN for specimen M3	85
Figure 4.35: Shear versus strain for transverse hoops in specimen M3	86
Figure 4.36: Shear versus strain for top longitudinal bar in specimen M3	87
Figure 4.37: Shear versus strain for bottom longitudinal bar in specimen M3	87
Figure 4.38: Average bar elongation strains for specimen M3.....	88
Figure 4.39: Principal strain and angle from specimen M3 rosettes	89
Figure 4.40: Shear versus deflection of specimen M4.....	92
Figure 4.41: Applied load versus applied shear for specimen M4	93
Figure 4.42: Shear failure of specimen M4	94
Figure 4.43: Specimen M4 in final displaced position	94
Figure 4.44: Shear versus maximum crack widths for west side of specimen M4.....	95
Figure 4.45: Shear versus maximum crack widths for east side of specimen M4	96
Figure 4.46: Crack pattern and widths at a shear of 226 kN for specimen M4.....	96
Figure 4.47: Crack pattern and width at shear of 417 kN for specimen M4.....	97
Figure 4.48: Shear versus strain for transverse hoops in specimen M4	98
Figure 4.49: Shear versus strain for top longitudinal bar in specimen M4	99
Figure 4.50: Shear versus strain for bottom longitudinal bar in specimen M4	99
Figure 4.51: Average bar elongation strains for specimen M4	100
Figure 4.52: Principal strain and angle from specimen M4 rosettes	101
Figure 5.1: Shear-deflection responses of column specimens.....	103
Figure 5.2: Shear versus maximum shear crack width for specimens M2, M3 and M4	105
Figure 5.3: Shear versus maximum shear crack widths for specimens M1, M2, M3 and M4.....	105
Figure 5.4: Shear crack patterns at maximum shear	106
Figure 5.5: Maximum flexural crack widths, west end (top) east end (bottom)	107

Figure 5.6: Response 2000 predictions for column M1, input data (top), predicted response (bottom).....	112
Figure 5.7: Comparison of predictions made by sectional analysis methods	114
Figure 5.8: Idealized concrete strut for a typical specimen tested in this series	118
Figure 5.9: Response 2000 flexural analysis	119
Figure 5.10: Comparison of the different truss and arch prediction models.....	121
Figure 5.11: Photograph of McGill University testing frame	124
Figure 5.12: Finite element model for the column specimens	124
Figure 5.13: Predicted deflected shape and crack pattern of specimen M3 at predicted maximum shear	125
Figure 5.14: Comparison between VecTor2 predictions and experimentally determined shear deflection responses	126
Figure 5.15: VecTor2 predicted crack widths for all specimens at a shear of $0.8V_{test}$	128
Figure 5.16: Comparison of experimental values and all prediction shear strengths models.....	130

List of Tables

Table 3.1: Summary of transverse reinforcement in column specimens	30
Table 3.2: Ready-mix concrete proportions.....	38
Table 3.3: Expected ready-mix concrete properties	38
Table 3.4: Concrete material properties.....	39
Table 3.5: Reinforcing bar material properties	41
Table 4.1: Shear-deflection response of specimen M1.....	55
Table 4.2: Shear-deflection response of specimen M2.....	67
Table 4.3: Shear-deflection response of specimen M3.....	79
Table 4.4: Shear-deflection response of specimen M4.....	91
Table 5.1: Comparison of peak shears and deflections of column specimens (hoop spacings given in brackets) ...	104
Table 5.2: Comparison of predicted shear capacities using CHBDC general method with shear achieved during testing	110
Table 5.3: Comparison of predicted shear capacities using CHBDC simplified method with shear achieved during testing	111
Table 5.4: Response 2000 nominal shear predictions compared to maximum experimental shears	112
Table 5.5: Comparison of predicted shear capacities using ACI (ACI Committee 318, 2019) with maximum shear achieved during testing.....	114
Table 5.6: Comparison of predicted shear capacities using the approach of Priestley et al. (1994)	116
Table 5.7: Comparison of predicted shear capacities using the approach of Pan and Li (2013)	117
Table 5.8: Comparison of neutral axis depth	119
Table 5.9: Comparison of predicted shear capacities using CHBDC (CSA, 2019) general method with the superimposed concrete strut.....	120
Table 5.10: Models used in VecTor2	123
Table 5.11: Comparison of predicted shear capacities from VecTor2 with shear capacities achieved during testing	125
Table 5.12: Crack width predictions versus observed at $0.8V_{\text{test}}$ for all specimens	127
Table 5.13: Experimental and prediction shear strengths of the specimens.....	129

1 Introduction

1.1 Problem Description

The design of reinforced concrete members such as columns is generally done within the framework of standardized design codes. The main purpose of these design codes is to provide requirements for the design of safe and economical structures. However, no relevant code requirements are available for the design of short, shear-critical, reinforced concrete columns. Many bridges have short columns due to the presence of ramps and valley crossings. Short columns are also present in some reinforced concrete frame buildings due to the presence of architectural features and sloping ground.

Although designers attempt to avoid the presence of short columns there are many situations where this is not possible. It is important to develop a method for assessing the shear strength of short columns that resist lateral loads due to wind and earthquake effects. Reinforced concrete short columns have small shear span-to-depth ratios and relatively high lateral stiffness and are typically governed by brittle shear failures. Due to their high stiffness short columns attract large lateral forces during earthquakes and are often among the first members to fail. If the columns do not have appropriate shear strength, they will lose their load carrying capacity at small lateral deformations and a catastrophic collapse of the structure may occur. Figure 1.1 shows the brittle shear failure of a short column in a building that was subjected to the 1995 Kobe earthquake (Yoshimura and Nakamura, 2003). The presence of a relatively deep beam at the top of the column along with a wall at the base of the column resulted in a shortening of the clear height of the column, thus creating a short column. Figure 1.2 shows the brittle shear failure of a bridge column due to the 2010 Chile earthquake (Mitchell et al., 2011). The 1000 mm x 2000 mm column failed in the short direction of the column due to seismic forces in the longitudinal direction of the bridge. The bridge crossed a river resulting in the end columns being shorter than the other bridge columns due to the presence of the river embankments and resulted in larger shear forces in these poorly reinforced shear-critical columns. The transverse reinforcement consisted of 8 mm diameter column ties, with



Figure 1.1: Damaged Column during 1995 Kobe Earthquake (Yoshimura and Nakamura, 2003)



Figure 1.2: Shear failure of bridge column in the 2010 Chile Earthquake (Mitchell et al., 2011)

90-degree bend anchorages spaced at 350 mm resulting in inadequate shear strength. The longitudinal reinforcement consisted of 25 mm diameter bars.

Sectional shear design provisions of the American Concrete Institute (ACI) (ACI Committee-318, 2019), Canadian Standards Association (CSA) A23.3 Standard (CSA, 2019), American Association of State and Highway Transportation Officials (AASHTO) LRFD Bridge Design Specifications (AASHTO, 2014) and the Canadian Highway Bridge Design Code (CHBDC) (CSA, 2019) are applicable to regions without discontinuities (B-regions) and have resulted from extensive research conducted primarily on reinforced concrete beams. Short columns, because of their low shear span-to-depth ratio, constitute a discontinuity region (D-region) along their entire height. For beams without transverse reinforcement, strut action plays an important role when the shear span-to-depth ratio is less than about 2.5 (Collins and Mitchell, 1991). For members with transverse reinforcement, the FIP Recommendations (FIP Commission 3, 1996) accounted for a combined resisting mechanism with a direct strut and stirrups for shear span-to-internal lever arm ratios less than 2.0 (i.e., a/d less than about 2.2). The design provisions of codes investigated in this thesis, offer conservative procedures for the design of axially loaded columns with low shear span-to-depth ratios.

The four rectangular reinforced concrete columns in this experimental program were designed to have a shear span-to-depth ratio, a/d , of 1.91. A column with a shear span-to-depth ratio of about 2.5 or less is considered to be a short column. The shear strength of reinforced concrete columns depends on many parameters such as the width and depth of the cross section, the height of the column, the concrete cover, the amount of longitudinal reinforcement, the level of axial load and the amount of transverse reinforcement. Although many parameters affect the shear strength, the amount of reinforcement (transverse and longitudinal) and the level of axial load are typically most critical. The specimens had a longitudinal reinforcement ratio of 4% that satisfies the CHBDC (CSA, 2019) requirements for ductile columns. The four reinforced concrete columns were detailed to have different transverse hoop spacings. The columns had transverse reinforcement amounts, $\rho_v f_y$, that ranged between 0.943 and 2.514 MPa. The

column specimens were subjected to a constant axial compressive load of 500 kN and were tested monotonically in shear under a reversed bending.

1.2 Previous Research

Although many series of tests have been conducted on columns subjected to reversed cyclic loading (e.g., Priestley et al. (1994)), few experimental programs have been conducted on short columns subjected to monotonic shear loading. There is a need to carry out tests on short shear-critical columns under monotonic loading to understand the complex behaviour that involves the development of a superimposed strut (D-region) on a compression field (B-region) resisting shear.

A study by Priestley et al. (1994) presented a predictive equation for the shear strength of circular and rectangular columns subjected to reversed cyclic lateral shear force. This equation separately considers the contributions of concrete mechanisms, axial load mechanisms and truss mechanisms. The predictive equation was compared with an extensive database of column tests. It provided a very good simulation of the influence of flexural ductility, axial load, and aspect ratio. The approach proposed in the study improved prediction of shear strength when compared to alternative existing design equations at the time (Priestley et al., 1994).

Pan and Li (2013) presented an improved analytical model for the prediction of the shear strength of reinforced concrete columns with a small shear span-to-depth ratio and high axial-load ratio. The shear strength of a short RC column is developed partly by a truss resisting mechanism and partly by arch or strut action. Considering the condition of deformation compatibility between the truss model and the arch model, a predictive expression for the shear strength of shear-critical reinforced concrete columns was developed. From the comparison of measured and predicted shear strengths of 90 shear-critical RC columns, the shear strength predicted by the proposed model was found to correlate well with experimental results (Pan and Li, 2013).

1.3 Research Objectives

The main objective of this research project was to conduct tests on short rectangular shear-critical columns subjected to axial compression and monotonically applied shear. Four shear-critical reinforced concrete columns containing different amounts of transverse reinforcement were constructed and tested. Shear strength predictions were made using the approaches in current code provisions, sectional analysis software and non-linear finite element analysis. In addition, predictions were made by superimposing strut action from the applied axial compression on to the analytical models used for B-regions. A secondary objective was to compare the shear behaviour of short columns using sectional models versus models considering the compressive strut action. In summary the objectives of this research program were:

1. Examine the behaviour of short columns with, $a/d < 2.5$
2. Study the effect of axial load on column shear strength.
3. Study the influence of the amount of transverse reinforcement on the shear strength and the overall behaviour.
4. Compare predictions made using a sectional design approach, truss-and-strut or arch models, and non-linear finite element analysis.
5. Develop a practical approach for predicting the shear strength of shear-critical columns within the context of Canadian design code procedures.

1.4 Outline of the Thesis

This thesis is comprised of six chapters starting with the introduction and objectives in this chapter. Brief descriptions of the shear provisions of the design codes and the analytical programs used to predict the shear strength of columns are given in Chapter 2. These predictions are later used for comparison with experimental results. Detailed descriptions of the geometry and material properties of each of the four specimens is given in Chapter 3. The experimental program including descriptions of the test apparatus, construction details and

instrumentation of the four rectangular columns is presented in this chapter. The experimental observations made during the loading of each specimen are presented in Chapter 4. Load-deformation responses, the development of reinforcing steel strains, crack development and crack widths at different load stages are provided in this chapter. The experimental and analytical results obtained are then compared and discussed in Chapter 5. The experimentally determined shear strengths of the specimens are compared with the predictions using several code provisions, analytical programs based on the Modified Compression Field Theory (MCFT) and empirical prediction models from the literature. Chapter 6 presents the conclusions of this thesis.

2 Literature Review and Previous Research

Analytical models based on the Modified Compression Field Theory (MCFT) are discussed in this chapter. The code provisions of the 2019 Canadian Highway Bridge Design Code CHBDC (CSA, 2019) and the 2019 American Concrete Institute (ACI) (ACI Committee 318, 2019) are also discussed. Analytical models from the literature and a new Truss-Arch model are also presented.

2.1 Modified Compression Field Theory (MCFT)

2.1.1 Background

The traditional ACI methodology for shear design considers a concrete contribution, V_c , and a contribution from the transverse reinforcement, V_s . To determine the shear carried by the steel component, V_s , the ACI Code assumed a 45° truss model (ACI committee 318, 1989). Kupfer (1964) proposed a variable-angle truss model assuming both the reinforcement and concrete were linearly elastic. Before the development of the 1984 Canadian Standards Association (CSA) A23.3 standard (CSA, 1984), shear design in North America was based upon provisions set by the ACI Code. The 1984 CSA A23.3 Standard proposed a sectional analysis method that differed from the traditional ACI approach (Collins and Mitchell, 1986). This “General Method” was based on the Compression Field Theory developed initially by Mitchell and Collins (1974) for pure torsion, which analyzed the behaviour of concrete once cracked where it no longer behaves elastically. This theory is based on the assumption that the principal tensile stress, f_1 , in the concrete after cracking was negligible. The angle of diagonal compressive stresses, θ , was considered as variable compared to the fixed value of 45° used by the ACI code. The angle of principal compression of the concrete was allowed to vary between 15° and 75° . An upper bound on, θ , was given when the principal compressive stress in the concrete, f_2 , reaches its crushing strength, $f_{2,max}$, (Collins and Mitchell, 1986).

2.1.2 MCFT

In the 1980s, after testing different reinforced concrete members elements subjected to pure shear, pure axial load, and a combination of shear and axial load, the Modified Compression Field Theory (MCFT) (Vecchio and Collins, 1986) was developed. The main finding of this theory was that significant tensile stresses exist in the concrete between the cracks, even at high values of average tensile strains, which were previously assumed to be negligible. Figure 2.1 summarizes the equilibrium, compatibility and stress-strain relationships used by the MCFT (Vecchio and Collins, 1986). The MCFT was able to determine the relationship between strains and stresses by making the key assumption that the concrete and reinforcement were perfectly bonded, thus having equal strains. In the relationships, θ , is the angle between the longitudinal axis of the member, and the direction of the principal compressive strain.

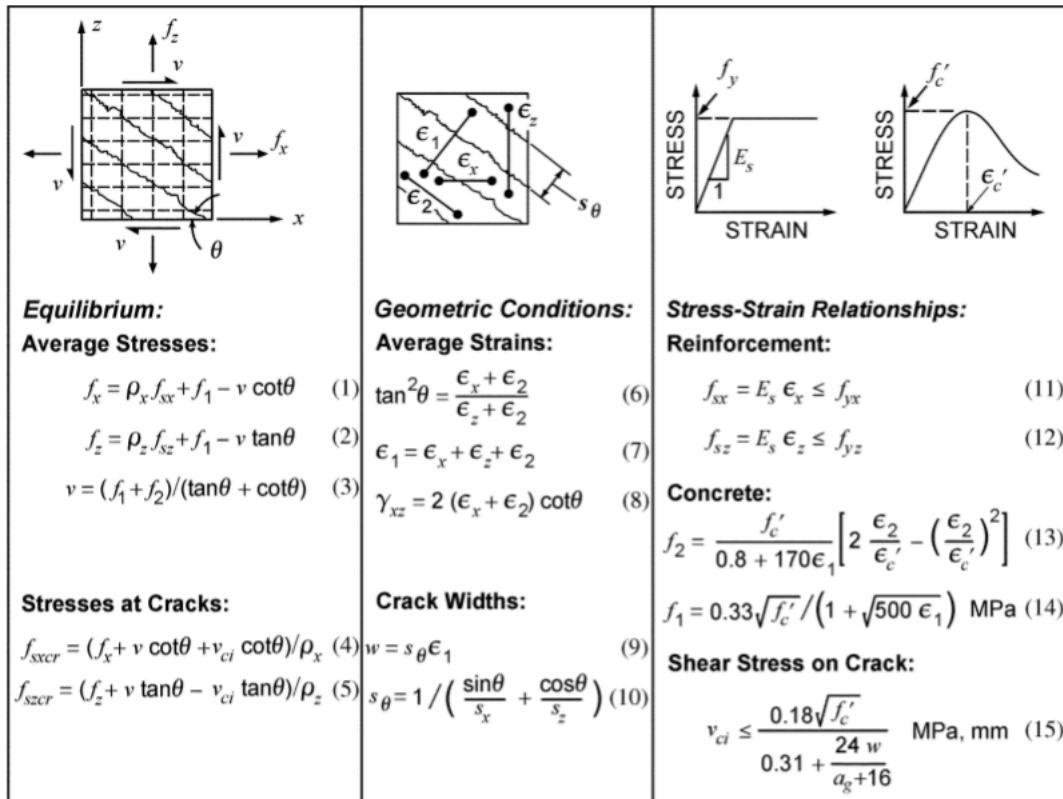


Figure 2.1: Equations of modified compression field theory (Bentz and Collins, 2006)

These average strains were measured over base lengths that were greater than the crack spacing. For specified applied loads, the angle, θ , the average stresses and the average strains can be determined by solving the given equilibrium equations in terms of average stresses, the given compatibility equations in terms of average strains, and the given average-stress versus average-strain relationships.

2.1.2.1 MCFT and Design Provisions

The MCFT was first developed into a practical shear design method by Collins and Mitchell (1991) which was subsequently implemented in the General Method of the CSA A23.3 1994 Standard and has become fundamental to shear design. The MCFT was able to accurately predict the shear behaviour of concrete members subjected to shear and axial forces. It has been implemented in several codes including the 1994 AASHTO LRFD Bridge Design Specifications (AASHTO, 1994) and the Ontario Highway Bridge Design Code OHBDC (OHBDC, 1991). To simplify the process of predicting the shear strength of a section using the MCFT, the shear stress is assumed to remain constant over the depth of the cross section, and the shear strength of the section can be determined by considering the axial strain at mid-depth of the web. This was the basis of the sectional design model for shear implemented by the CSA A23.3 Standard, the CHBDC Code and the AASHTO LRFD Specifications.

In these early versions of the MCFT the prediction of the parameter, β , and the angle, θ , was required to be determined using a cumbersome tabular approach. The parameter, β , reflects the ability of the diagonally cracked concrete to transmit tensile strains and shear stresses and, θ , is the angle of principal compressive stresses. The modified compression field theory was further simplified when direct equations were developed by Bentz and Collins (2006) for, β , and θ , to replace the iterative procedure that was implemented by earlier versions of the CSA Standard, the AASHTO LRFD Specifications and the CHBDC code.

For the 2004 CSA A23.3 Standard, Bentz and Collins (2006) derived straightforward equations for determining, θ and β , that would replace the aforementioned tabular approach. Looking first at, β , an equation independent of, θ , was developed.

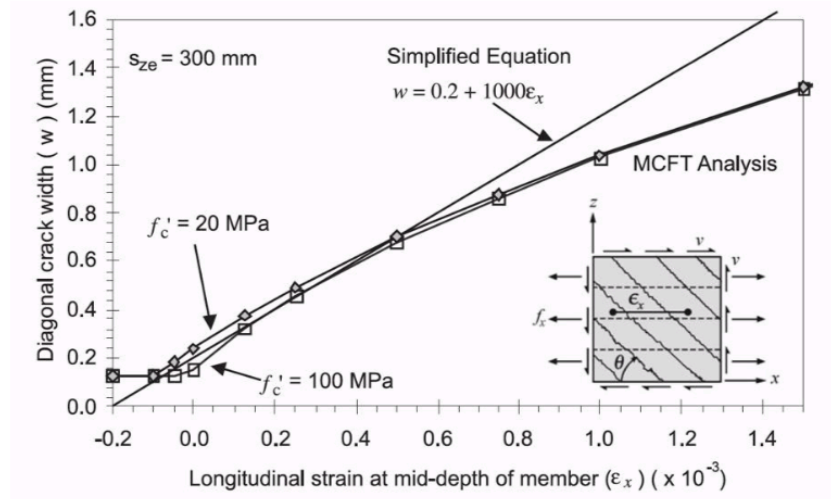


Figure 2.2: Simplified diagonal crack widths compared to MCFT (Bentz and Collins, 2006)

The simplified equation shown in Fig. 2.2, relating the crack width, w , to the longitudinal strain at mid-depth of the section, ϵ_x , only works for longitudinal strains larger than -0.2×10^{-3} , as values lower than this result in negative crack widths. Additionally, it is important to note that at high longitudinal strains the crack width equation becomes very conservative when compared to the predictions using the MCFT.

Bentz and Collins (2006) based the, θ , equation on a member with a significant amount of transverse reinforcement, where the ratio of shear stress to the concrete compressive stress, v/f'_c , equalled 0.25. Curves relating, θ , to, ϵ_x , for concrete with different compressive strengths were determined as shown in Fig. 2.3. One set of curves signified the lower bound for, θ , corresponding to the situation that the concrete compressive stresses reach the crushing limit. The upper bound corresponds to the situation where shear failure occurs without stirrup yielding.

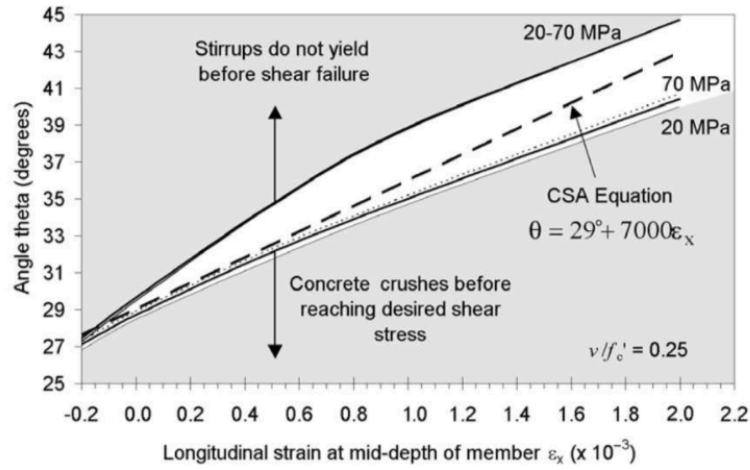


Figure 2.3: The CSA A23.3 2004 theta equation compared to upper and lower bounds (Bentz and Collins, 2006)

A suitable equation for, θ , was then determined to fit between the two limits:

$$\theta = 29 + 7000\epsilon_x \quad (2.2)$$

The result was that θ and β , could be more readily determined. Though, β , is based on a member with no transverse reinforcement and, θ , is based on a member with a large amount of shear reinforcement, for an amount of transverse reinforcement between these two limits Bentz and Collins (2006) showed that the use of these β and θ , values give appropriate conservative values.

2.2 Sectional Design Models

This section presents three sectional design models. The first two approaches are based on the MCFT to predict the shear response of reinforced concrete members namely: the CHBDC (CSA, 2019) simplified and general method and the computer program Response 2000. In addition to the code equations of the (ACI) (ACI Committee 318, 2019).

2.2.1 Canadian Highway Bridge Design Code (CSA, 2019)

The shear resistance of a member, V , given by the sectional design model of the CHBDC (CSA, 2019) is:

$$V = V_c + V_s + V_p \quad (2.3)$$

Where V_c , V_s , and V_p are the shear contribution of the concrete, transverse reinforcement, and vertical component of prestressing, respectively. This is shown in a free body diagram in Fig.

2.4.

$$V_c = \beta \sqrt{f'_c} b_v d_v \quad (2.4)$$

$$V_s = \frac{f_y A_v d_v \cot \theta}{s} \quad (2.5)$$

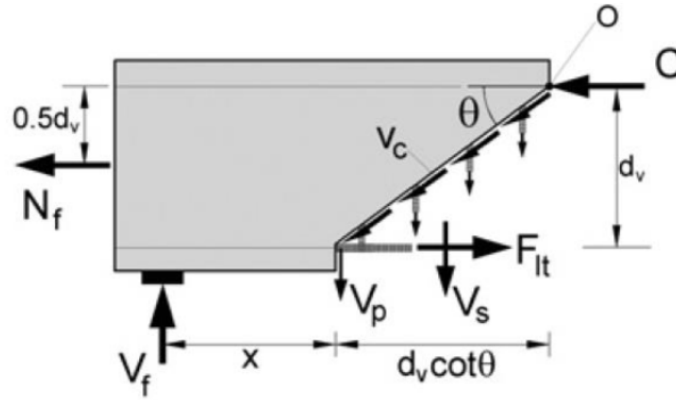


Figure 2.4: Free body diagram of shear resistance components (Bentz and Collins, 2006)

For typical situations, sections located less than, d_v , from the face of the support may be designed for the same shear as that computed at a distance of, d_v . The effective shear depth is taken as the maximum of 72% of the height, h , of the cross section or 90% of the effective depth, d . The effective depth is the depth from the top compressive surface to the centroid of the tensile reinforcement.

2.2.1.1 Determination of β and θ for Non-Prestressed Components (Simplified Method)

For non-prestressed components not subjected to axial tension, and provided that the specified yield strength of the longitudinal reinforcement does not exceed 400 MPa and the design concrete strength does not exceed 60 MPa, the value of the angle of inclination, θ , shall be taken as 42° and the value of the parameter, β , shall be 0.18 for members with at least the minimum amount of transverse reinforcement required.

2.2.1.2 Determination of β and θ (General Method)

The use of the General Method requires that the values of, β and θ , be determined by first determining the longitudinal strain at mid-depth of the section, ε_x , as follows:

$$\varepsilon_x = \frac{\frac{M_f}{d_v} + V_f - V_p + 0.5N_f - A_p f_{p0}}{2(E_s A_s + A_p E_p)} \quad (2.6)$$

Where, M_f , is the factored moment at the shear section corresponding to V_f , N_f , is the factored applied axial load. A_s , is the area of reinforcing bars on the flexural tension side of the member, E_s , is the elastic modulus of reinforcing steel. A_p , is the area of prestressing steel on the flexural tension side of the member, E_p , is the elastic modulus of prestressing and f_{p0} , is the stress in prestressing when the concrete strain is zero.

The parameter, β , takes into account the shear resistance of the cracked concrete. This is calculated as:

$$\beta = \frac{0.4}{1 + 1500\varepsilon_x} \left(\frac{1300}{1000 + s_{ze}} \right) \quad (2.7)$$

Where (s_{ze}) is taken as 300 mm for sections containing at least the minimum transverse reinforcement.

The angle of principal compression, θ , is calculated as:

$$\theta = 29 + 7000\varepsilon_x \quad (2.8)$$

2.2.2 Response 2000

Response 2000 was developed at the University of Toronto by Bentz (2000). This two-dimensional sectional analysis program for reinforced concrete members is used to determine the strength and ductility of a member subjected to shear, moment, and axial load. All three loads are considered simultaneously to find the full load-deformation response. This program treats each cross-section as a stack of biaxially stressed elements. The assumptions implicit in the program are that plane sections remain plane, and that there is no transverse clamping stress across the depth of the beam. For sections of a beam or column at a reasonable distance away from a support or point load, these are excellent assumptions (Bentz, 2001).

2.2.3 ACI Committee 318 (2019) Code Equations

The 2019 ACI (ACI Committee 318, 2019) considers a portion of the design shear force to be carried by the concrete, V_c , with the remainder carried by transverse steel, V_s , as done by earlier codes and models. To determine the shear carried by the steel component the ACI assumes a 45° truss model as shown in Fig. 2.5.

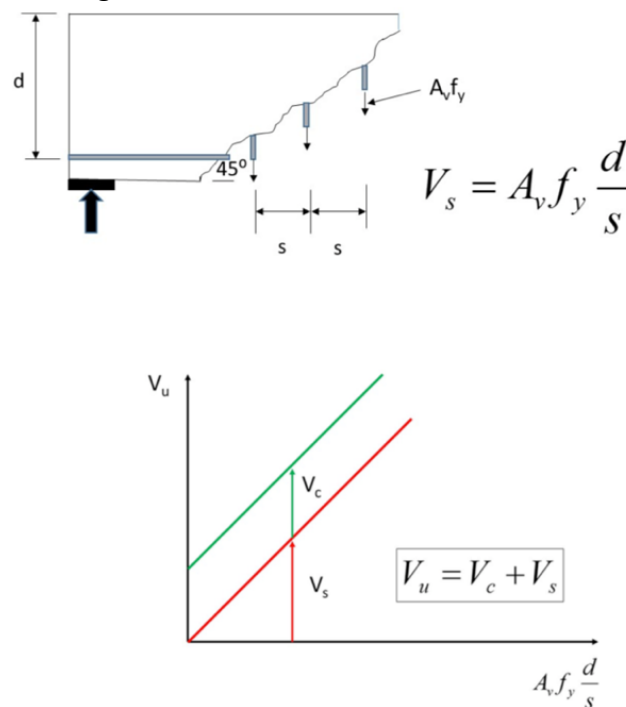


Figure 2.5: The ACI 45° truss model

The following ACI Code equation for calculating the nominal shear strength, V_n , for non-prestressed members subjected to combined shear and moment (ACI Committee 318, 2019) is given as:

$$V_n = V_c + V_s \quad (2.9)$$

For member subjected to axial compression, with at least the minimum amount of transverse reinforcement. V_c , can be calculated as follows:

$$V_c = \left[2\lambda\sqrt{f'_c} + \frac{N_u}{6A_g} \right] b_w d \quad (2.10)$$

Alternatively, the following expression may be used:

$$V_c = \left[8\lambda(\rho_w)^{\frac{1}{3}}\sqrt{f'_c} + \frac{N_u}{6A_g} \right] b_w d \quad (2.11)$$

Where, N_u , is the axial load applied to the section, A_g , is gross concrete cross-sectional area, f'_c , is concrete compressive strength, b_w , is the width of the section, and d , is the effective depth of the section. The longitudinal reinforcement ratio, ρ_w , maybe taken as the sum of the areas of longitudinal bars located more than two thirds of the overall member depth away from the extreme compression fiber. The modification factor, λ , accounts for the weight of the concrete and is taken as 1.0 for normal-weight concrete. A_v , is the area of transverse reinforcement within the spacing, s , and f_{yt} , is the yield stress of the transverse steel. In either case, the shear contribution of the transverse reinforcement, V_s , is given by:

$$V_s = \frac{A_v f_{yt} d}{s} \quad (2.12)$$

2.3 Non-Linear Finite Element Analysis

2.3.1 VecTor2

VecTor2 (Vecchio, 2018) is a non-linear finite element program developed by Vecchio at the University of Toronto for analyzing the response of two-dimensional models of reinforced concrete structures (Wong et al., 2013). This program performs its post-cracking analysis based on two foundational theories: The Modified Compression Field Theory as described earlier, and the Disturbed Stress Field Model (DSFM). The DSFM was developed by Vecchio (2000) as a revised model to the earlier MCFT, and as such is similar to the MCFT in many respects. The primary difference is that the DSFM takes into consideration crack shear slip which can be especially significant in lightly reinforced members. By including crack shear slip the assumption that principal stresses and principal strains have the same direction is no longer correct, as the principal strains change in direction faster than the principal stresses. Thus, the model becomes a smeared delayed rotating-crack model (Vecchio, 2000).

2.3.1.1 FormWorks

FormWorks is a pre-processor developed by Wong (2002) specifically designed to be used in tandem with VecTor2. It allows a user to create a two-dimensional finite element model representing a reinforced concrete member, to be then analyzed using VecTor2. FormWorks allows the user to select specific non-linear models to model various concrete and reinforcement responses. The non-linear models selected are then used in the VecTor2 analysis. A detailed summary of the non-linear models available for use could be found in (Wong et al., 2013).

2.3.1.2 Augustus

Augustus is a post-processor developed by Bentz (2003) that was developed for use with VecTor2. It provides graphical information from the VecTor2 analysis on key aspects of the member modelled in FormWorks. Such data includes the load-deformation response, stresses

and strains in the concrete and reinforcement, cracking patterns, crack widths and the deformations of the member.

2.3.2 Crack Widths and Spacing

Crack widths in concrete are quantified by an average crack width parameter, w_m . Concrete doesn't behave uniformly, with cracks varying in spacing and width. Thus, an average width is calculated. The expression for average crack width in VecTor2 is based on Walraven's (1981) crack width equation:

$$w_m = \varepsilon_{c1} s_m \quad (2.13)$$

Where, s_m , is the average crack spacing and ε_{c1} , is the average tensile strain. The average tensile strain is determined based on the MCFT. The average crack spacing is determined based on the CEB-FIP Model Code (CEB, 1978) as:

$$s_m = s \left(c + \frac{s}{10} \right) + k_1 k_2 \frac{d_b}{\rho_{ef}} \quad (2.14)$$

Where, c , is the clear concrete cover, d_b , is the diameter of reinforcing bars

s , is the maximum spacing of longitudinal reinforcement but not larger than $15d_b$

k_1 , is a factor for bond properties of reinforcing bars, taken as 0.4 for deformed bars and 0.8 for plain bars

k_2 , is a factor accounting for strain gradient in concrete $0.25(\varepsilon_1 + \varepsilon_2)/2\varepsilon_1$

ε_1 and ε_2 , are the largest and smallest tensile strain in $A_{c,ef}$, respectively

$A_{c,ef}$, is the area of the effective embedment zone, which is taken as a rectangular region with bounds $7.5d_b$ from the center of the reinforcing bars

A_s , is the effective steel area and ρ_{ef} , is the effective reinforcement ratio, equal to $A_s/A_{c,ef}$

2.4 Previous Research

Predictions using sectional models such as the variable angle truss model or the MCFT do not account for the strut action that occurs in short columns and are therefore conservative. In this section models from the literature that consider this strut or arch action will be presented.

2.4.1 Watanabe and Ichinose (1991)

Watanabe and Ichinose (1991) developed a strut-and-tie approach that combines the truss analogy with an arch model. The shear design approach of a combined model of truss and arch action is based on constitutive laws for concrete and steel, and a simplified two-dimensional stress distribution. Later, an adjustment was made for high-strength concrete and axial load but is not considered here (Watanabe and Kabeyasawa, 1998).

The load carried by the truss mechanism depends on the amount of web reinforcement and the load carried by the arch and the compression members of the truss is limited by the strength of the concrete. The fundamental design equation for the combined approach is expressed as:

$$V = V_t + V_a \quad (2.15)$$

Where, V_t , is the truss resistance and V_a , is the resistance provided by the arch or strut action.

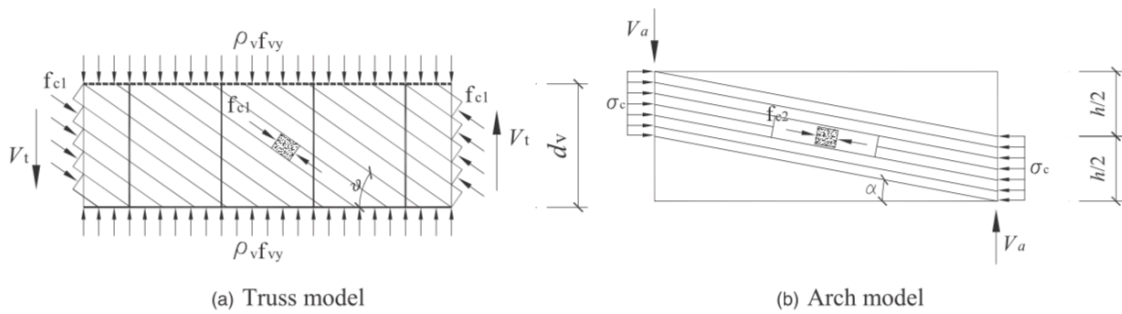


Figure 2.6: Truss-arch model by Ichinose (1992): (a) truss model; (b) arch

2.4.1.1 Arch Action

The contribution of the arch, is given as the bearing strength limit on the nodal zone by

$$V_a = \frac{1}{2}bh\sigma_c \tan \alpha \quad (2.16)$$

Where, b , is the width of the section, h , is the total depth, σ_c , is average stress in the compression strut and α , is the inclination of the arch.

For simplicity, it is assumed that the arch is linear, not bent, and has a depth equal to $h/2$.

According to this assumption the angle is given by the geometry of the member as

$$\tan \theta = \frac{\sqrt{L^2 + D^2} - L}{D} = \sqrt{\left(\frac{L}{D}\right)^2 + 1} - \frac{L}{D} \quad (2.17)$$

Where, L , is the member length.

2.4.1.2 Truss Action

The truss mechanism is modeled using the distance between the centroids of the outermost reinforcement for determining the height of the truss. It is assumed that the inclined truss force is uniformly distributed by the transverse reinforcement. The shear force attributed to truss action is given by

$$V_t = bd_v\rho_v f_{vy} \cot v \quad (2.18)$$

Where, d_v , is the distance between upper and lower reinforcement, ρ_v , is the transverse reinforcement ratio, f_{vy} , is yield strength of the transverse reinforcement and v , is the inclination of compressive stress in the concrete measured from the member axis.

The total shear is calculated as the superposition of arch and truss contributions, with the truss angle, ν , and the arch stress, σ_c , being the variables. These variables depend on the considered location, that is, whether the desired behaviour at the respective location is non-ductile or ductile.

2.4.2 Truss and Strut Model by Priestley et al. (1994)

Priestley et al. (1994) proposed a model for the shear strength of reinforced concrete members under cyclic lateral load as the summation of the concrete contribution, V_c , the contribution from the transverse reinforcement, V_s , and the contribution from the strut mechanism, V_p , associated with axial load. In this model the arch contribution relies on the axial compression acting on the column.

$$V_u = V_c + V_s + V_p \quad (2.19)$$

The concrete mechanism term is

$$V_c = k \sqrt{f'_c} A_e, A_e = 0.8 A_g \quad (2.20)$$

Where, k , within plastic end regions depends on member's displacement ductility. The degradation factor is only applied to the concrete component. Factor, k can be obtained from Fig. 2.7.

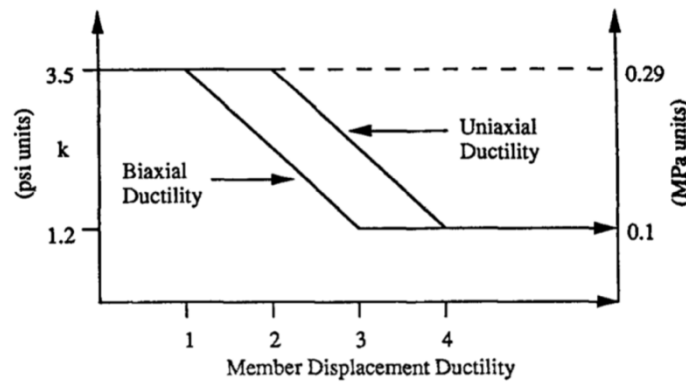


Figure 2.7: Degradation factor with displacement ductility (Priestley et al., 1994)

The truss mechanism component for a rectangular column is

$$V_s = \frac{A_v f_{yh} D'}{s} \cot 30^\circ \quad (2.21)$$

Where, D' , is the distance between centers of the peripheral hoop.

The contribution of transverse reinforcement to shear strength is based on a truss mechanism using a 30° angle between the compression diagonals and the members longitudinal axis.

The strut load component is given as:

$$V_p = P \tan \alpha = \frac{D - c}{2a} P \quad (2.22)$$

Where, D , is the overall depth of the section, c , the depth of compression zone, and a , is equal to column length, L , for a cantilever column or $2L$, for a column in reversed bending.

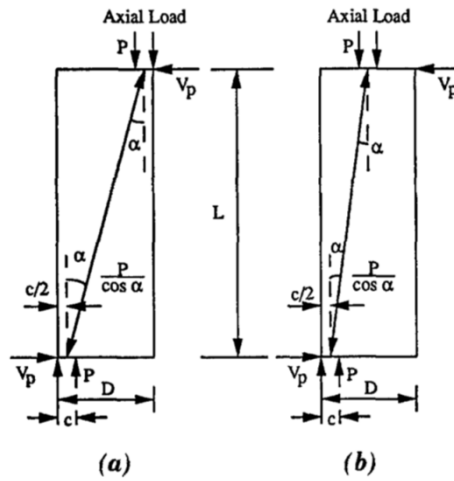


Figure 2.8: Contribution of axial force to column shear strength (Priestley et al., 1994)

It is noted that the column axial force enhances the shear strength by forming an inclined strut, as shown in Fig. 2.8. There are similarities to the arch action of Ichinose's model, except that in this approach the arch or strut action is dependent on the axial-load level, whereas Ichinose's

model is independent of axial load. The enhancement to shear strength is the horizontal component of the diagonal compression strut, since this component directly resists the applied shear force.

2.4.3 Truss-Arch Model by Pan and Li (2013)

The approach by Ichinose (1992) does not include the effects of axial load, and hence provides good predictions at low axial-load levels, but the lack of specific consideration of the axial load leads to increased conservatism as the axial-load level increases. Also, in the derivation of the shear design equation by Ichinose and Priestley, the deformation compatibility between the truss and the arch has not been accounted for. In Ichinose's model the height of the strut is assumed to be half the height of the column, which does not match experimental observations. Moreover, in Ichinose's truss model, the contribution of concrete to shear, such as the aggregate interlock on the crack surface, has not been considered.

A truss-arch model to predict the shear strength of shear-critical RC columns, developed by Pan and Li (2013) was based on the shear strength model of (Ichinose, 1992). This model can reasonably represent the contributions of shear span-to-depth ratio, a/d , and the axial-load ratio, $P/(f'_c A_g)$, to the shear strength of RC columns. As an improvement to Ichinose's shear model, deformation compatibility between the truss model and the arch model, as well as a more reasonable effective depth for the arch model, are considered. The validity of the proposed model has been verified by the test data of 90 shear-critical RC columns in reversed cyclic loading tests (Pan and Li, 2013).

For RC columns that have been subjected to the combined action of shear, flexure, and axial compressive forces, the arch action is significant for the following reasons:

- i. The shear strength of a RC column increases as the shear span-to-depth ratio decreases. i.e., as members become, deeper or shorter, more shear force will be transmitted directly to the support by a compressive strut.

- ii. The axial compressive force increases the neutral axis depth of the section.
- iii. The angle of inclined cracks can be decreased.
- iv. Crack width can be reduced and the ability of the crack interface to transmit shear force increases.

For RC columns with a small shear span-to-depth ratio or high axial-load ratio, Bernoulli's hypothesis of plane-strain distribution is no longer reasonable, and parts of the shear force are directly transmitted by arch or strut action due to the compressive strut. Therefore, a sectional model will provide conservative estimates of the shear strength, especially for RC columns with a small shear span-to-depth ratio and significant axial loads.

2.4.3.1 Truss-Arch Model for Shear Strength

The shear behaviour of RC columns can be described by means of the variable angle truss model with a compressive strut arch in terms of the diagonal cracks pattern shown in Fig. 2.9. However, the variable angle truss model with a compressive strut arch superimposed is statically indeterminate and is of limited applicability in practice.

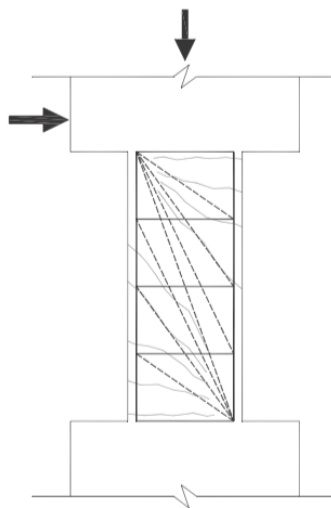


Figure 2.9: Variable angle truss model (Pan and Li, 2013)

The variable angle truss model could be approximated by a constant angle truss model given that, $a > d_v \cot(\theta)$, where a , is the shear span, d_v , is the effective shear depth and θ , is the angle of principal compression. Based on a truss model with a compressive strut arch an expression was developed by Pan and Li (2013) to predict the shear strength of RC columns,

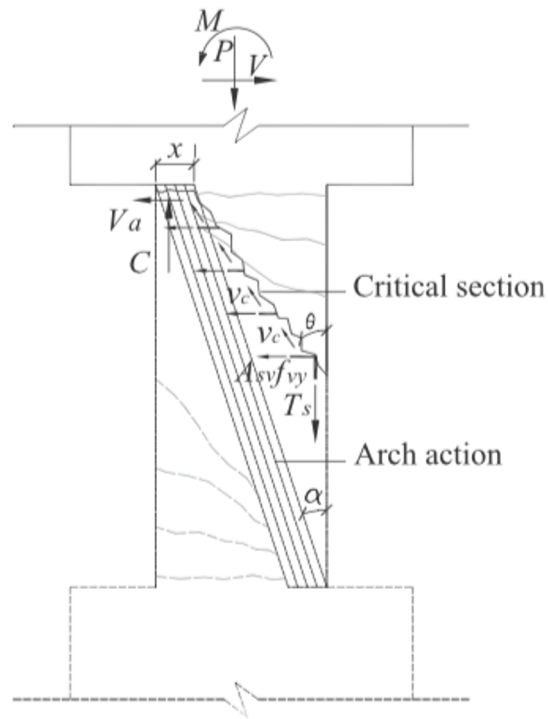


Figure 2.10: Critical section (Pan and Li, 2013)

considering the compatibility of deformation between the truss model and the arch model. The components of shear strength for a shear-critical RC column are illustrated in Fig. 2.10. The shear strength of the column consisting of three components is as follows:

$$V = V_{ct} + V_s + V_a \quad (2.23)$$

Where, V_{ct} , and V_s , are contributions of concrete and transverse reinforcements to the shear in the truss model, respectively and V_a , is the shear strength provided by the arch action.

2.4.3.2 Truss Component

The contribution of concrete and transverse reinforcement to shear in the truss model is based on the MCFT. The contribution of transverse reinforcement to shear can be expressed as

$$V_s = \frac{f_y A_v d_v \cot \theta}{s} \quad (2.24)$$

V_{ct} , is expressed as

$$V_{ct} = \beta \sqrt{f'_c} b_v d_v \quad (2.25)$$

A model proposed by Kim and Mander (1999) estimates the crack angle based on minimizing the external work caused by a unit shear force and is calibrated by experimental observations. The expression for, θ , is as follows (Kim and Mander, 1999)

$$\theta = \arctan \left(\frac{n\rho_v + \xi_2 \frac{\rho_v b d_v}{\rho_{sl} A_g}}{1 + n\rho_v} \right)^{\frac{1}{4}} \quad (2.26)$$

Where, ξ_1 , is the boundary condition factor for calculating, ε_x . ξ_1 , is taken as 2 for fixed-fixed ends or 1 for fixed-pinned ends. ξ_2 , is the column boundary condition factor. ξ_2 , is taken as 0.57 for fixed-fixed ends or 1.57 for fixed-pinned ends.

The concrete contribution to shear strength in the truss model is calculated as follow:

$$V_{ct} = \frac{-B + \sqrt{B^2 - 4AC}}{2A} \quad (2.27)$$

$$A = \frac{750}{E_s A_s} \left(1 + \frac{L}{\xi_1 d_v} \right) \quad (2.28)$$

$$B = \frac{750V_s}{E_s A_s} \left(1 + \frac{L}{\xi_1 d_v} \right) - \frac{375P}{E_s A_s} + 1 \quad (2.29)$$

$$C = \frac{-520\sqrt{f'_c} b d_v}{1000 + s_{ze}} \quad (2.30)$$

Where, s_{ze} , is taken as 300 mm for sections containing at least the minimum transverse reinforcement.

2.3.3.3 Arch Component

The arch mechanism is assumed to be related to a single compressive strut directed from the compression zone at the top toward that at the bottom as shown in Fig. 2.11. If the RC column is in double bending, the inclination of the strut is found from the line joining the centers of flexural compression at the top and at the bottom of the column.

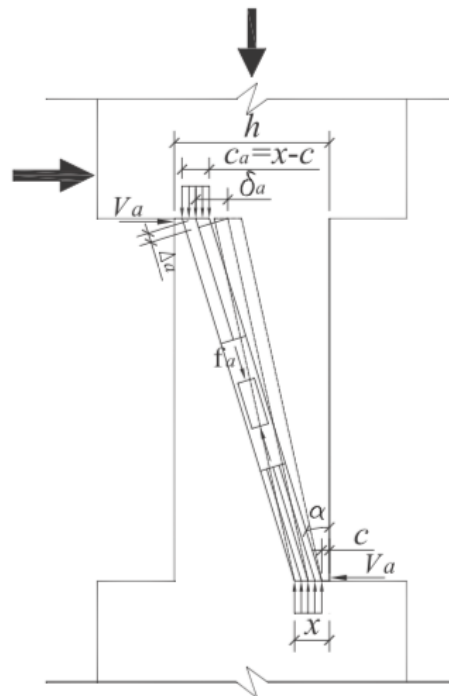


Figure 2.11: Arch model, columns with fixed-fixed ends

The arch contribution is derived from the condition of deformation compatibility between the truss model and the arch model. The shear deformation induced by the truss model must be equal to that induced by the arch model as follow

$$\frac{V_t}{K_t} = \frac{V_a}{K_a} \quad (2.31)$$

Where, K_t , is the shear stiffness of the truss model taken as

$$K_t = \frac{n\rho_v E_c b d_v (\cot \theta)^2}{1 + n\rho_v (\csc \theta)^4} \quad (2.32)$$

K_a , is the shear stiffness of the strut arch model taken as

$$K_a = E_c b c_a (\sin \alpha)^2 (\cos \alpha)^2 \quad (2.33)$$

Where, α , is the inclination of the strut. For a column in double bending, α , is taken as, $(h - x)/L$, or as, $(h - x)/2L$, for a column in single bending. c_a , is the effective depth of the strut in the arch model. For RC columns under cyclic loading, the concrete cover will partly spall off when the maximum shear force is reached; therefore, c_a , will decrease. Here, c_a , can be taken as, $x - c$.

The neutral axis depth, x , can be estimated as follows (Paulay and Priestley, 1992)

$$x = \left(0.25 + 0.85 \frac{P}{f'_c A_g} \right) h \quad (2.34)$$

The shear strength of RC column under monotonic loading is

$$V_m = V_{ct} + V_s + V_a = (V_{ct} + V_s) \left(1 + \frac{K_a}{K_t} \right) \quad (2.35)$$

3 Experimental Program

3.1 Introduction

The experimental program consisted of the construction and testing of four full-scale reinforced concrete column specimens. The reinforced concrete columns were detailed to have different transverse hoop spacings. Each column specimen was monolithically cast with walls at the ends of the column to provide fixed-end conditions in the testing frame.

3.2 Details of Specimens

3.2.1 Geometric Design

The geometry of the specimens can be seen in Fig. 3.1. The columns were tested in the horizontal position in the testing frame. Each end wall was 300 mm in width, 1200 long and 1200 mm high. Each column was 250 mm in width and measured 1200 mm in length by 400 mm in height (1200 mm x 400 mm x 250 mm).

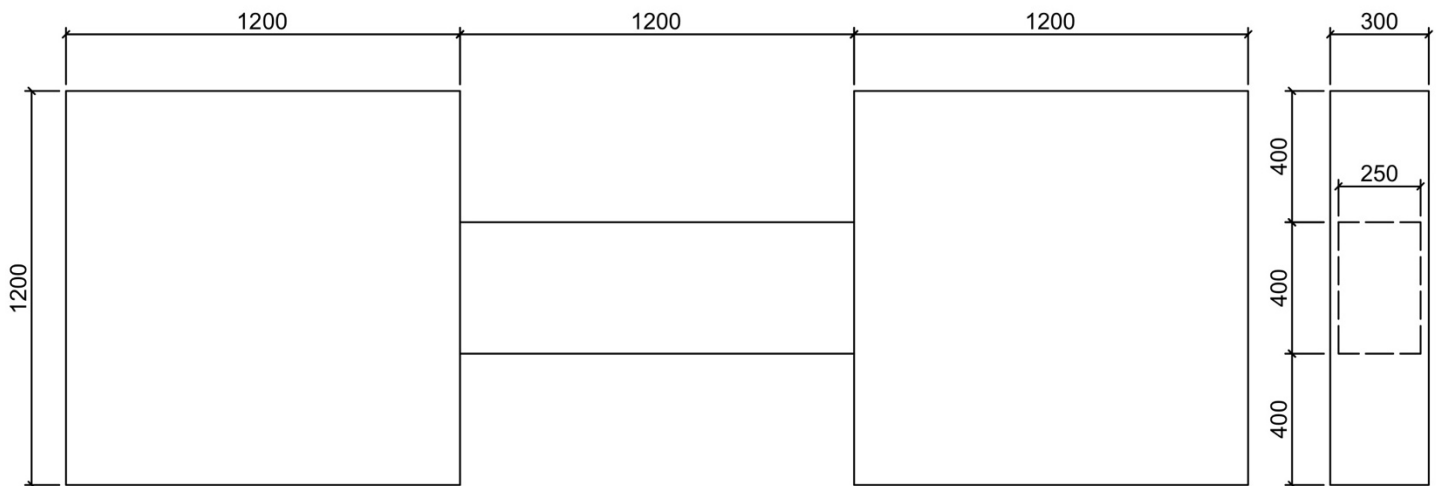


Figure 3.1: Geometry of column specimens

3.2.2 Reinforcing Steel Design

All of the columns were designed to fail in shear and contained three 25M longitudinal bars in the top and bottom layers and two 25M bars at mid-height of the cross section. This reinforcement results in a longitudinal reinforcement ratio of 4% that satisfies the CHBDC (CSA, 2019) requirements for ductile columns. Figure 3.2 shows the typical detailing and cross-section of a column specimen. The concrete clear cover was 25 mm.

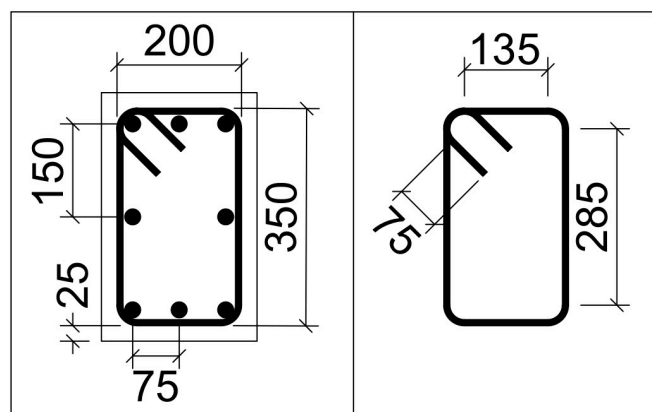
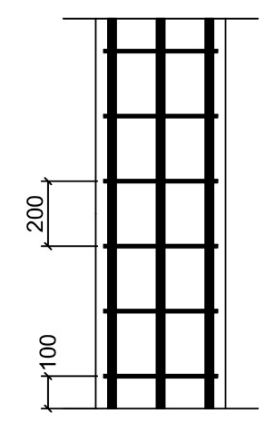
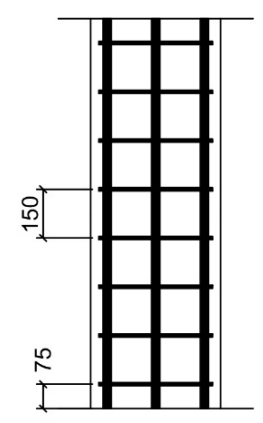
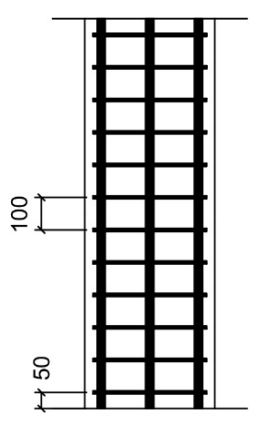
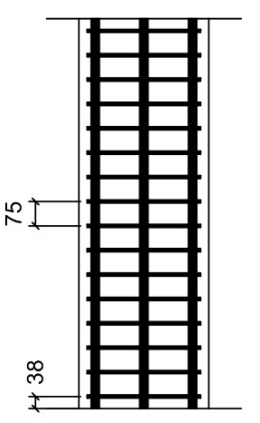
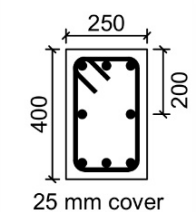


Figure 3.2: Detailing of typical column cross section

The transverse reinforcement consisted of US No. 3 hoops ($A_s = 0.11 \text{ in.}^2 = 71 \text{ mm}^2$ per bar) in order to provide a smaller bar size. The spacing of the hoops varied for each specimen. The hoop spacings, s , and shear reinforcement ratios are shown in Table 3.1. The hoops are anchored with 135° bends, having free end extensions of 75 mm. The free end extension satisfies the ACI 318-19 code but is somewhat less than the minimum free end extension of 100 mm required for seismic hooks in the CSA A23.3-19 Standard and the CSA S6-19 Standard. The first hoop was located at a distance equal to $s/2$ from the face of each wall. The amount of transverse reinforcement was chosen such that at least a minimum amount of shear reinforcement was provided.

Table 3.1: Summary of transverse reinforcement in column specimens

Specimen M1		Specimen M2		Specimen M3		Specimen M4	
							
Cross Section		Specimen M1		Specimen M2		Specimen M3	
		Hoop Spacing		Hoop Spacing		Hoop Spacing	
		8d _b		6d _b		4d _b	
		200 mm		150 mm		100 mm	
		ρ _v f _y (MPa)		1.257		1.886	
		0.943		1.257		1.886	

As per the CHBDC (CSA, 2019) the development length required, for a 25M bar (assuming Grade 400 steel and a concrete strength of 30 MPa) is:

$$\begin{aligned} l_d &= 0.45k_1k_2k_3k_4 \frac{f_y}{\sqrt{f'_c}} d_b > 300 \text{ mm} \\ &= 0.45(1.0)(1.0)(1.0)(1.0) \frac{400}{\sqrt{30}} (25) = 822 \text{ mm} \end{aligned} \quad (3.1)$$

Where,

K_1 = bar location factor = 1.0

K_2 = coating factor = 1.0 for uncoated reinforcement

K_3 = concrete density factor = 1.0 for normal-density concrete

K_4 = bars size factor = 0.8 for 20M bars and smaller

All eight 25M longitudinal bars provided were extended all the way in the end walls in each direction to provide adequate anchorage.

Details of the columns and the walls are shown below for each specimen.

3.2.3 Specimen M1

Column M1 contained eight 25M longitudinal bars with No. 3 hoops spaced at 200 mm. This spacing equals eight times the diameter of the 25M longitudinal reinforcing bars. The first hoop was placed at $s/2 = 100$ mm from the face of each wall. The reinforcement details for specimen M1 are shown in Fig. 3.3 and Fig. 3.4.

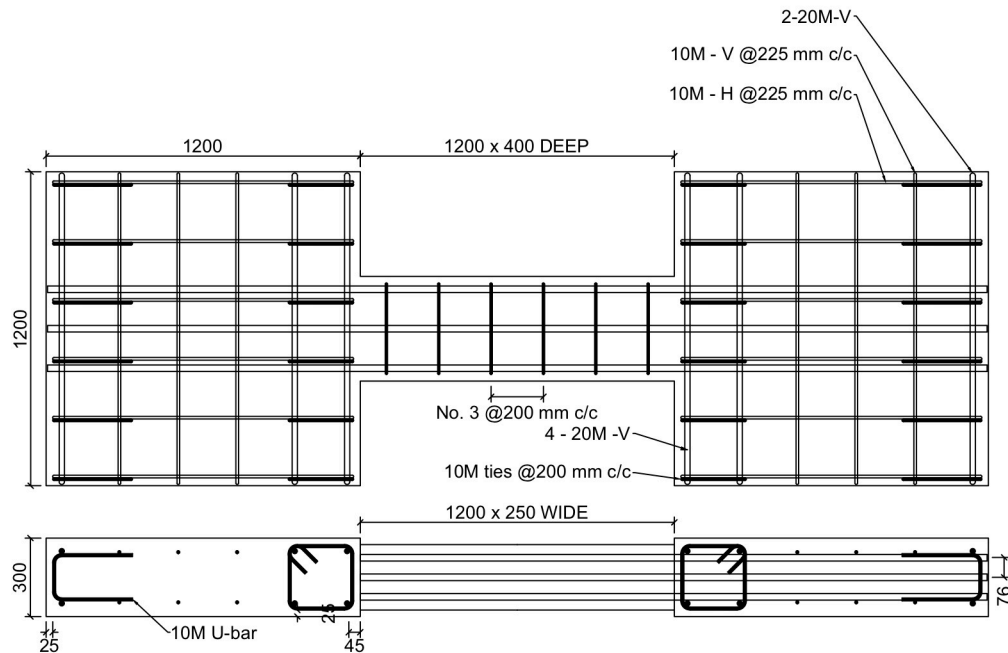


Figure 3.3: Detailing of specimen M1

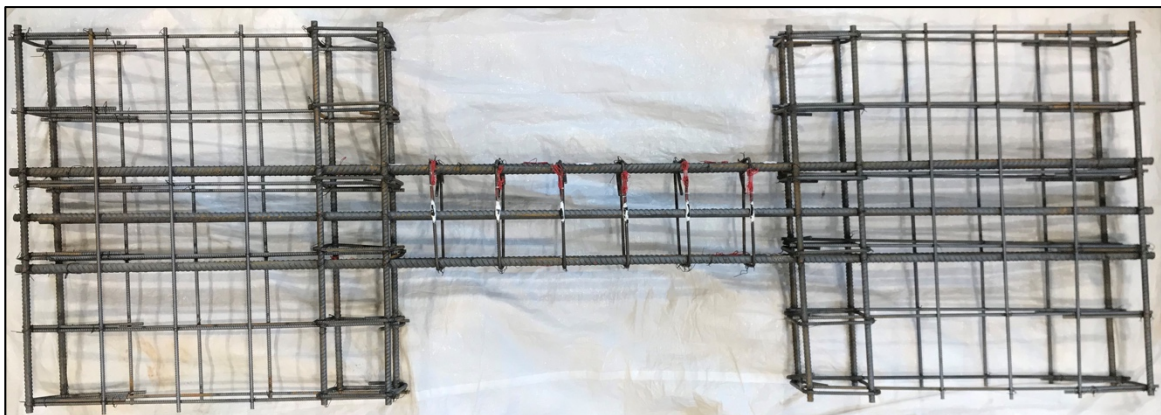


Figure 3.4: Reinforcing steel of specimen M1

3.2.4 Specimen M2

Column M2 contained eight 25M longitudinal bars with No. 3 hoops spaced at 150 mm. This spacing equals six times the diameter of the 25M longitudinal reinforcing bars. The first hoop was placed at $s/2 = 75$ mm from the face of each wall. The reinforcement details for specimen M2 are shown in Fig. 3.5. and Fig. 3.6.

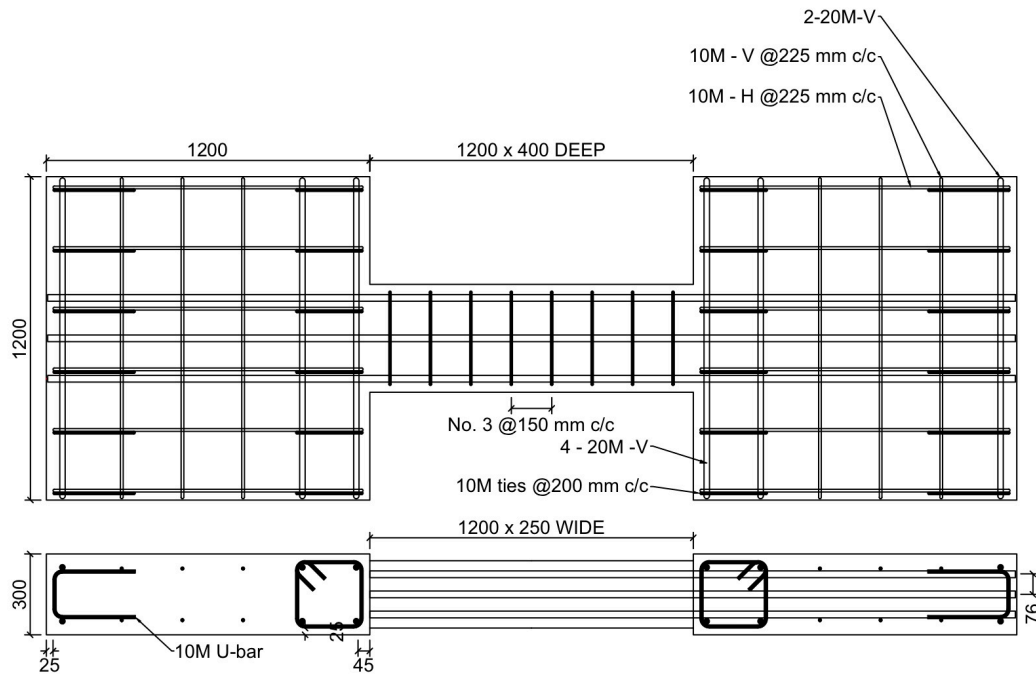


Figure 3.5: Detailing of specimen M2

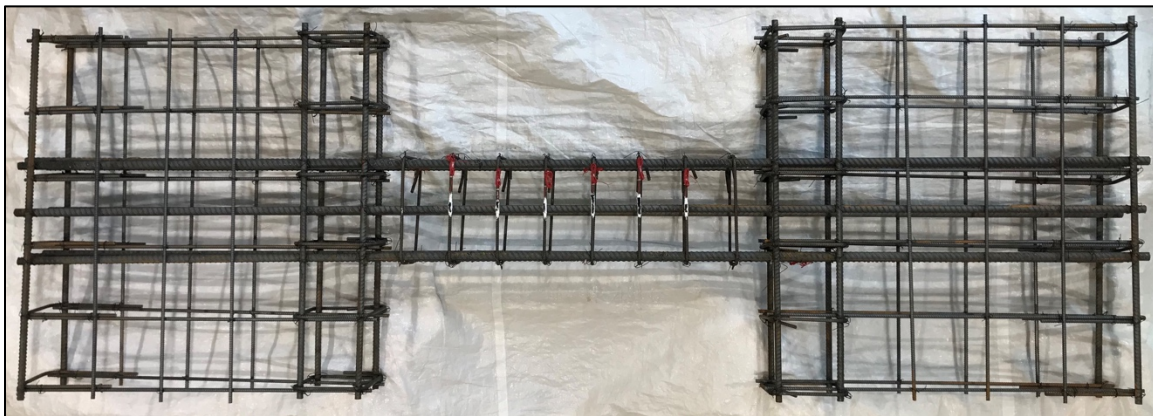


Figure 3.6: Reinforcing steel for specimen M2

3.2.5 Specimen M3

Column M3 contained eight 25M longitudinal bars with No. 3 hoops spaced at 100 mm. This spacing equals four times the diameter of the 25M longitudinal reinforcing bars. The first hoop was placed at $s/2 = 50$ mm from the face of each wall. The reinforcement details for specimen M3 are shown in Fig. 3.7. and Fig. 3.8.

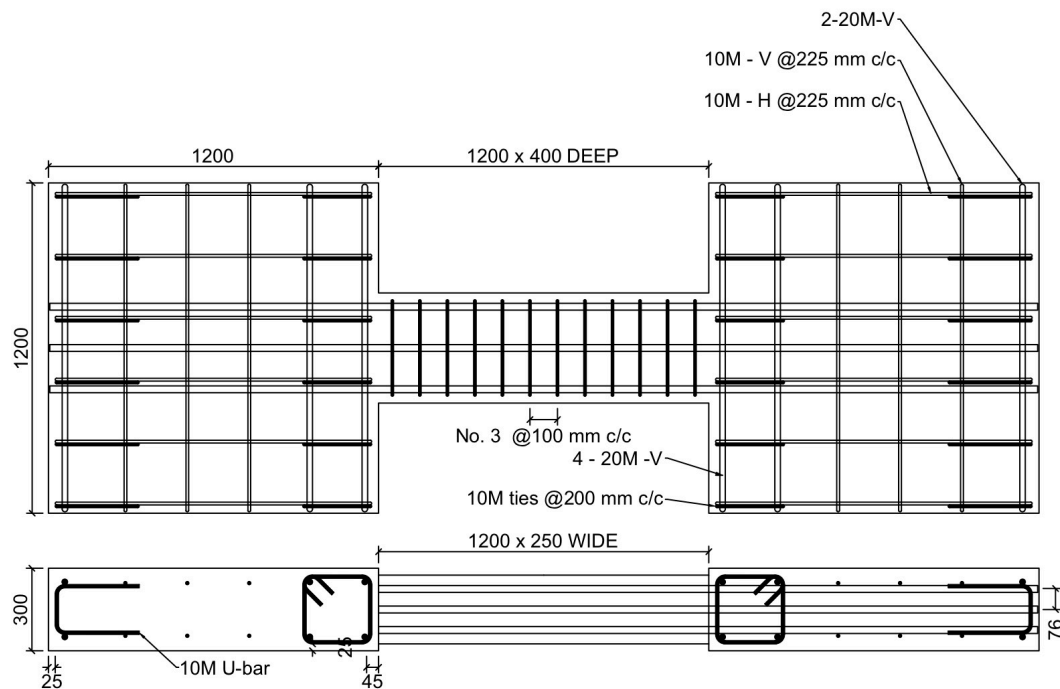


Figure 3.7: Detailing of specimen M3

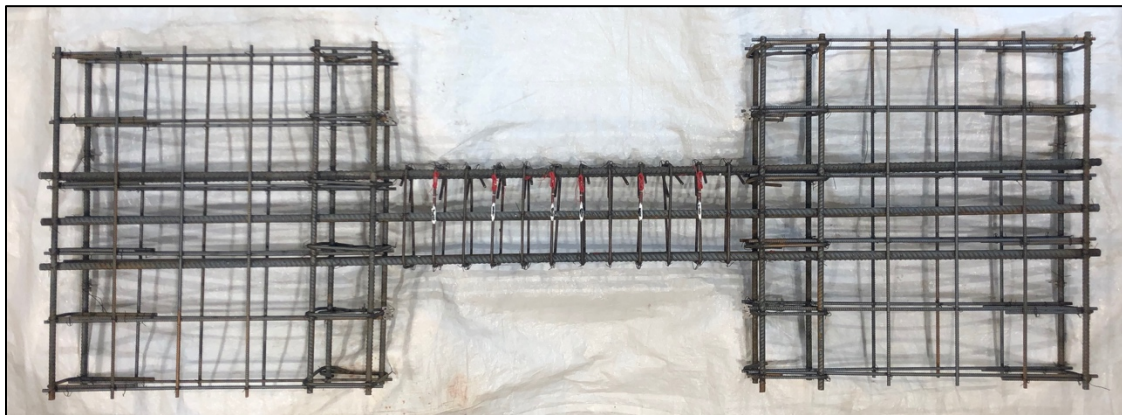


Figure 3.8: Reinforcing steel for specimen M3

3.2.6 Specimen M4

Column M4 contained eight 25M longitudinal bars with No. 3 hoops spaced at 75 mm. This spacing equals three times the diameter of the 25M longitudinal reinforcing bars. The first hoop was placed at $s/2 = 38$ mm from the face of each wall. The reinforcement details for specimen M4 are shown in Fig. 3.9 and Fig. 3.10.

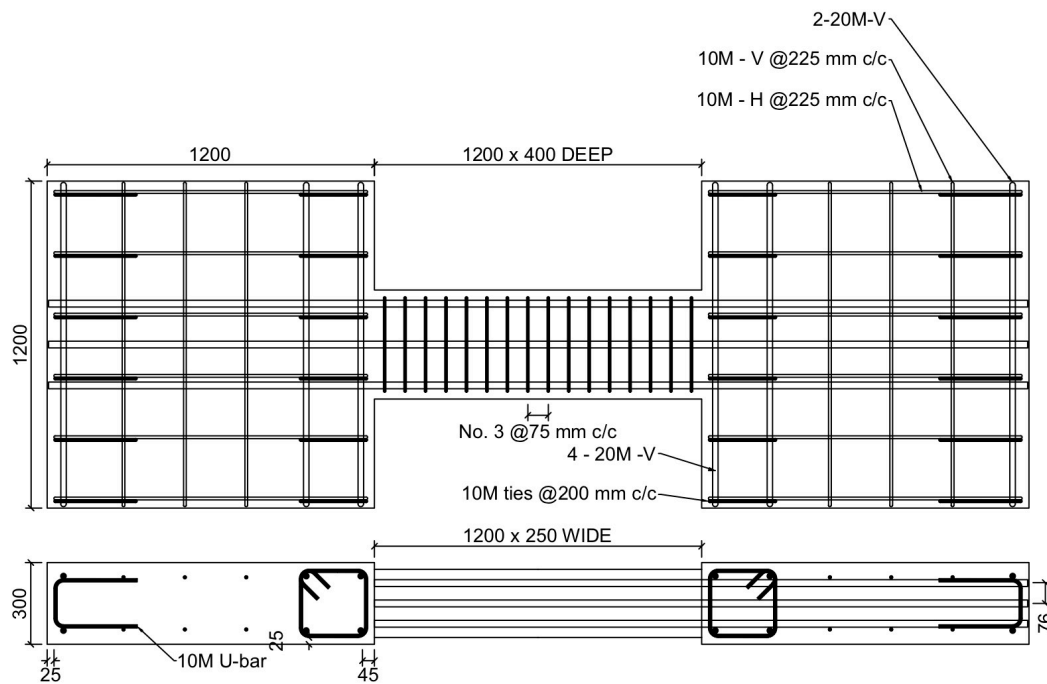


Figure 3.9: Detailing of specimen M4

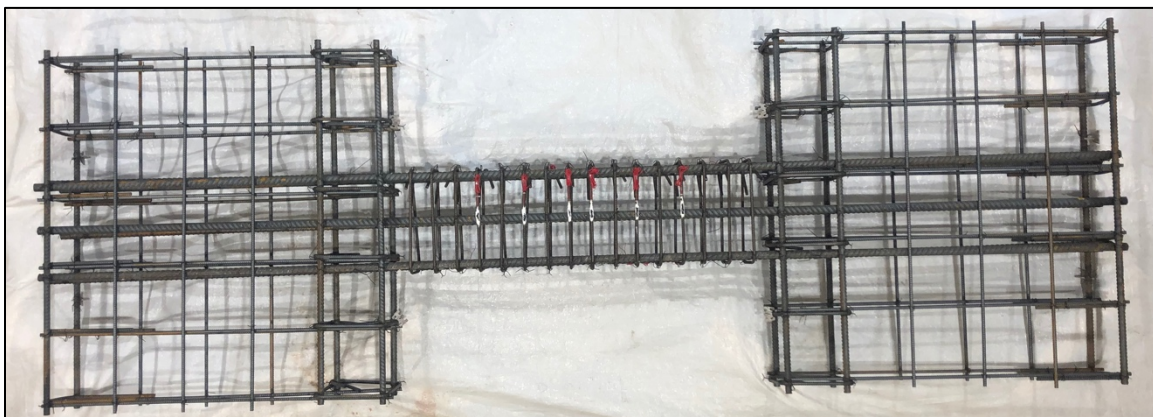


Figure 3.10: Reinforcing steel for specimen M4

3.3 Construction

All steel bars were cut and bent in the laboratory, except for the 25M longitudinal straight bars which were ordered to length. The reinforcing cages were assembled in a horizontal position for ease of construction. For each specimen the two assembled wall cages were then placed over the formwork and the longitudinal 25 M bars were placed in their respective positions joining the two wall cages. Finally, the No. 3 hoops were placed to provide the corresponding hoop spacing for each specimen. Casting the columns flat was advantageous in terms of facilitating formwork design. The wall reinforcing cages were positioned on 35 mm high plastic spacers that were placed on the formwork. The positioning of one of the walls reinforcing cages is shown in Fig. 3.11.



Figure 3.11: Placing of wall reinforcement cage above formwork for final assembly

The reinforcement cages for four specimens in the formwork in the final state before casting is shown in Fig. 3.12. Additional stiffeners were added to all sides of the formwork to protect against any formwork bulging during casting. The casting of specimens M1 and M2 and the associated cylinders for material testing are shown in Fig. 3.13 and Fig. 3.14, respectively.



Figure 3.12: Specimens M1 and M2 in formwork before casting



Figure 3.13: Casting of specimens



Figure 3.14: Casting of cylinders

3.4 Material properties

3.4.1 Concrete

The specimens were cast in place using two different ready-mix normal density concrete batches. Batch 1 was used for specimens M1 and M2, and Batch 2 for specimens M3 and M4. Table 3.2 summarizes the mix proportions, which were the same for the two batches. A slump test and air content test were performed for the fresh concrete before placement as per the CSA A23.2-5C and CSA A23.2-4C (CSA, 2014) standards, respectively. The ready-mix concrete properties are given in Table 3.3.

Table 3.2: Ready-mix concrete proportions

Component	Quantity (per m ³)
Cement type S	55 kg
Portland Cement type GUL	220 kg
Concrete sand	932 kg
5-14 mm stone	442 kg
10-20 mm stone	541 kg
Water	150 L
Air entraining agent	22 ml/100kg
Water – reducing admixture	133 ml/100kg
Air	5.5%

Table 3.3: Expected ready-mix concrete properties

Property	Value
Specified Concrete Strength (MPa)	25
Entrained Air (%)	5-8
Slump (mm)	80 ± 30

The specimens were cast in the formwork and the concrete carefully vibrated. Approximately two hours after casting the specimens were covered with wet burlap and plastic sheeting. The specimens were left to moist cure in the formwork for three days, after which the formwork was removed, and the specimens were allowed to cure at room temperature until testing. Concrete cylinders were cast from the batches at the time of casting the specimens. Like the

specimens, the cylinders were covered in wet burlap and plastic sheeting right after casting. After 24 hours in this condition the cylinders were then removed from their forms and were placed in a curing chamber until testing. Each cylinder measured 100 mm in diameter, with a length of 200 mm as per the requirements in the CSA A23.2-12C (CSA, 2014) Standard. They were used in determining the average compressive strength, f'_c , and the splitting tensile strength, f_{sp} , prior to testing of the specimen from the compression and split-cylinder tests detailed in CSA A23.2-9C and CSA A23.2-13C respectively (CSA, 2014). Similarly, concrete rectangular beams were cast and stored in the fog room, each measuring 100 mm in depth, 100 mm in width, and 350 mm in length as per the requirements in the CSA A23.2-8C (CSA, 2014). The beams were used in four-point bending tests to determine the modulus of rupture, f_r . All material properties were determined from the average of three test samples in accordance with CSA A23.2 (CSA, 2014). Table 3.4 summarizes the concrete material properties that were obtained for each specimen. Figure 3.15 shows typical concrete compressive stress-strain relationships representative of Batch 1 (specimen M1 and M2) and Batch 2 (specimen M3 and M4).

Table 3.4: Concrete material properties

Batch (Specimen)	Age at testing (days)	f'_c (MPa) (STDEV)	ϵ'_c (STDEV)	f_{sp} (MPa) (STDEV)	f_r (MPa) (STDEV)
1 (M1)	109	37.9 (0.7)	0.00177 (0.00004)	3.81 (0.31)	5.52 (0.23)
1 (M2)	123	37.1 (0.3)	0.00178 (0.00019)	4.19 (0.21)	5.52 (0.23)
2 (M3)	121	35.9 (1.4)	0.00172 (0.00003)	3.97 (0.26)	5.01 (0.27)
2 (M4)	135	35.9 (1.5)	0.00180 (0.00016)	3.97 (0.26)	5.01 (0.27)

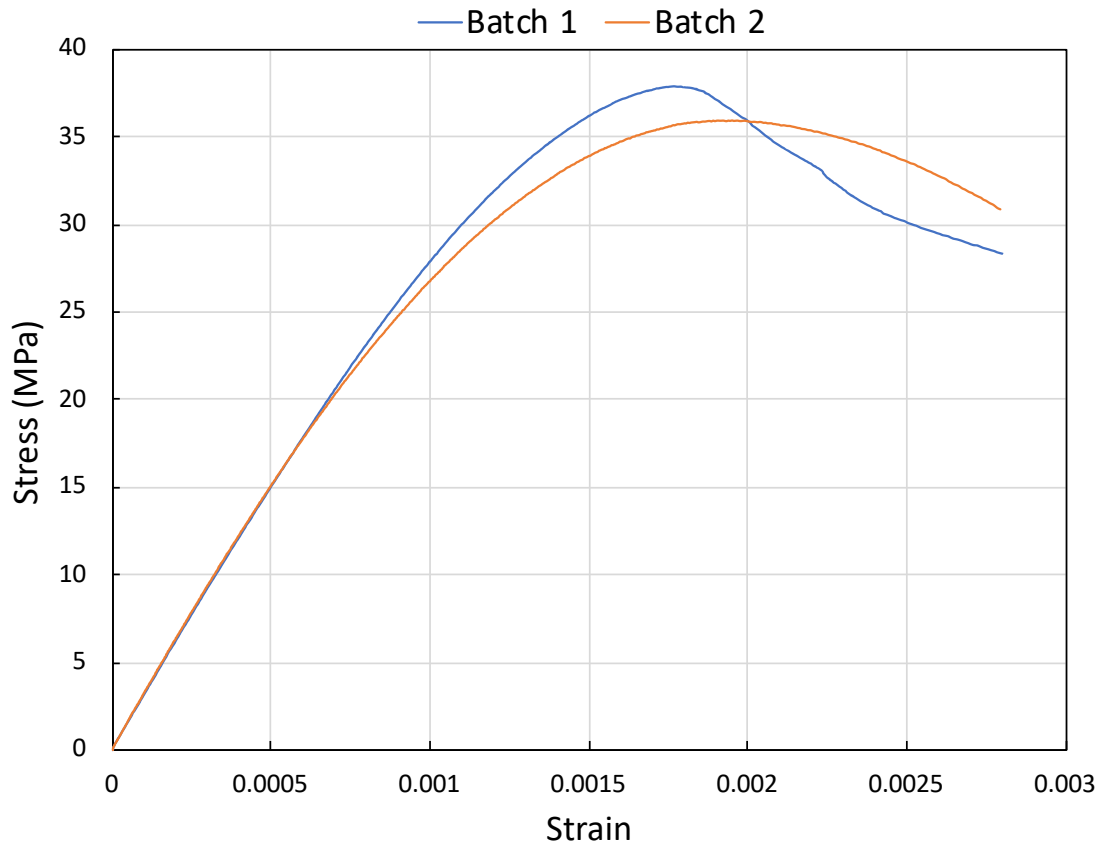


Figure 3.15: Typical concrete compressive stress-strain relationships for batch 1 and 2

3.4.2 Reinforcing Steel

The reinforcing steel comprised of No.3, 10M, 20M and 25M deformed bars. All the reinforcing steel was Grade 400 MPa with properties in accordance with CSA G30.18 (CSA, 2009), except for the No. 3 hoops, which were Grade 40 (yield strength of 40 ksi, 276 MPa). Five tension tests were performed per bar size in accordance with the A615/615-M016 Standard (ASTM, 2016). The loading machine provided axial force values while the axial displacement was recorded by an extensometer. From the stress-strain curves average steel properties were determined for each size of bar, namely the yield strength, f_y , ultimate strength, f_u , and strains at yielding, ϵ_y , at the initiation of strain hardening, ϵ_{sh} , and at ultimate strength, ϵ_u . Table 3.5 summarizes the

reinforcement properties obtained from tension tests. Figure 3.16 presents typical stress-strain relationships for the deformed bars.

Table 3.5: Reinforcing bar material properties

Bar size	f_y (MPa) (STDEV)	f_u (MPa) (STDEV)	ϵ_y (STDEV)	ϵ_{sh} (STDEV)	ϵ_u (STDEV)
No. 3*	332 (3.20)	517 (3.30)	0.00378 (0.00018)	-	0.150 (0.012)
10M	484 (17.00)	611 (15.70)	0.00242 (0.00008)	0.0258 (0.0019)	0.126 (0.001)
20M	459 (2.90)	597 (1.30)	0.00229 (0.00006)	0.0189 (0.0008)	0.125 (0.004)
25M	419 (2.20)	623 (1.00)	0.00210 (0.00001)	0.0096 (0.0005)	0.132 (0.010)

*Note: rounded stress-strain relationship, 0.2% offset stress used for yield

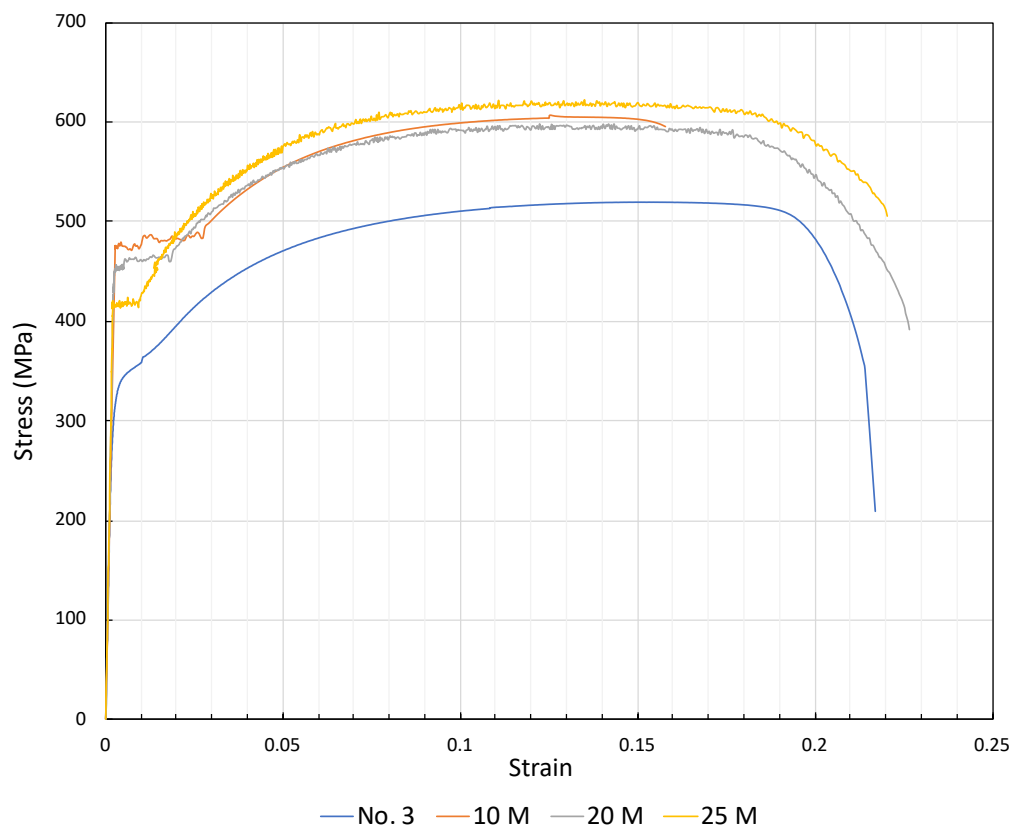


Figure 3.16: Typical tensile stress-strain relationships for reinforcing bars

In accordance with the 2019 CHBDC (CSA, 2019) provisions, the minimum amount of shear reinforcement, $\left(\frac{A_v}{s}\right)_{min}$, using the average material properties is:

$$\left(\frac{A_v}{s}\right)_{min} = \frac{0.06\sqrt{f'_c}b_w}{f_y} = \frac{0.06*\sqrt{36.7}*250}{332} = 0.274 \quad (3.2)$$

From Eq. 3.2, $\left(\frac{A_v}{s}\right)_{min}$, of 0.274 corresponded to a $\rho_v f_y$ of 0.363 MPa. It is noted that all of the specimens had transverse reinforcement exceeding this requirement (see Table 3.1).

3.5 Test Setup and Instrumentation

3.5.1 Test Setup

The column specimens were tested in the Jamieson Structures Laboratory in the Department of Civil Engineering at McGill University. The specimens were designed with end walls to represent column fixed end restraints and were tested in the custom-made coupled wall testing apparatus that has been used previously. The testing frame for all specimens is shown in Fig. 3.17 and Fig. 3.18.

The loading and reactions were applied to the walls of the specimen through loading beams located at the bases of each wall. At the free wall, the positive upward shear load was applied to the specimen at a location such that the line of action of the applied load passes through the midspan of the column. In the testing orientation it was assumed that the centroidal axes of the end walls remain parallel at each floor level while the column undergoes vertical deflection that would resemble column lateral deflection in a typical scenario as illustrated in Fig. 3.19. Figure 3.20 shows how the testing frame simulates the loading conditions.

The positive load was provided by two thirty-ton hydraulic jacks reacting against the strong floor. The maximum possible shear force was sixty tons, approximately 530 kN. A single thirty-ton hydraulic jack placed at the far end of the loaded wall applied load in order to balance the dead load of the specimen and testing apparatus to keep the two walls parallel throughout loading. The constant column axial load of 500 kN was provided by two 50-ton hydraulic jacks and four 25 mm diameter high-strength threaded rods.

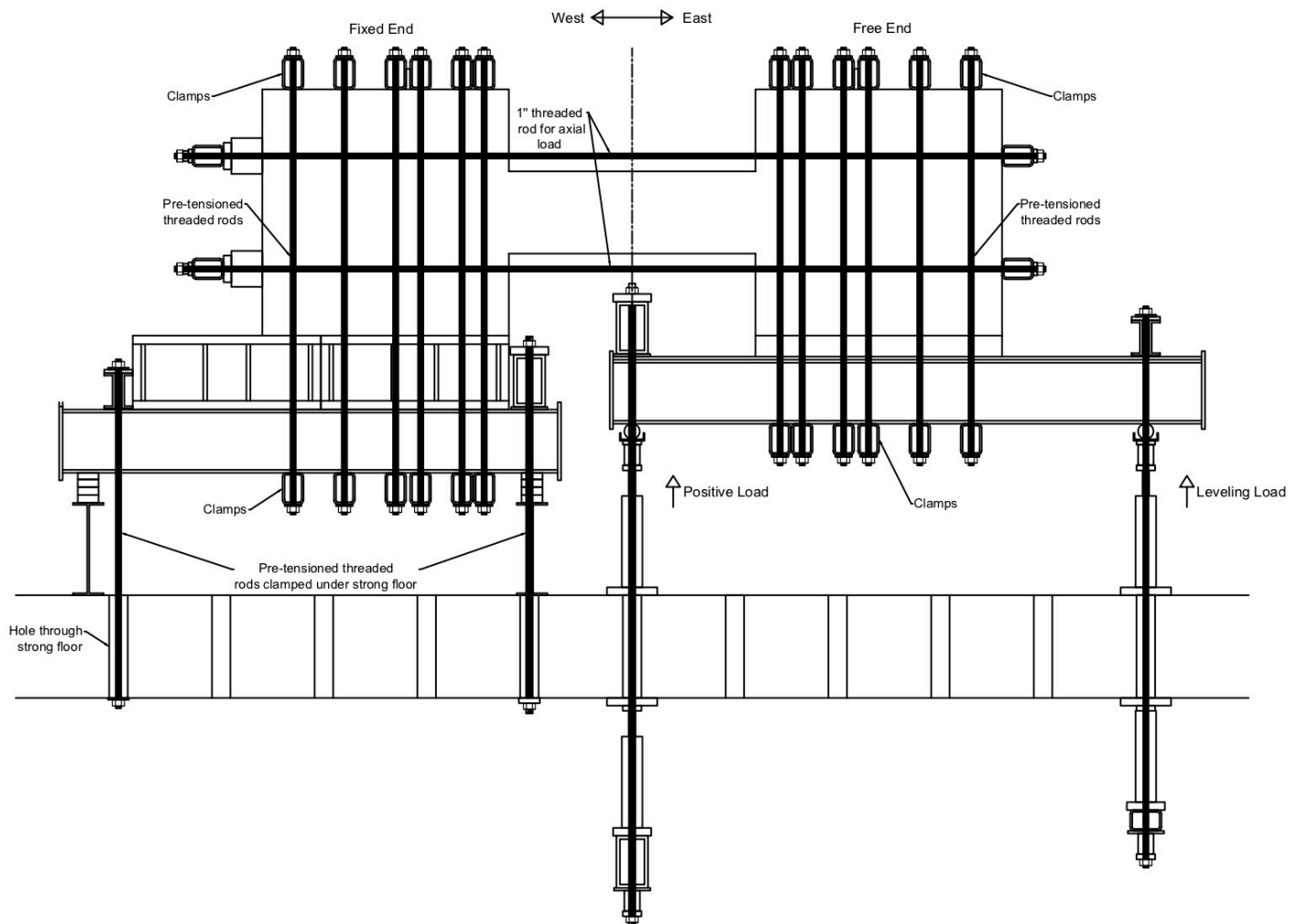


Figure 3.17: Illustration of McGill University testing frame

At the fixed end wall, the fixed boundary conditions were achieved by clamping the fixed beam to the strong floor and then clamping the specimen to the beam. On the east side of the fixed beam, two high-strength 1-1/2" (38 mm) diameter tension rods were pre-tensioned to 1000 kN. At the west end of the beam, two regular 1" (25 mm) diameter tension rods were pre-tensioned to 300 kN. The two end walls of the specimen were clamped to the loading and fixed beams using six pairs of tension rods respectively each pair pre-tensioned to 300 kN. That was typical for specimens M2, M3 and M4 only five pairs were used for specimen M1.

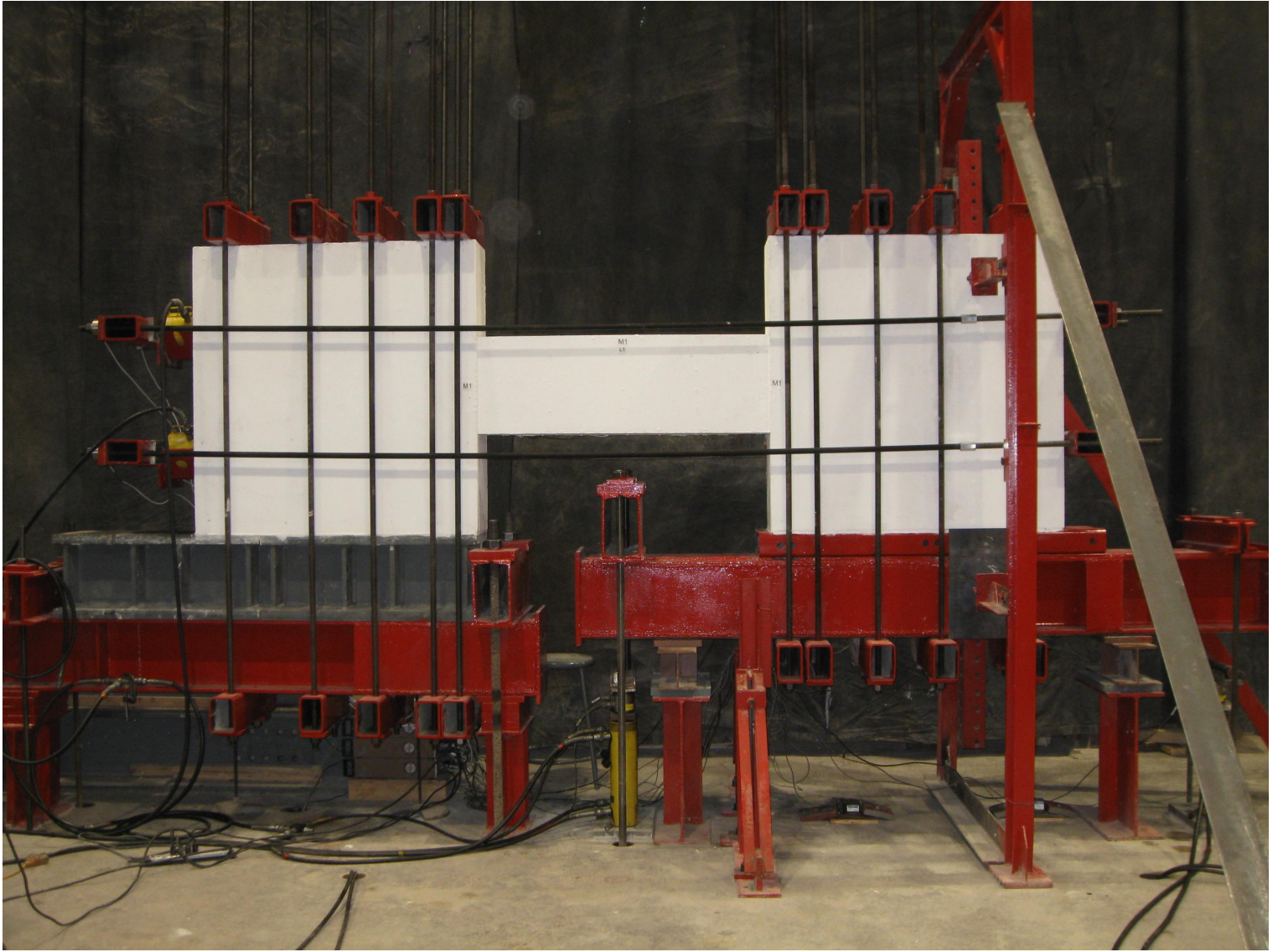


Figure 3.18: Photograph of McGill University custom testing frame

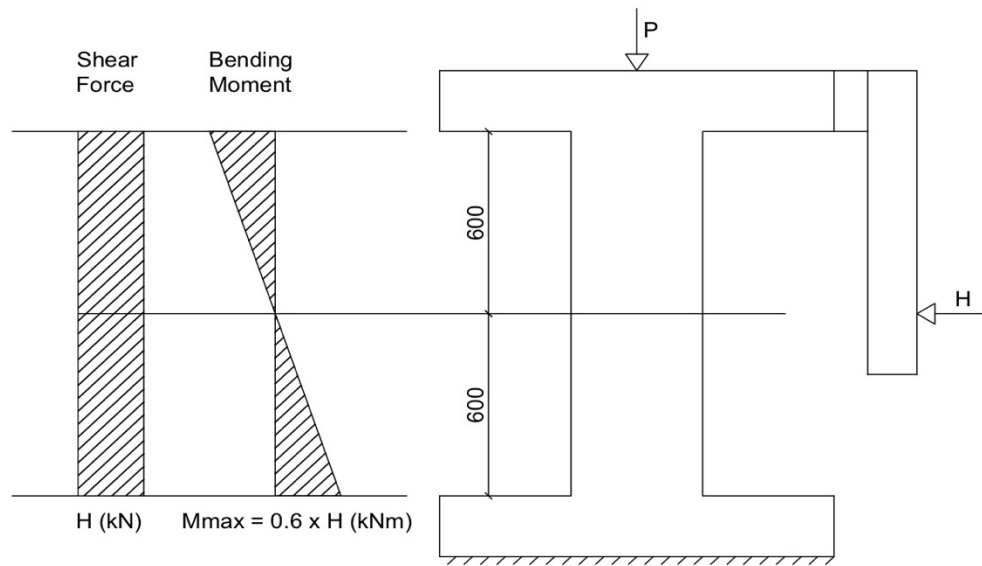


Figure 3.19: Column in upright position

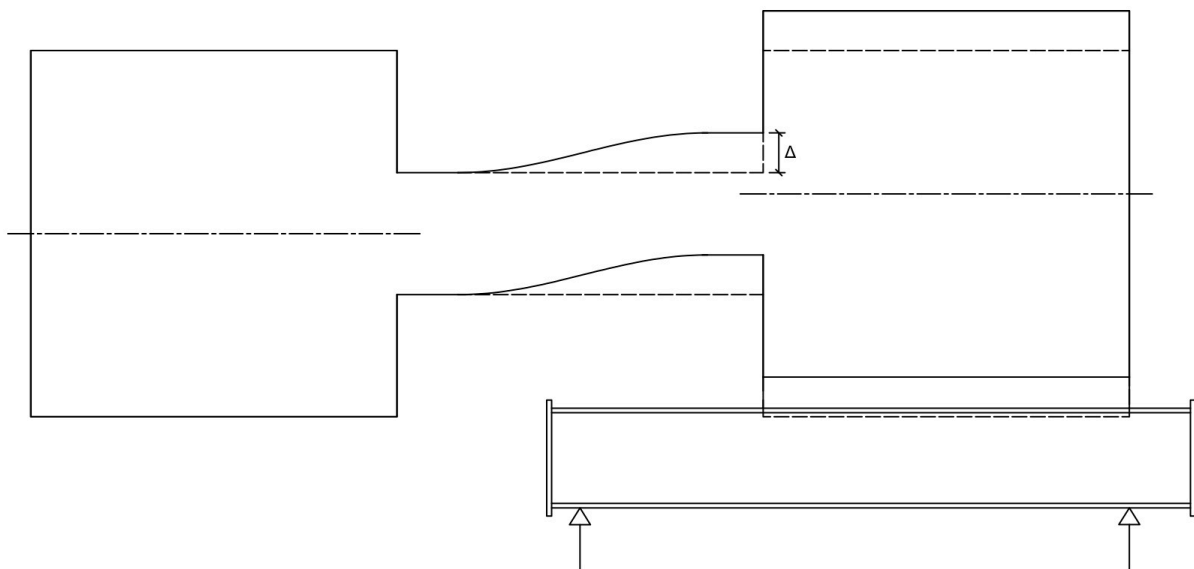


Figure 3.20: Deformation of a column test specimen

3.5.2 Instrumentation

The instrumentation comprising load cells, LVDTs and strain gauges were connected to a computer-controlled data acquisition system and displayed in real time during the tests. The data acquisition system also recorded the data for post processing analysis.

3.5.2.1 Load Measurements

Figure 3.21 shows the locations of the load cells (LC) used to measure the loads applied to the column specimens. The load cells measured the applied load in real time. Two 75-kip (333 kN) capacity load cells, LC-L-P-N and LC-L-P-S were installed above the strong floor to measure the external load applied through a line passing through the midspan of the column during the positive upward loading. One 75-kip (333 kN) capacity load cell, LC-S-P, was used to measure the external positive load applied by the leveling jack.

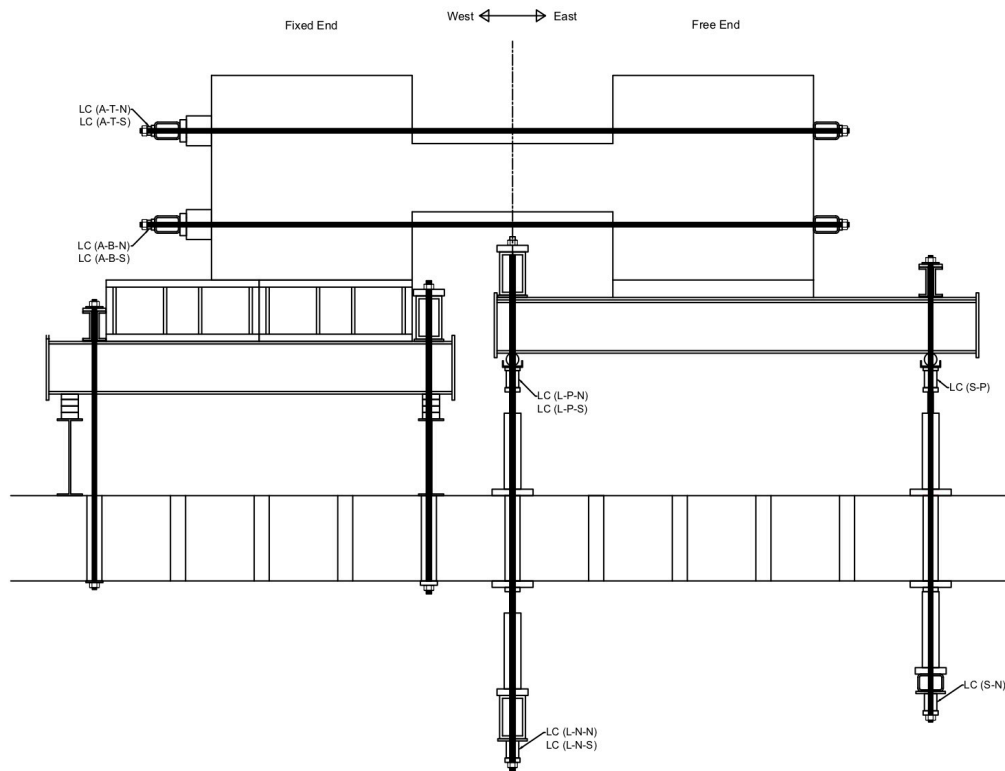


Figure 3.21: Load cell locations

Four 40-kip capacity load cells were installed at each end of the axial threaded rods LC-A-T-N, LC-A-T-S, LC-A-B-N and LC-A-B-S in order to monitor the column axial load applied by the jacks during the test.

3.5.2.2 Displacement Measurements

Figure 3.22 shows the locations of the linear variable differential transformers (LVDTs) used for all column specimens. When viewing instrumentation figures, one must note that the back of the specimen is shown. The instrumentation was installed on this side. Two 15-mm LVDTs and two string potentiometers measured the vertical displacements at the locations indicated, allowing for the differential displacements and corresponding rotations to be determined in real time. Through the control of the displacements and the applied loads, the vertical centroidal axes of the two end walls were kept as parallel as possible during testing. The relative displacement (Δ) of the loaded column was calculated using the translational displacement (Δ_T) the rotational displacement (Δ_θ) given in Eq. 3.3 to Eq. 3.6. The rotational displacement accounts for the differential slopes of the loading wall (LW) and fixed wall (FW). SP (S-A) measures the axial elongation.

$$\Delta_T = \left(\frac{\Delta_1 + \Delta_2}{2} \right) - \left(\frac{\Delta_3 + \Delta_4}{2} \right) \quad (3.3)$$

$$\Delta_{\theta LW} = \left(\frac{\Delta_2 - \Delta_1}{820} \right) \quad (3.4)$$

$$\Delta_{\theta FW} = \left(\frac{\Delta_3 - \Delta_4}{820} \right) \quad (3.5)$$

$$\Delta = \left(\Delta_2 + \frac{930}{820} (\Delta_2 - \Delta_1) \right) - \left(\Delta_3 + \frac{930}{820} (\Delta_3 - \Delta_4) \right) \quad (3.6)$$

Where,

$$\Delta_1 = \text{SP (S-E)}, \Delta_2 = \text{SP (S-W)}, \Delta_3 = \text{D (S-E)} \text{ and } \Delta_4 = \text{D (S-W)}$$

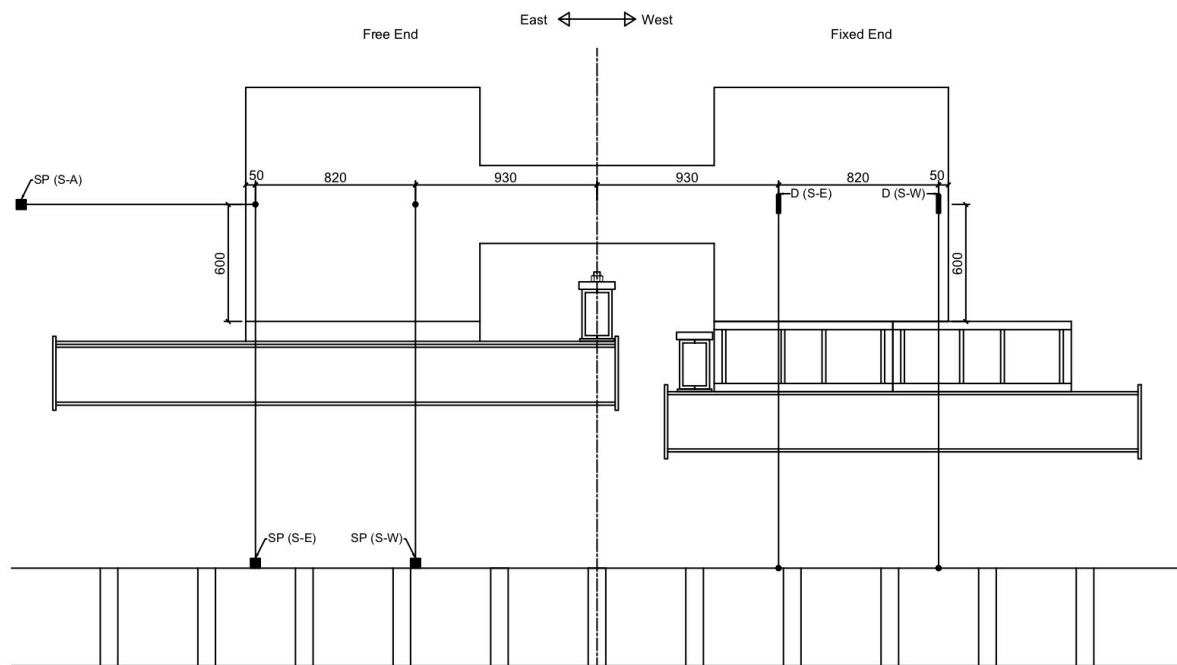


Figure 3.22: LVDT and string potentiometer locations

Each column had two rosettes one on the east side of the specimen and one on the west side (See Fig. 3.24), except for M1 specimen which had one rosette at the centre (see Fig. 3.25). Each rosette was made up of two 15-mm LVDTs in the horizontal (column centerline) direction and vertical (perpendicular to the centerline) direction and two diagonal 15-mm LVDTs at $\pm 45^\circ$ to the column centerline. The centre of each rosette was located at the mid-depth of the column, at a horizontal distance of 265 mm from the face of column support. The gauge length of the rosette LVDTs was 260 mm. The rosettes were used to determine the principal strains and the angles of principal compressive strains. Four 25-mm LVDTs were used to measure the elongation of the 25M reinforcing bars at the top and bottom east and west corners of the specimen. Additionally four 25-mm LVDTs were used to measure the yield penetration of the 25M bars at the top and bottom east and west corners of the column. Details of the LVDTs are shown in Fig. 3.23.

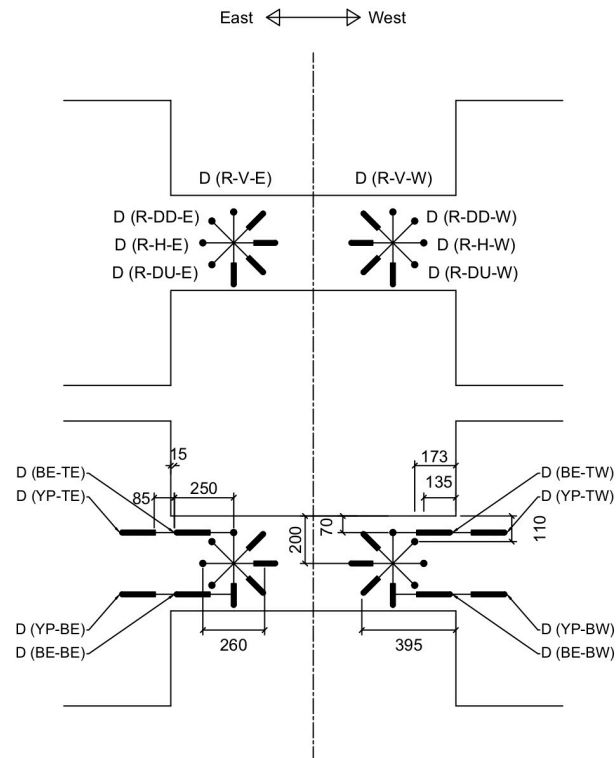


Figure 3.23: LVDT schematics closeup

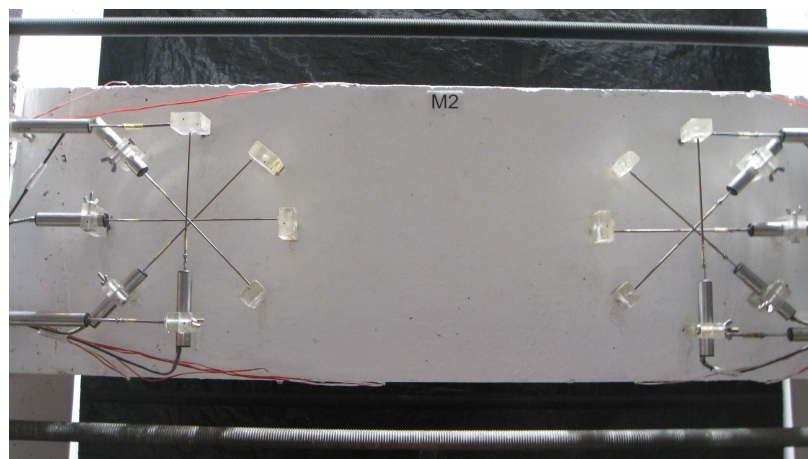


Figure 3.24: Typical LVDT configuration for specimens M2, M3 and M4

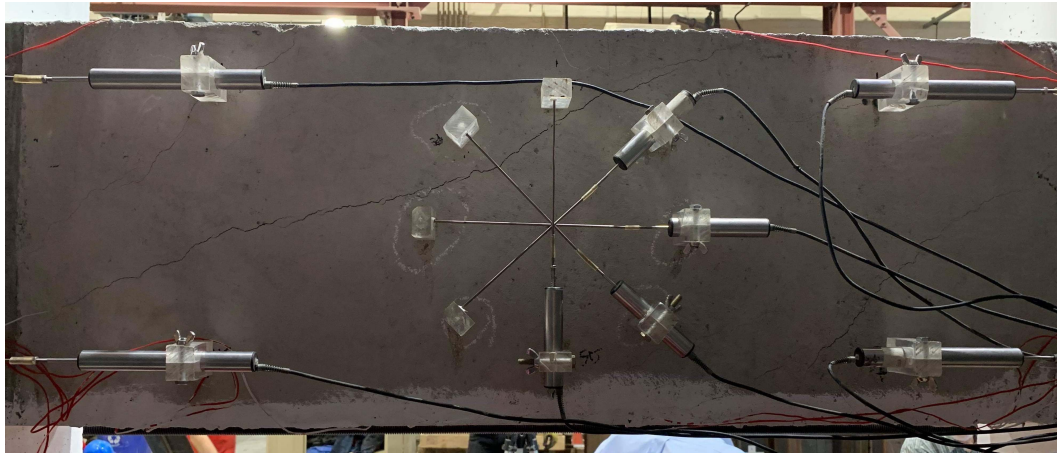


Figure 3.25: LVDT configuration for specimen M1

3.5.2.3 Strain Measurements

A total of six strain gauges with 5-mm gauge length were installed on two 25M longitudinal bars. Strain gauges were installed at three locations on a top and a bottom bar respectively, this was typical for all four specimens. In addition, six strain gauges with 2-mm gauge length were installed on the No. 3 transverse hoops. The No. 3 strain gauges were installed on different hoops for each specimen. Figures 3.26 and 3.27 show the locations of the strain gauges installed on the reinforcing bars embedded in the concrete for each specimen. Each specimen had a total of 12 strain gauges. The strain gauges on the hoops were closely monitored during the test in order to observe the first yielding of the transverse reinforcement.

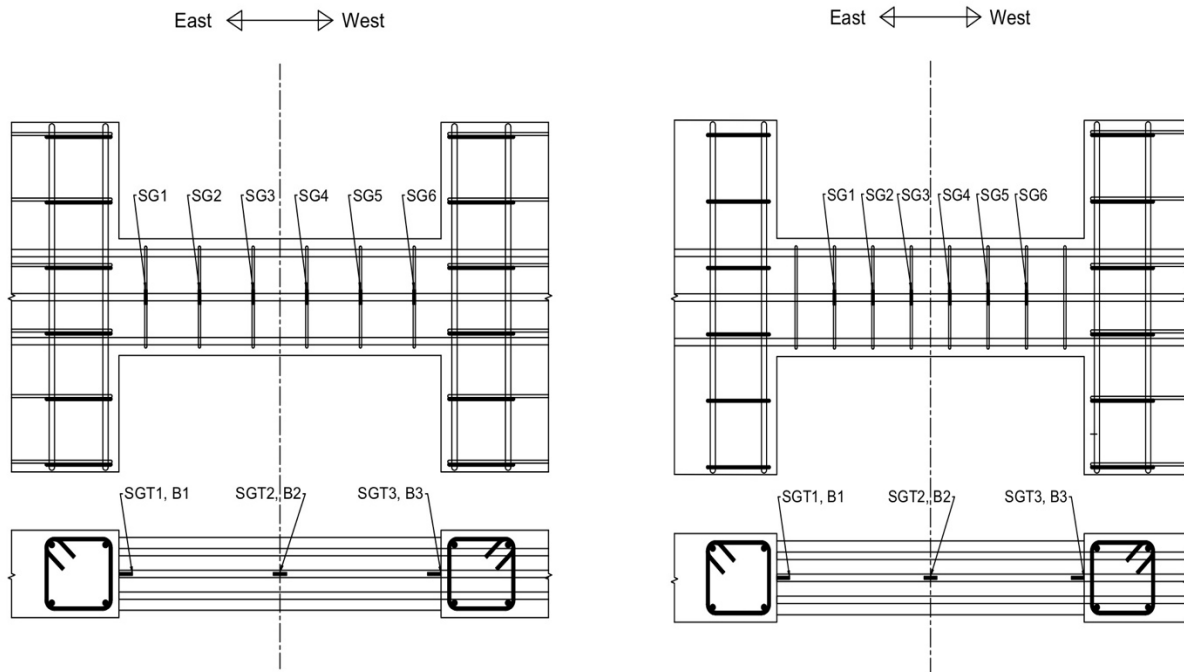


Figure 3.26: Strain gauge configuration for M1 (left) and M2 (right)

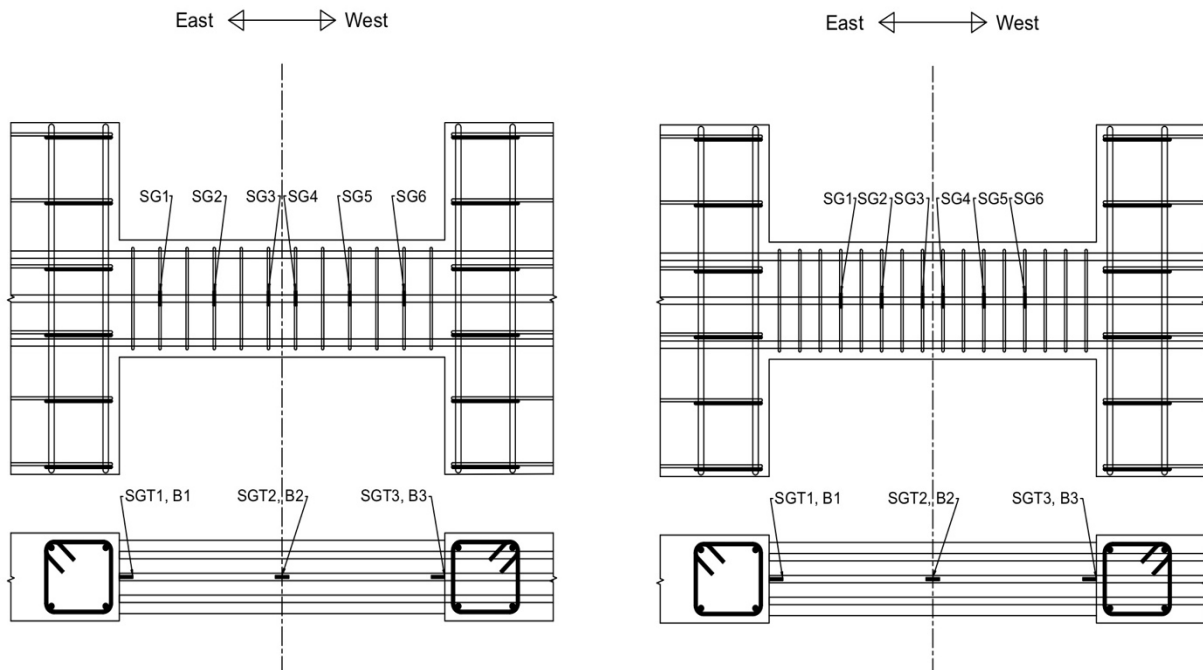


Figure 3.27: Strain gauge configuration for M3 (left) and M4 (right)

3.6 Experimental Procedure

Each column was subjected to a monotonic loading scheme at pre-determined loading stages. The load stages were separated into two types of loading: load-controlled and deflection-controlled. The specimens were initially tested under load control. First step was to pick up the specimen and zero the data acquisition system. The first load stage was estimated to cause flexural cracking. In all cases first cracking was observed at this load stage. The subsequent load-controlled stages consisted of load stages corresponding to:

1. first yielding of a No. 3 hoop
2. general yielding of transverse reinforcement.

The column failed in shear when the load applied dropped suddenly and the maximum shear load was recorded. After the peak shears were reached the specimens were loaded in deflection-control. The displacement at which the maximum shear force is recorded is established as the peak displacement, Δ_{peak} . The deflection targets were multiples of the deflection of the specimen at shear failure.

Testing was paused after each load stage to mark and measure the crack widths, and to take photographs of the crack patterns. As the applied shear was increased the axial load applied could rise above the target 500 kN. The axial load was monitored closely and adjusted accordingly if needed to ensure that the applied axial load was kept constant at 500 kN.

4 Experimental Results

4.1 Introduction

The behaviour of the four column specimens is described in this chapter. The data presented was recorded during the specimen testing by a computerized data acquisition system along with crack width measurements and photographs. Each specimen was subjected to a monotonic loading scheme at pre-determined loading and deflection stages. The specimens were initially subjected to load-controlled cycles until the column failed in shear. After the peak shear was reached the specimens were loaded in deflection control.

4.2 Response of Specimen M1

4.2.1 Shear-Deflection Response

The shear versus deflection response is given in Table 4.1 along with the measured maximum crack width at each load stage.

Table 4.1: Shear-deflection response of specimen M1

Load Stage	Description	Applied Shear (kN)	Deflection (mm)	Axial Load (kN)
L0	Balance self-weight	0	0	0
L1	Add axial load	0	0	500
L2	First flexural cracking	149	1.11	
L3	Hairline flexural cracks	203	2.01	
L4	First shear crack on west side	225	2.62	
L5	First shear crack on east side	225	2.69	
L6	Shear crack 0.15 mm	238	3.34	
L7	Shear crack 0.2 mm	245	3.47	
L8	Shear crack 0.25 mm	253	3.79	
L9	Shear crack 0.3 mm	261	4.09	
L10	First transverse hoop yielding	269	4.44	
L11	Shear crack 0.35 mm	278	4.62	
L12		286	5.00	
L13	Shear crack 0.5 mm	295	5.44	
L14		301	5.30	
L15		310	6.10	
L16	Shear crack 0.6 mm	320	6.33	
L17	Shear crack 0.7 mm	330	7.01	
L18	Peak load	339	7.62	
L19	1.8 Δ_{peak}	330	13.57	
L20	3.0 Δ_{peak}	215	22.67	
	6.4 Δ_{peak}	140	48.90	

The shear force versus deflection response is shown in Fig. 4.1. First flexural cracking of the column occurred during load stage 2 at a load of 149 kN and a deflection of 1.11 mm. The first and second hairline crack initiated at the top right and bottom left corner of the column, respectively at load stage 3 at a load of 203 kN and a deflection of 2.01 mm. The first signs of hairline inclined cracking were observed at a shear of 225 kN. The column reached a maximum shear of 339 kN and a deflection of 7.62 mm followed by a sudden drop in shear, indicating a shear failure. After the column failed in shear, it was capable of resisting load due to the deflection control that was imposed. The specimen was loaded further, in deflection control, up to a deflection of 48.9 mm which was 6.4 times the deflection at the peak shear level. At this load stage the shear was 140 kN, which was 40% of the peak shear after which it was decided to stop the test.

The compressive axial load was applied and maintained at 500 kN, the axial load versus applied shear is shown in Fig. 4.2.

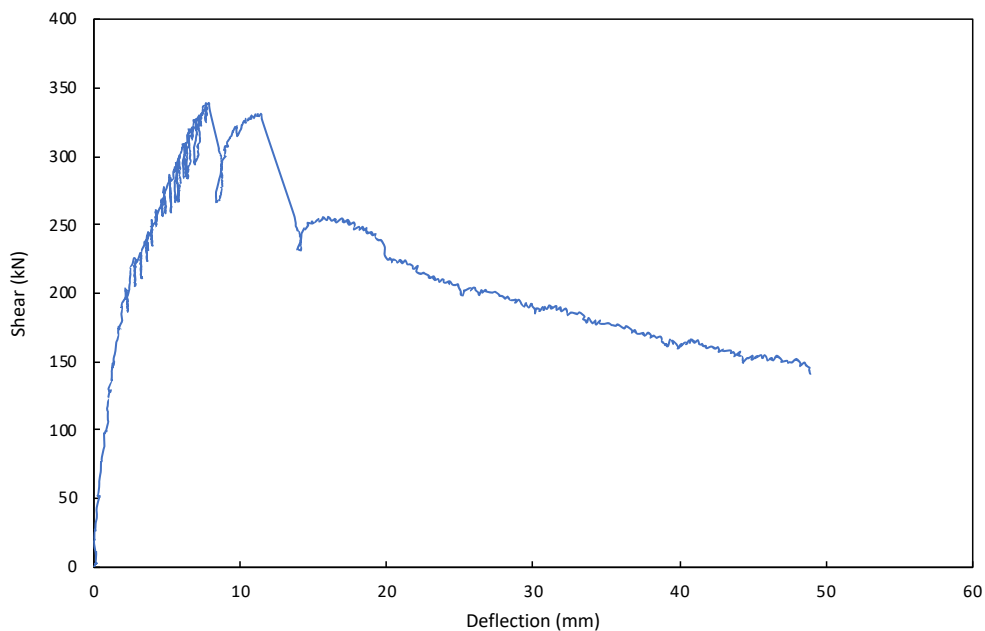


Figure 4.1: Shear versus deflection response of specimen M1

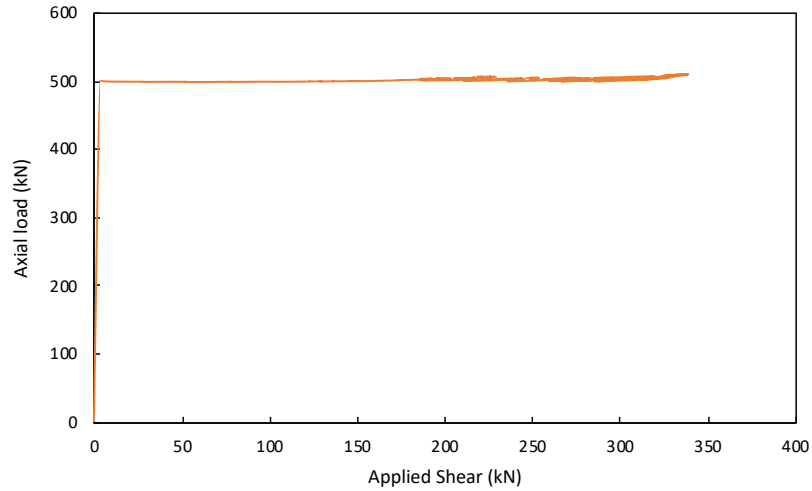


Figure 4.2: Axial load versus applied shear for specimen M1

4.2.2 Shear Failure

The shear failure can be seen in Fig. 4.3. The 1.5 mm wide critical shear crack started approximately 100 mm from the bottom east corner of the column and ended 300 mm from the top west corner of the specimen. The second to last transverse hoop on the west side located in the critical shear region experienced considerable yielding before shear failure occurred. The specimen was loaded further after the shear failure, up to a displacement of 48.9 mm. At this stage, significant concrete spalling had occurred. The specimen in the final displaced position is shown in Fig. 4.4.



Figure 4.3: Shear failure of specimen M1

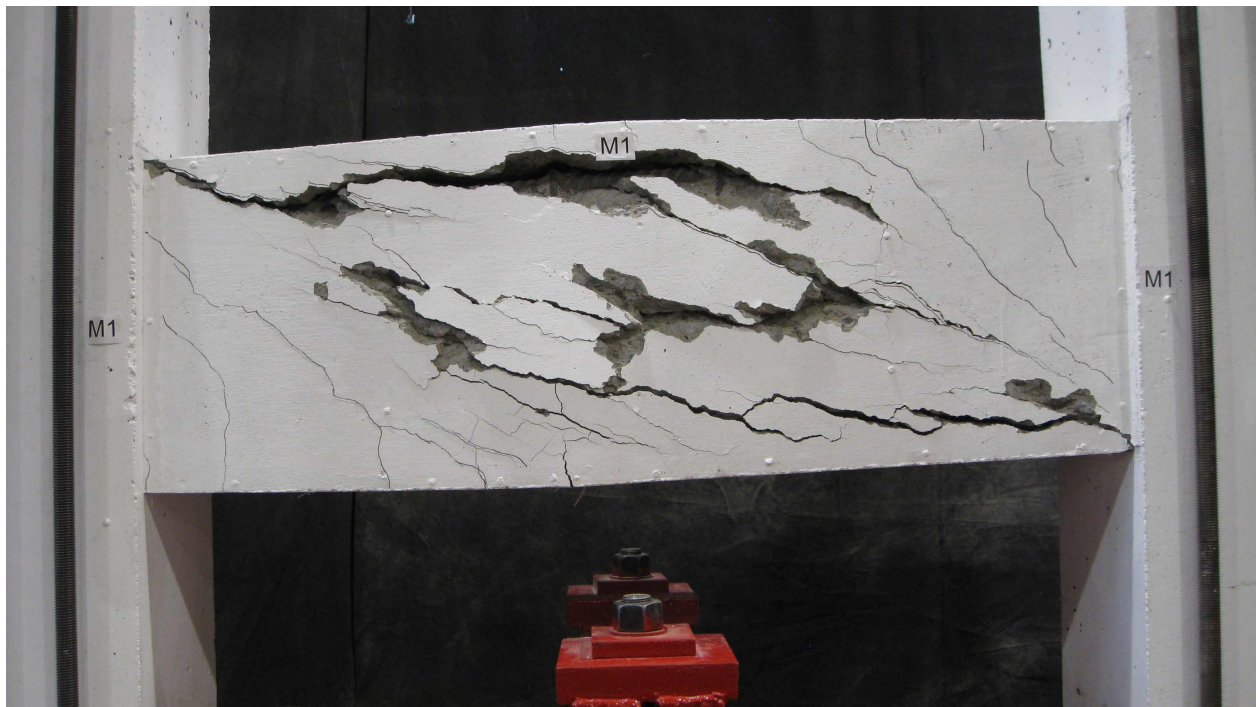


Figure 4.4: Specimen M1 in final displaced position

4.2.3 Crack Widths

The first shear cracks occurred at a load of 225 kN and a deflection of 2.62 mm. Two shear cracks located in the critical shear region on the west side and east side formed at this load level. All hoops except the ones located at the centre of the column had picked up exhibited increased strains at this load level. The existing cracks extended and widened, during the subsequent load stages. The shear versus maximum crack widths for the east and west sides are shown in Fig. 4.5 and Fig. 4.6, respectively. Before the shear failure, at shears between 320 and 330 kN, maximum crack widths of 0.7 mm and 0.6 mm on the west and east side were observed, respectively. A maximum flexural crack width of 0.05 mm was observed on the west side. Shear cracks were consistently very close in value between the west and east sides of the column. A critical 1 mm wide shear crack opened up when maximum shear was attained. The critical crack continued to grow to a width of 1.5 mm after reaching the peak shear.

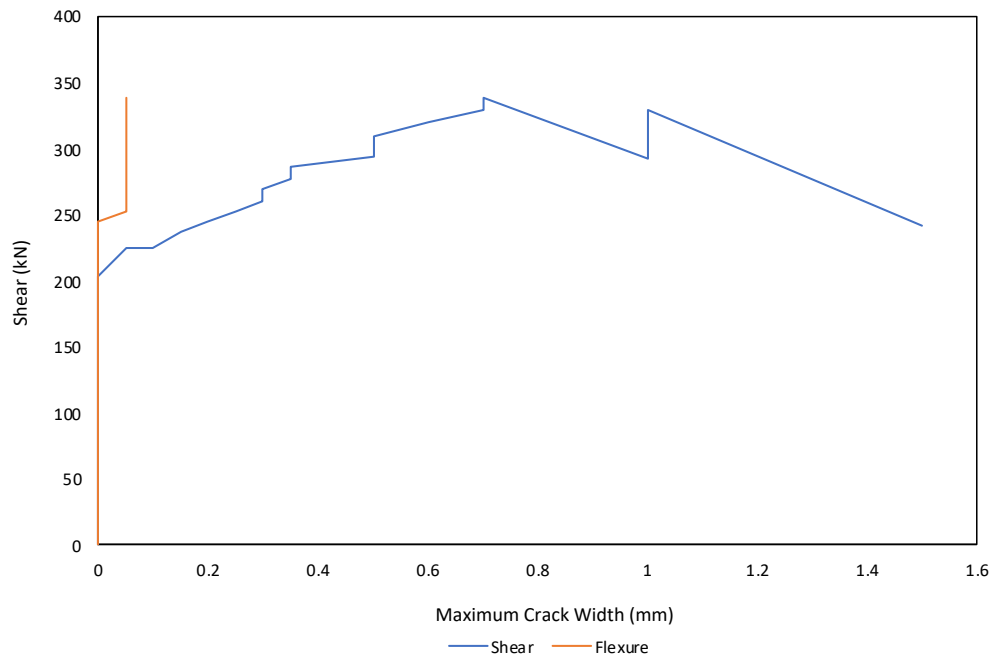


Figure 4.5: Shear versus maximum crack widths for west side of specimen M1

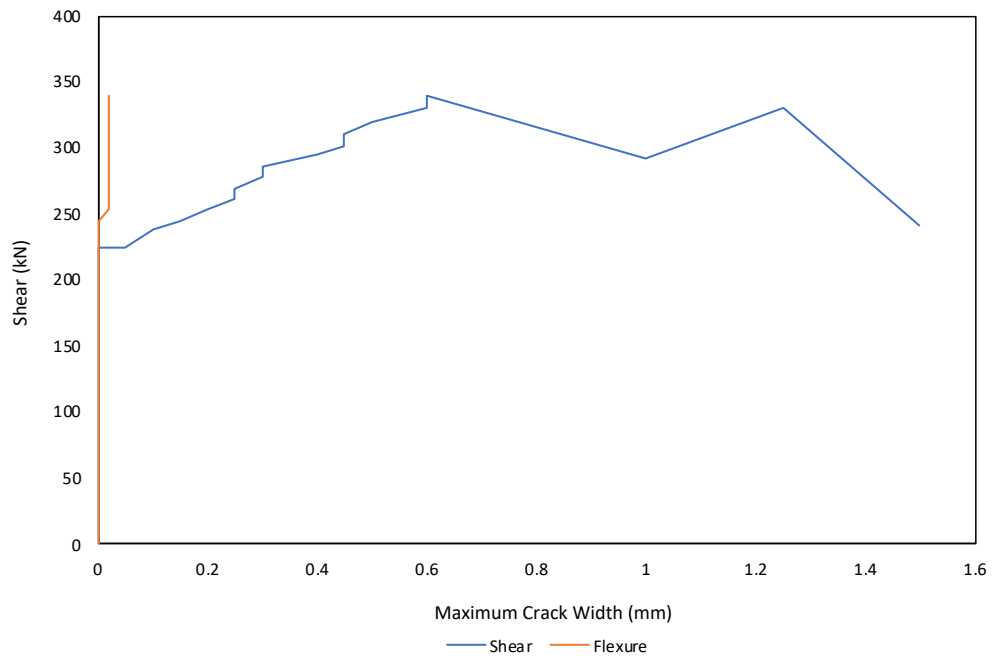


Figure 4.6: Shear versus maximum crack widths for east side of specimen M1

Figures 4.7 and 4.8 show the cracking that occurred at shears of 225 kN and at the peak shear level of 339 kN, respectively.



Figure 4.7: Crack pattern and widths at a shear of 225 kN for specimen M1



Figure 4.8: Crack pattern and widths at peak shear of 339 kN for specimen M1

4.2.4 Measured Strains

The shear versus strain relationships for the No. 3 hoops are shown in Fig. 4.9. Strain gauge, SG5, located on the hoop 300 mm from the west end of the column, was the first to reach the yield strain of 0.0016 of the No. 3 bars. This first yielding of the transverse reinforcement occurred at a shear of 261 kN. It is noted that, at this load level, the maximum shear crack width was 0.30 mm on the west end. On the east end strain gauges, SG1 and SG3, reached yielding at a shear of 310 kN while strain gauge, SG2, yielded at a shear of 332 kN. On the west end only strain gauge, SG5, yielded before the peak shear was reached, however strain gauge, SG4, yielded at a shear of 319 kN after the shear failure when the critical shear crack had opened significantly. After yielding strain gauge, SG4, was showing significant strains and malfunctioned immediately after. Finally, strain gauge, SG6, located 200 mm from the face of the column on the west side never yielded but reached a maximum strain of 0.0009 at a shear of 238 kN after the shear failure.

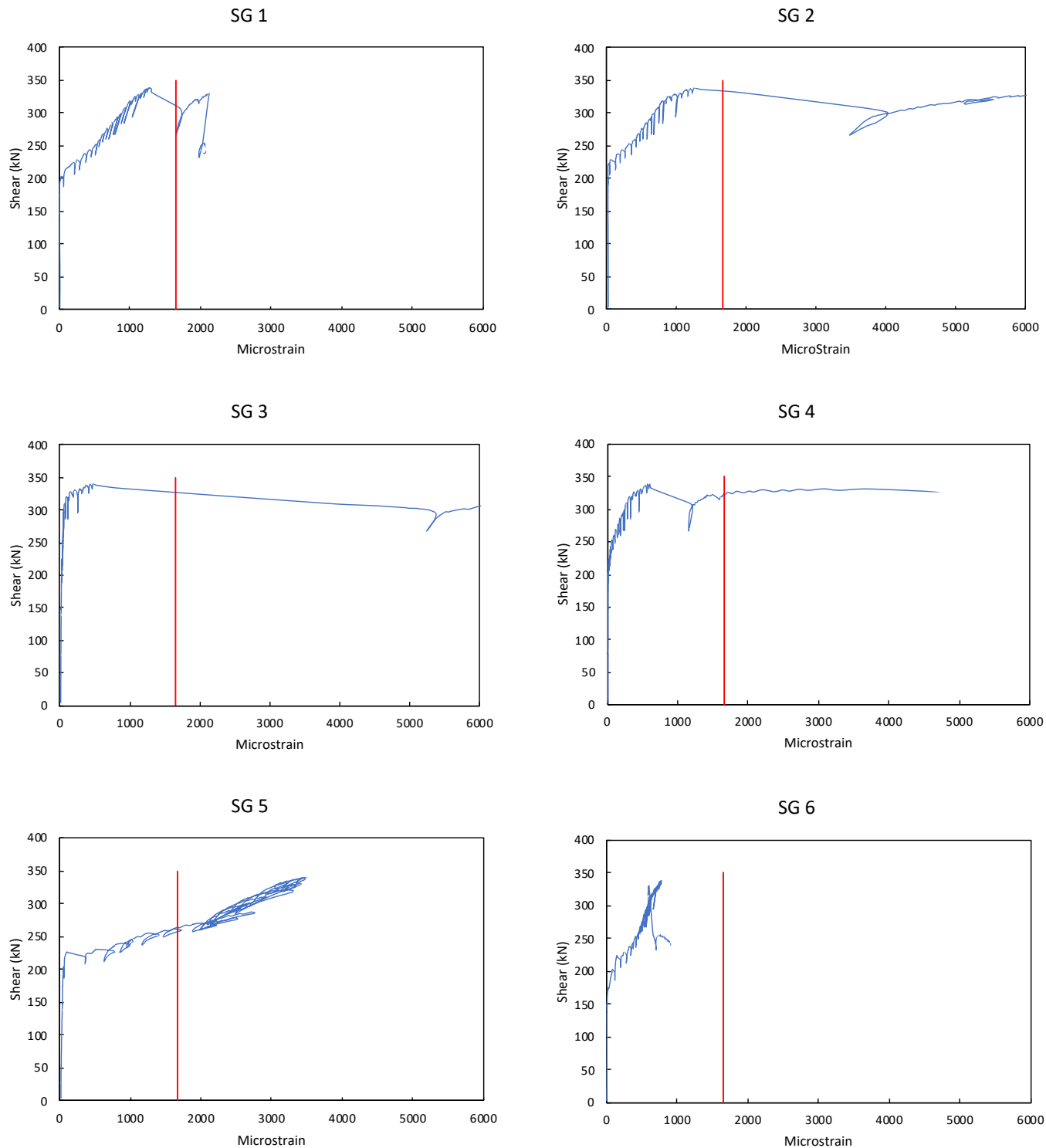


Figure 4.9: Shear versus strain for transverse hoops in specimen M1

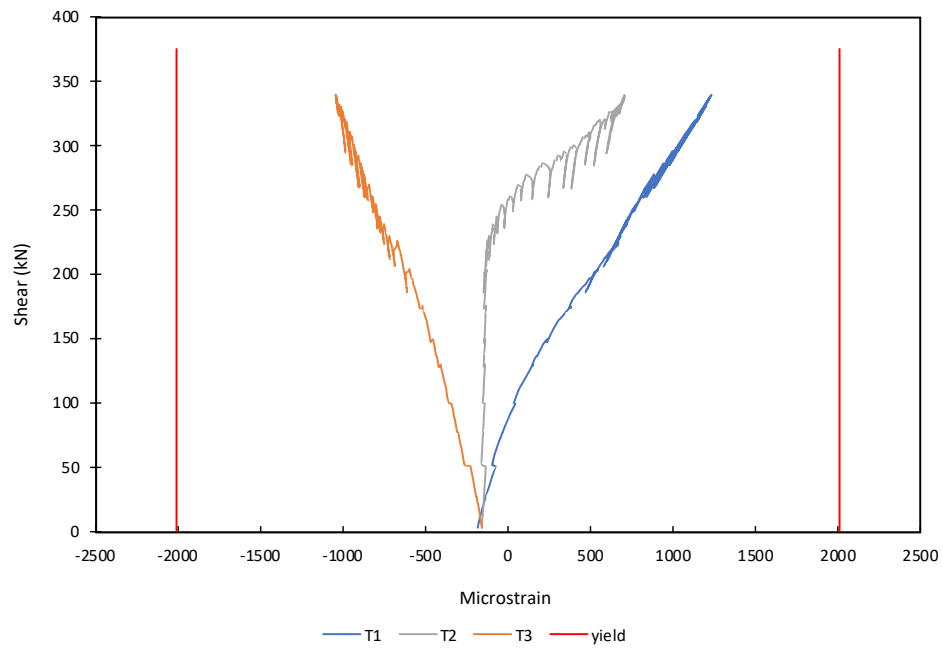


Figure 4.10: Shear versus strain for top longitudinal bar in specimen M1

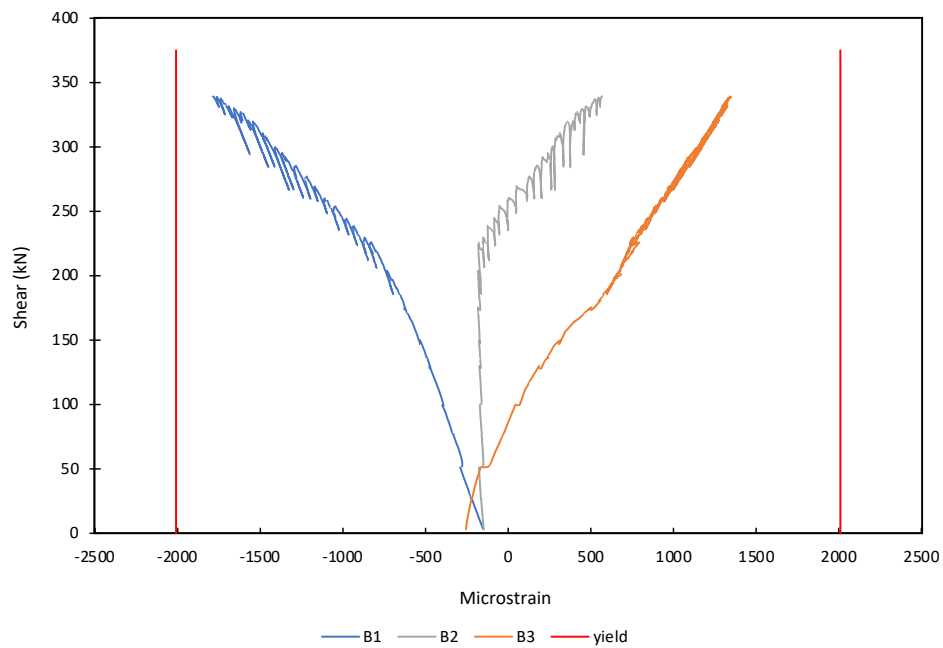


Figure 4.11: Shear versus strain for bottom longitudinal bar in specimen M1

Strain gauges were placed at three different locations on one 25M top bar and on one 25M bottom bar (see Fig. 3.26). Figures 4.10 and 4.11 show the shear versus strain relationships for these strain gauges. All strains started with a negative strain as the column was under axial compression before shear was applied to the column. When shear was applied on the column strain gauge top east gauge, T1, experienced tensile strains after cracking and bottom east gauge, B1, experienced increased compressive strains due to the moment. Similarly, bottom west gauge, B3, experienced tension and top east gauge, T3, experienced increasing compressive strains. Central strain gauges, T2 and B2, stayed in compression up to a shear of 220 kN before they experienced tensile strains. None of the strain gauges on the longitudinal 25M bars reached the yield strain of 0.0021.

The bar elongations were measured by four LVDTs in order to obtain the average strains in the bars. The average strain was determined over a gauge length of 250 mm. Initially under the axial load only, all of the average strains were negative, indicating compressive strains. The highest average strain at failure was 0.00429 in tension on the top east LVDT.

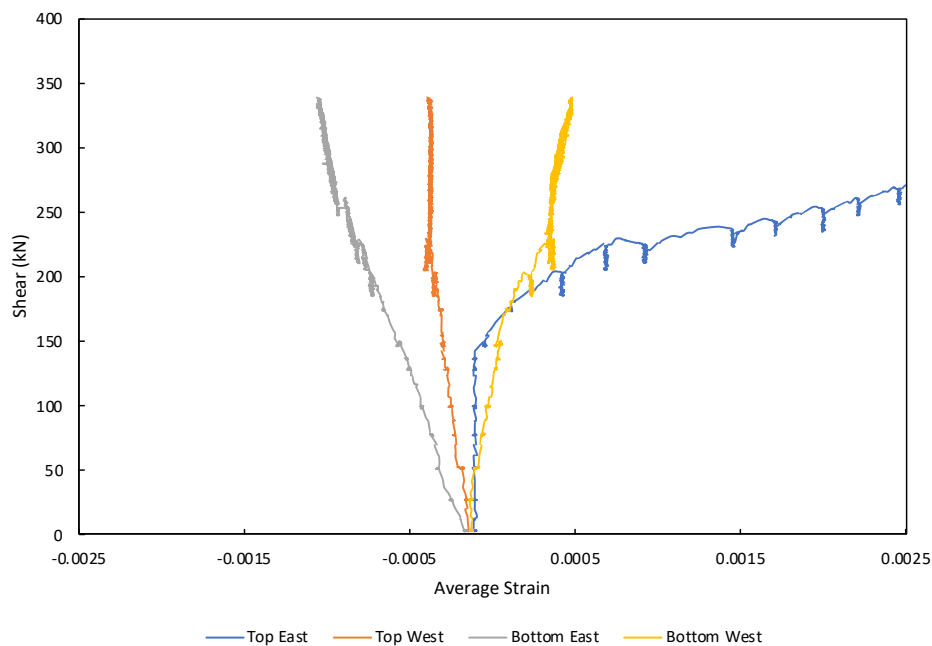
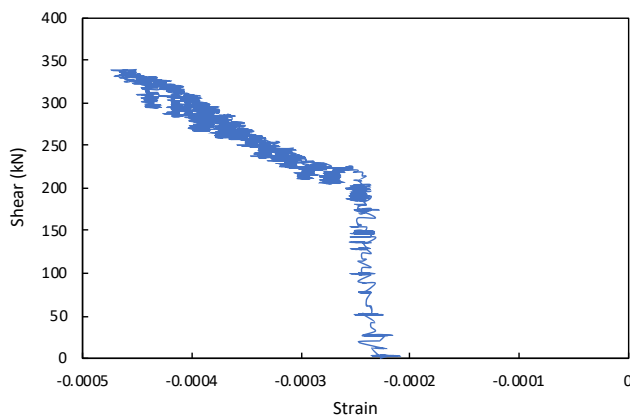


Figure 4.12: Average bar elongation strains for specimen M1

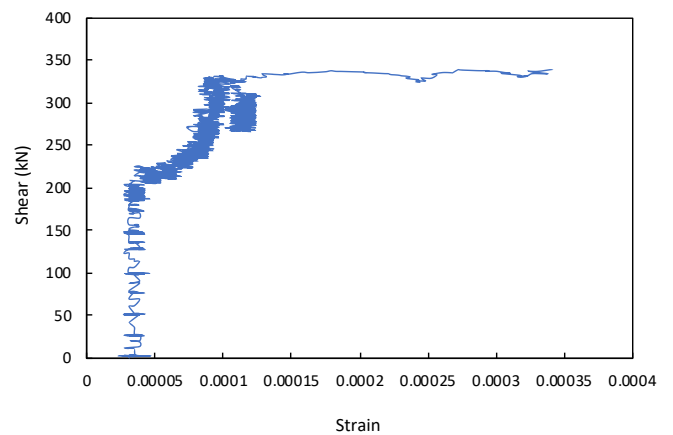
At the peak shear, all three LVDTs were below the yield strain of 0.0021 of the 25M bars.

Figure 4.12 shows the shear versus average strain relationships for each LVDT.

Figure 4.13 shows the results from the LVDTs, placed to form a rosette, on specimen M1. For specimen M1 the strain rosette was located at the centre of the column length (see Fig. 3.25). The horizontal strain, ϵ_x , at mid depth started negative under axial compression and increased to a strain of -0.0004596, when maximum shear was reached. The vertical strain, ϵ_y , remained negligible up to a shear of 200 kN after which it started to increase, coinciding with the formation of the first shear crack. At a shear of about 290 kN the vertical strain increased reaching a maximum of 0.000343 at the maximum shear level, which is less than the yield strain of 0.0016 of the No. 3 transverse hoops. The strain gauges on the central hoops, SG3 and SG4, didn't reach the yield level at failure. The principal tensile strain, ϵ_1 , at failure was 0.036%. Shear strain, γ_{xy} , at failure was 0.021%. The principal angle, θ_p , during failure was 25.8° .

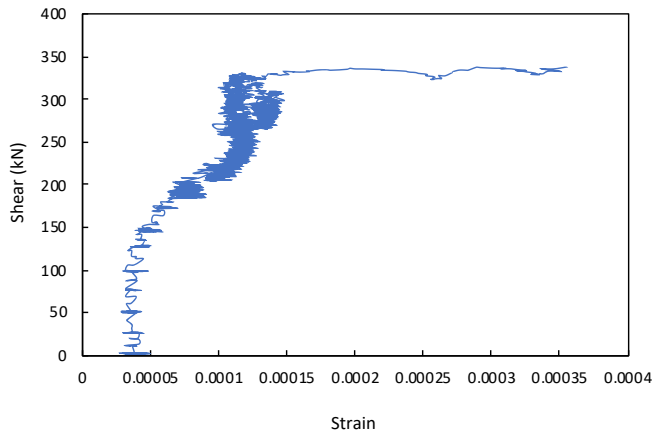


a) horizontal strain, (ϵ_x)

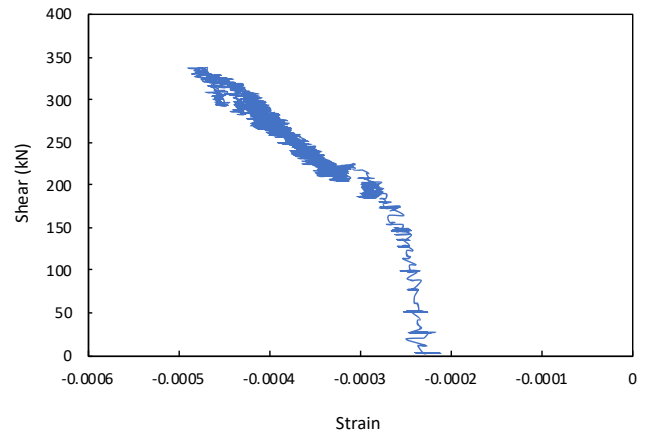


b) vertical strain, (ϵ_y)

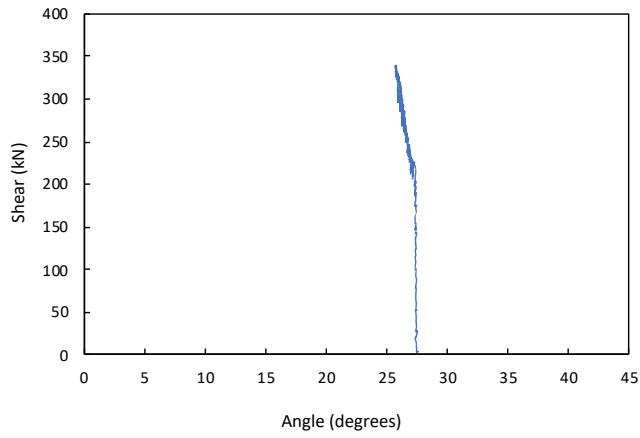
Figure 4.13: Principal strain and angle from specimen M1 rosette



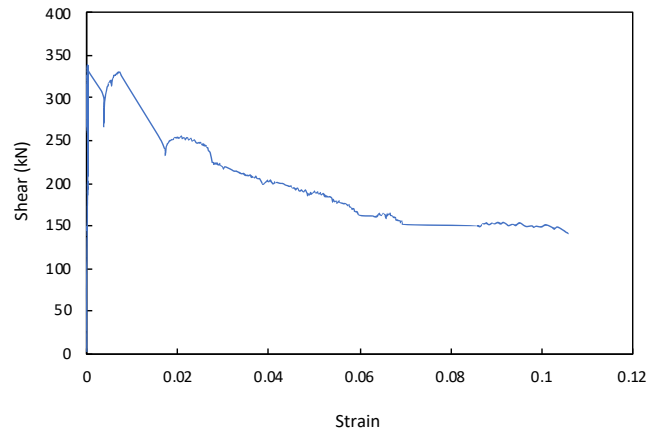
c) principal tensile strain, (ϵ_1)



d) principal compressive strain, (ϵ_2)



e) principal angle, (θ_p)



f) shear strain, (γ_{xy})

Figure 4.13 cont.: Principal strain and angle from specimen M1 rosette

4.3 Response of Specimen M2

4.3.1 Shear-Deflection Response

The shear versus deflection response is given in Table 4.2 along with the measured maximum crack width at each load stage.

Table 4.2: Shear-deflection response of specimen M2

Load Stage	Description	Applied Shear (kN)	Deflection (mm)	Axial Load (kN)
L0	Balance self-weight	0	0	0
L1	Add axial load	0	0	500
L2	First flexural cracking	151	1.55	
L3	Hairline flexural cracks	204	2.52	
L4	First shear crack	226	3.03	
L5	Shear crack 0.1 mm	240	3.37	
L6	Shear crack 0.15 mm	252	3.88	
L7		263	4.12	
L8	Shear crack 0.2 mm	283	5.09	
L9	Shear crack 0.25 mm	301	5.76	
L10	Shear crack 0.3 mm First transverse hoop yielding	321	6.71	
L11	Shear crack 0.4 mm	312	8.28	
L12	Shear crack 0.6 mm	344	10.05	
L13	Shear crack 0.75 mm	363	11.55	
L14	Peak load Yielding of all transverse reinforcement	366	12.56	
L15	1.5 Δ_{peak}	287	18.74	
L16	2.3 Δ_{peak}	245	28.41	
L17	4.4 Δ_{peak}	183	55.00	

The shear force versus deflection response for specimen M2 is shown in Fig. 4.14. First flexural cracking of specimen M2 occurred during load stage 2 at a load of 151 kN and a deflection of 1.55 mm. During load stage 3, the second hairline crack initiated at the top right corner of the column. The second and third hairline cracks appeared on the bottom left corner of the column. At load stage 3 the load was 204 kN and the deflection was 2.52 mm. The column specimen reached a shear of 366 kN and a deflection of 12.56 mm before a sudden drop in shear to 315 kN, indicating a shear failure. After the column failed in shear, the specimen was loaded, in deflection control, to a deflection of 55 mm which was 4.4 times the deflection at the peak. At this stage the shear had dropped to 183 kN, which is 50% of the peak shear after which it was decided to stop the test.

The compressive axial load was applied and maintained at 500 kN, the axial load versus applied shear is shown in Fig. 4.15.

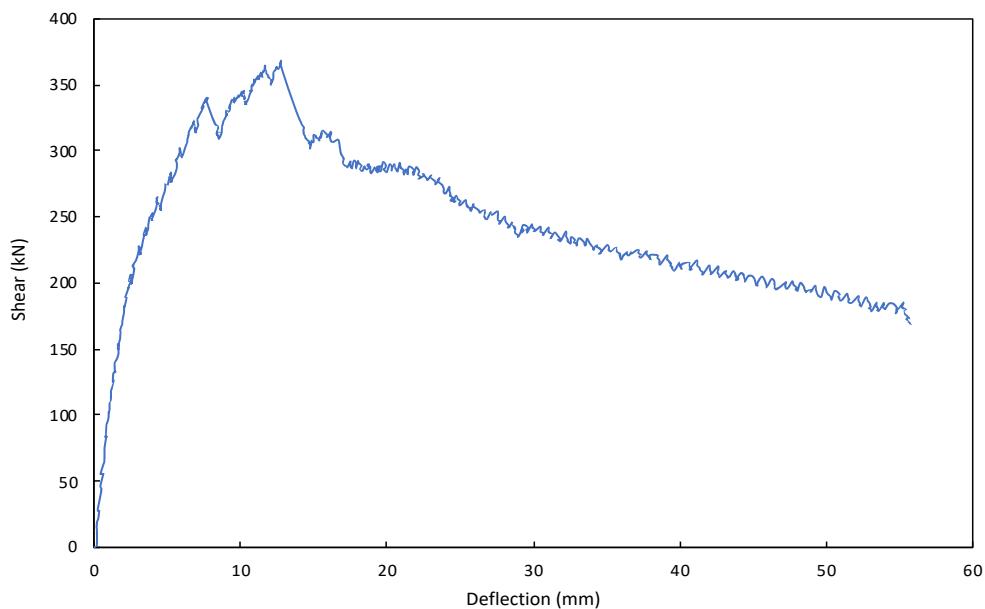


Figure 4.14: Shear versus deflection response of specimen M2

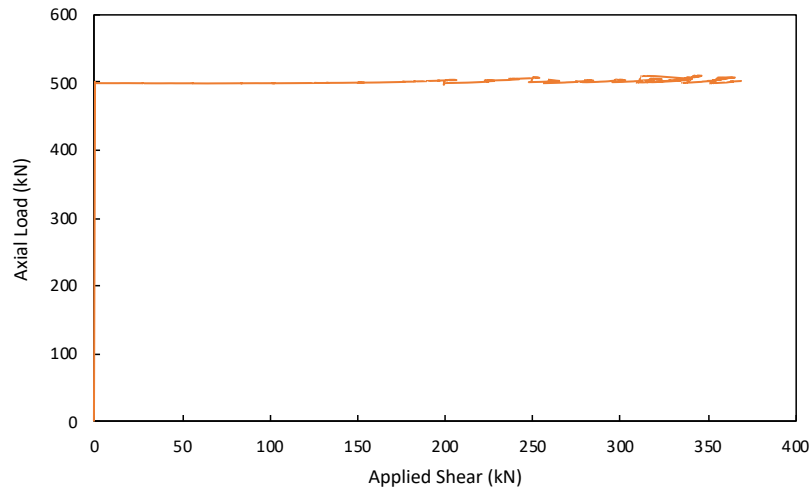


Figure 4.15: Axial load versus applied shear for specimen M2

4.3.2 Shear Failure

The shear failure can be seen in Fig. 4.16. The 0.8 mm wide critical shear crack started approximately 100 mm from the bottom corner of the column on the east end and ended 200 mm from the top west corner of the column. All transverse hoops monitored, yielded before the maximum shear was reached. The third to last transverse hoop on the east side located in the critical shear region, experienced a strain approximately 6 times the yield strain of No. 3 transverse hoops. After the column failed in shear, it was loaded further, up to a displacement of 55 mm. The specimen in the final displaced position is shown in Fig. 4.17.



Figure 4.16: Shear failure of specimen M2



Figure 4.17: Specimen M2 in final displaced position

4.3.3 Crack Widths

The first shear cracks occurred at a load of 226 kN and a deflection of 3.03 mm. At this load level one shear crack started in the critical shear region on the west and east end, respectively. Only the third to last transverse hoop on the east side located 375 mm from the column end had picked up considerable strain at this point. The existing cracks extended and widened, and two more shear cracks initiated during the subsequent load stages, one on each end of the column. A critical 0.75 mm wide shear crack opened up when the maximum shear was reached. The maximum crack widths for the east and west sides are shown in Fig. 4.18 and Fig. 4.19, respectively. Before shear failure, at a shear of 363 kN, maximum crack widths of 0.4 mm and 0.6 mm on the west and east side were observed respectively. A maximum flexural crack width of 0.15 mm was observed on both sides. Shear cracks and flexural cracks were consistently very close in value between the west and east ends of the column. The critical crack continued to grow to 0.8 mm.

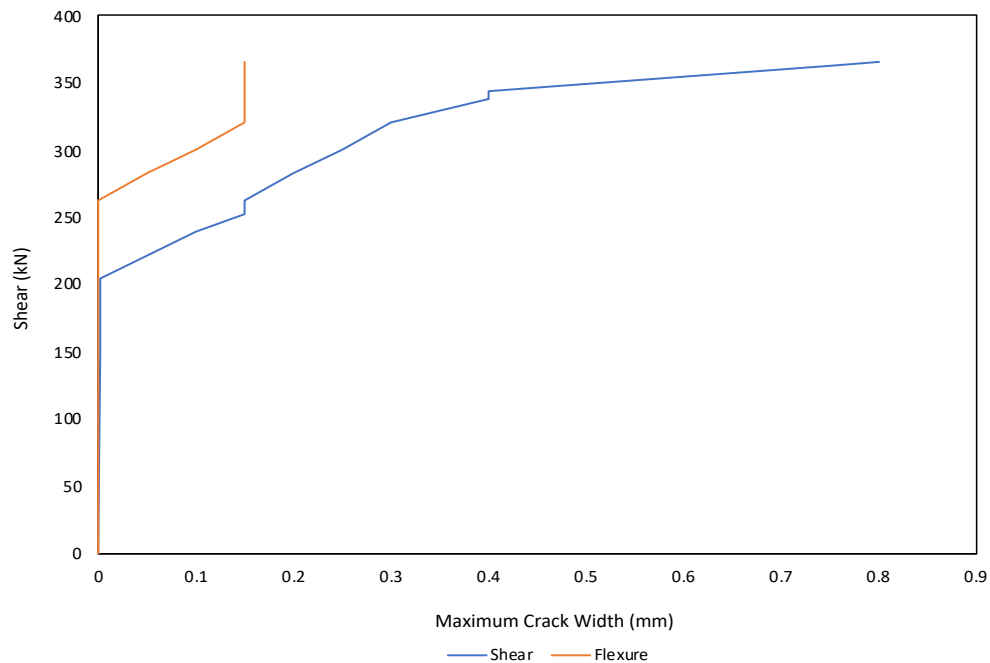


Figure 4.18: Shear versus maximum crack widths for west side of specimen M2

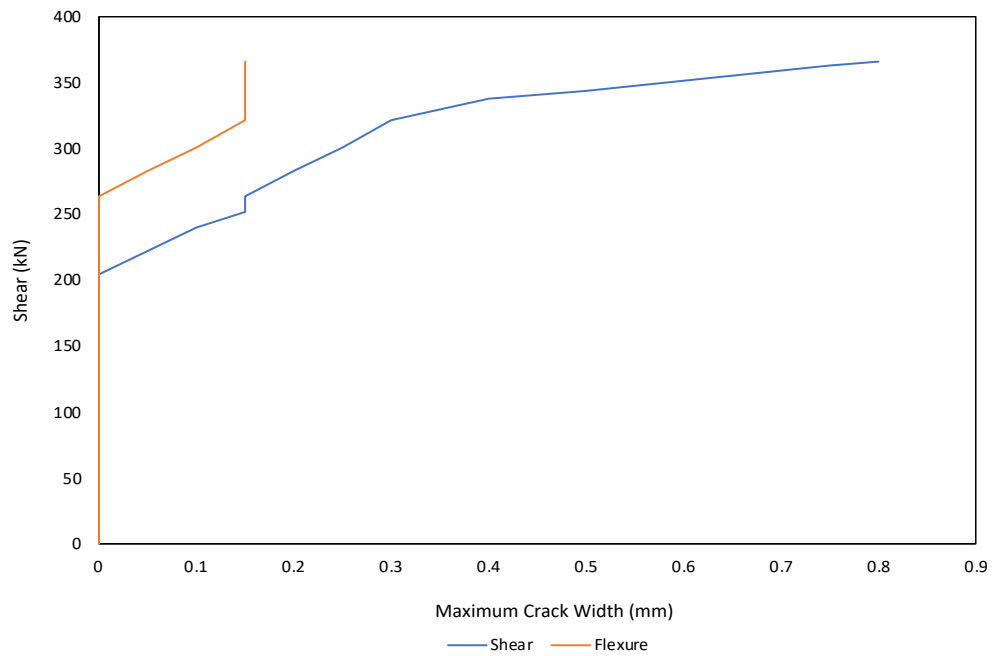


Figure 4.19: Shear versus maximum crack widths for east side of specimen M2

Figures 4.20 and 4.21 show the first shear cracking at 226 kN and at the shear level of 363 kN right before failure, respectively.



Figure 4.20: Crack pattern and widths at a shear of 226 kN for specimen M2

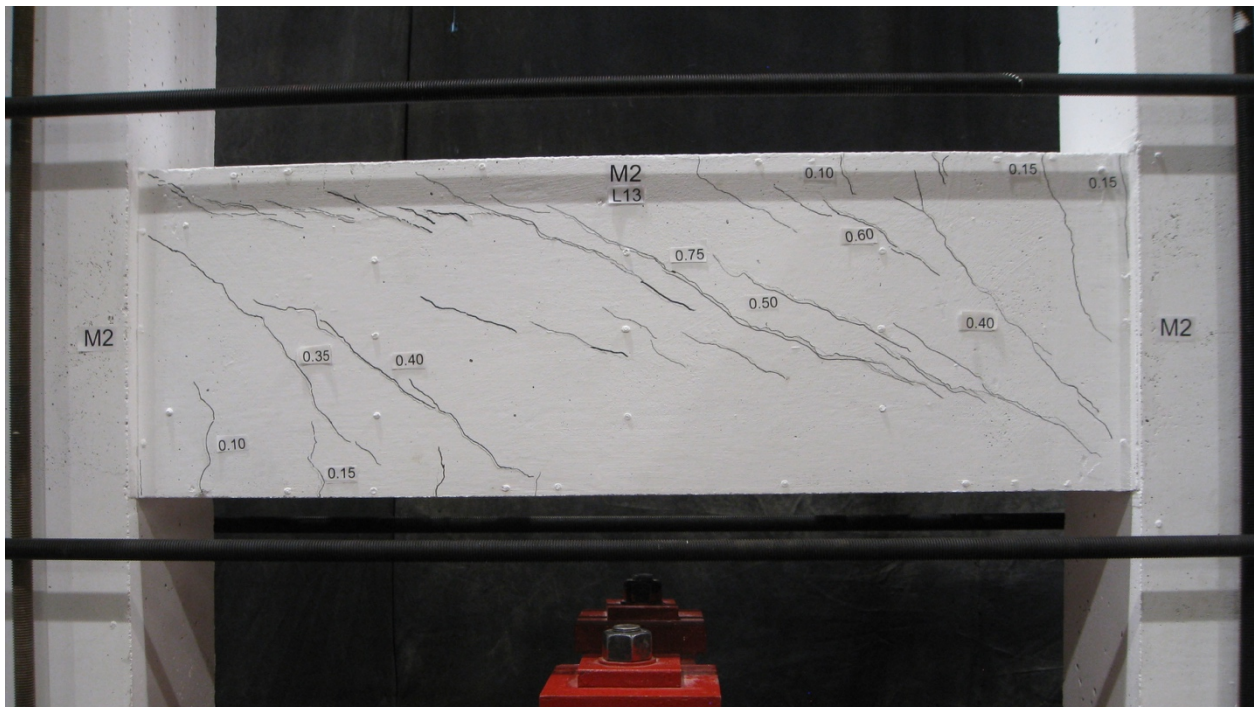


Figure 4.21: Crack pattern and widths at a shear of 363 kN for specimen M2

4.3.4 Measured Strains

The shear versus strain relationships for the No. 3 hoops are shown in Fig. 4.22. Strain gauge, SG6, was located on the hoop 275 mm from the west end of the column. SG6, was the first to reach the yield strain of 0.0016 of the No. 3 bars. This first yielding occurred at a shear of 321 kN during load stage 10. It was observed, at this load level, that the maximum shear crack width was 0.3 mm on the west end. After this load stage, the load dropped slightly and upon reloading strain gauges, SG1, SG2 and SG3, on the east end yielded at a shear of 319 kN during load stage 11. The maximum shear crack width on the east end was 0.4 at this load level. Strain gauge, SG2, malfunctioned shortly after. On the west side strain gauge, SG4, yielded at a shear of 319 kN followed by strain gauge, SG5, at a shear of 347 kN. Thus, all monitored transverse hoops have yielded, before the peak shear was reached. Strain gauge, SG4, was showing high strains and malfunctioned immediately after the maximum shear was recorded. All remaining 5 strain gauges were reading strains well beyond yield at this point.

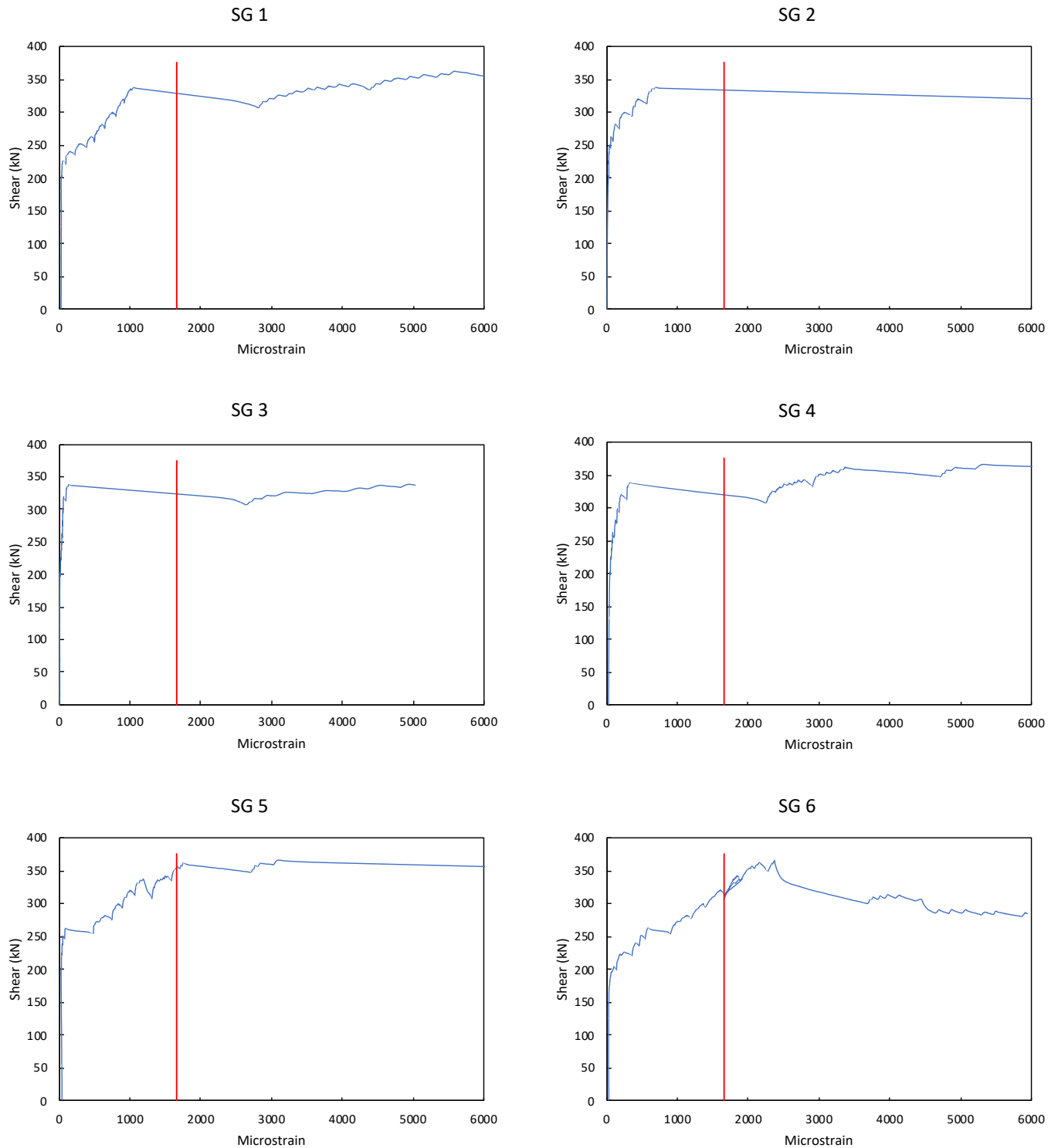


Figure 4.22: Shear versus strain for transverse hoops in specimen M2

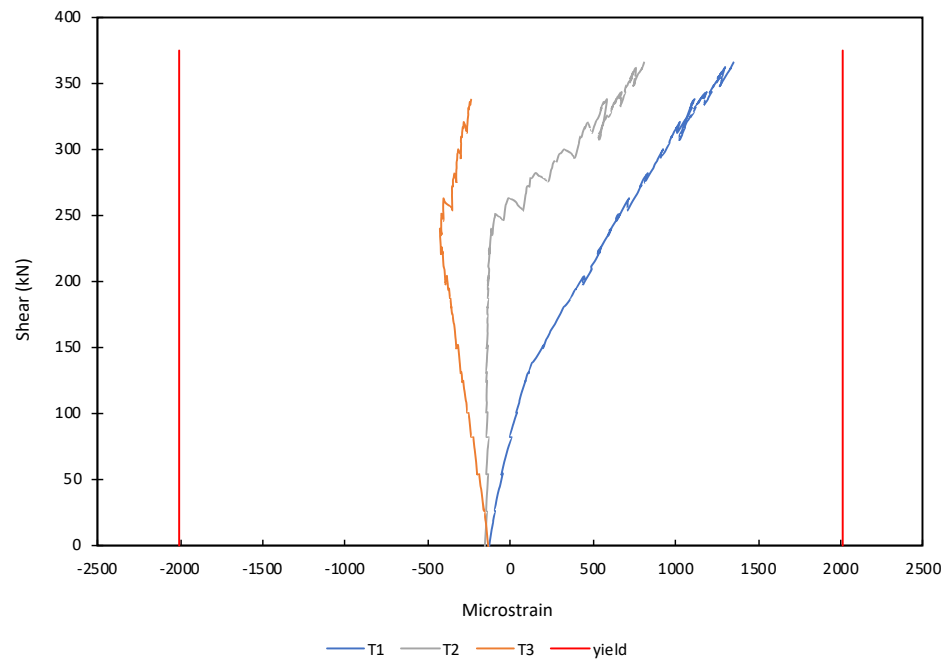


Figure 4.23: Shear versus strain for top longitudinal bar in specimen M2

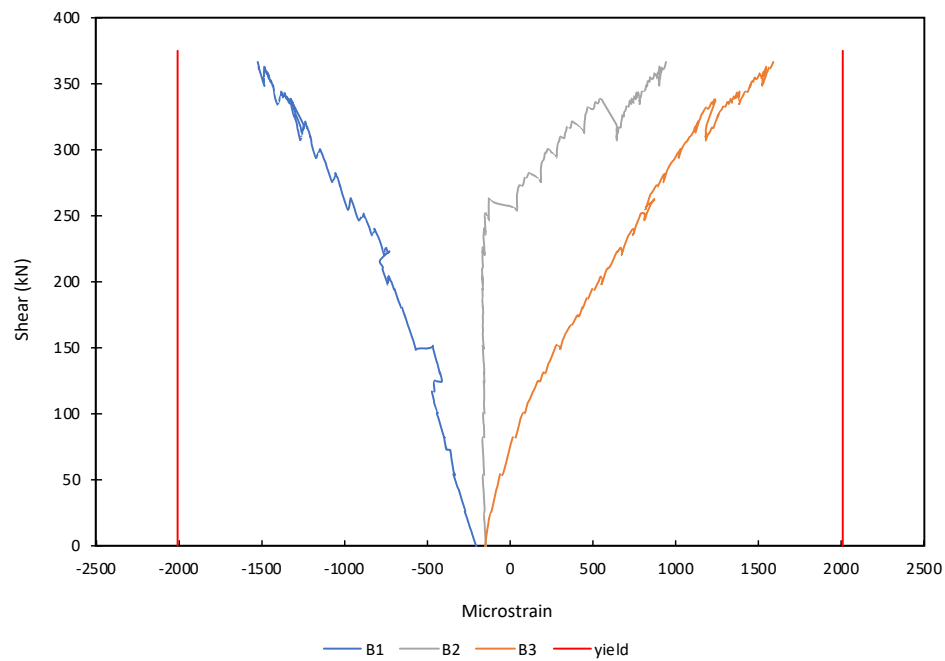


Figure 4.24: Shear versus strain for bottom longitudinal bar in specimen M2

Strain gauges were placed at three different locations on one 25M top bar and on one 25M bottom bar (see Fig. 3.26). Figures 4.23 and 4.24 show the shear versus strain relationships for these strain gauges. All strains started with a negative strain as the column was under axial compression only. When shear was applied on the column, top east strain gauge, T1, experienced tensile strains at a shear of 90 kN. Bottom east gauge, B1, experienced increasing compressive strains due to the moment. Similarly, bottom west gauge, B3, experienced tensile strains at a shear of 80 kN and top east gauge, T3, experienced compressive strains. Central strain gauges, T2 and B2, stayed in compression up to a shear of 260 kN before they experienced tensile strains. None of the strain gauges reached the yield strain of the 25M bars of 0.0021.

The average bar elongations were measured by four LVDTs to obtain the average strains in the bars. The average strain was determined over a gauge length of 250 mm. Initially under the axial load only, all of the average strains were negative, indicating compressive strains. The highest average strain at failure was 0.00169 in tension on the top east LVDT. All other LVDTs were below the yield strain of 0.0021 of the 25M bars at the peak shear. Figure 4.25 shows the shear versus average strain relationships for each LVDT.

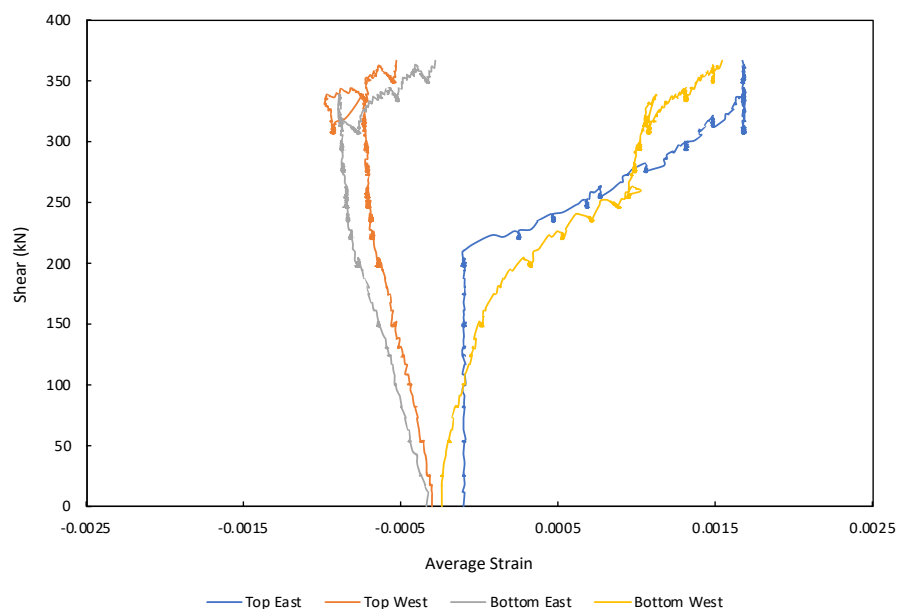


Figure 4.25: Average bar elongation strains for specimen M2

Figure 4.26 shows the results from the LVDTs, placed to form a rosette. M2 had two rosette sets, one on the west end and one on the east (see Fig. 3.24). The horizontal strain, ϵ_x , at mid depth started negative under axial compression and increased to a tensile strain of 0.0004573 and 0.0004915 on the west and east rosettes, respectively. The vertical strain, ϵ_y , remained negligible up to a shear of 225 kN. Coinciding with the formation of the first shear crack. The vertical strain started increasing, at around 260 kN on the west side and 330 kN on the east, due to higher tensile strains. The vertical strain reached a maximum of 0.00207 and 0.00289 on the west and east sides respectively, at the peak shear level. In agreement with the yielding of all transverse hoops. The yield for No. 3 bars is 0.0016. The principal tensile strain, ϵ_1 , at failure was 0.363% on the west side and 0.619% on the east side. Shear strain, γ_{xy} , at failure was 0.446% on the west side and 0.868% on the east side. The principal angle, θ_p , during failure was 32.2° on the west side and 32.4° on the east side. It was noted that the angle of the critical shear crack near the rosette at failure was 35.1° on the west side and 37.3° on the east side.

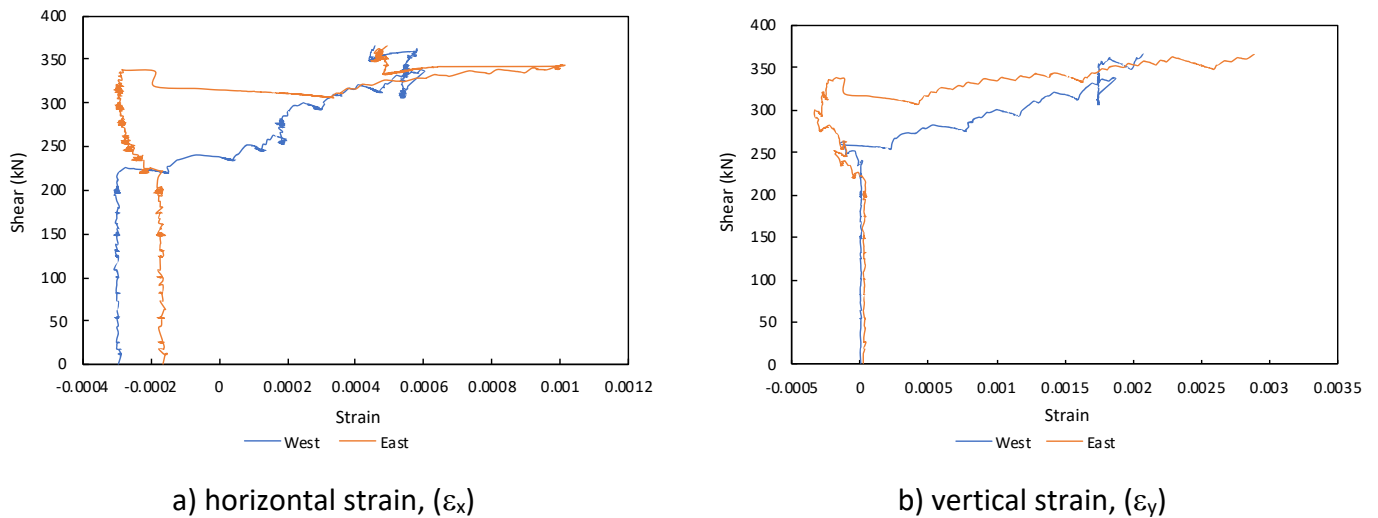
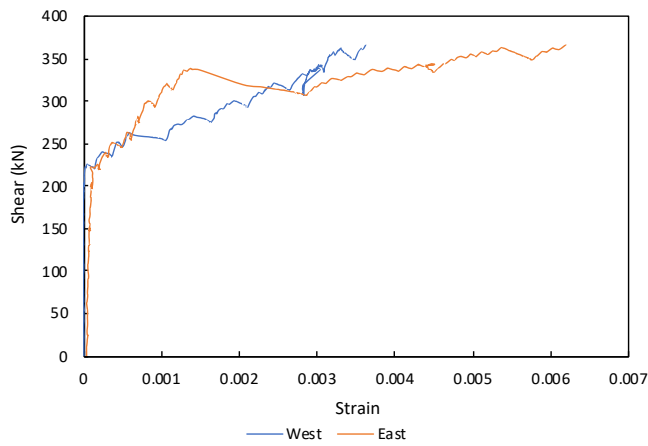
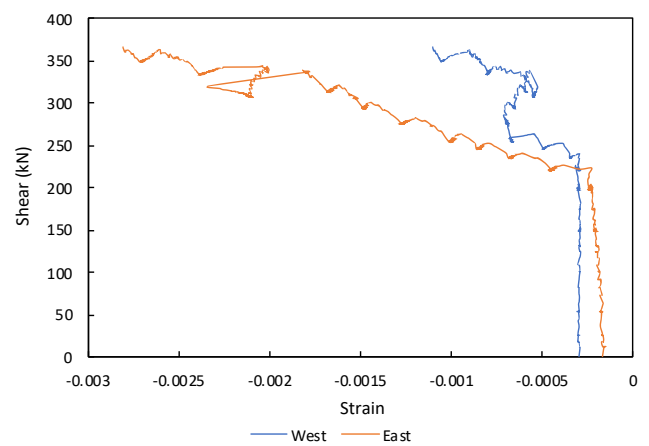


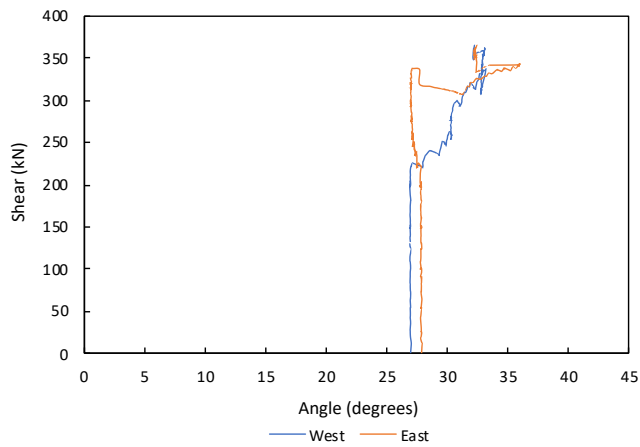
Figure 4.26: Principal strain and angle from specimen M2 rosettes



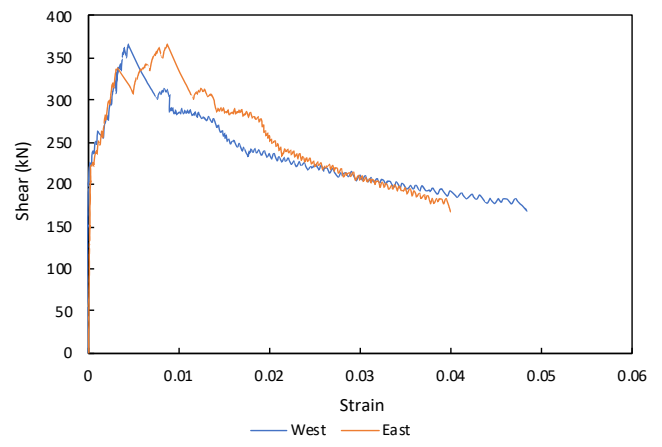
c) principal tensile strain, (ϵ_1)



d) principal compressive strain, (ϵ_2)



e) principal angle, (θ_p)



f) shear strain, (γ_{xy})

Figure 4.26 cont.: Principal strain and angle from specimen M2 rosettes

4.4 Response of Specimen M3

4.4.1 Shear-Deflection Response

The shear versus deflection response is given in Table 4.3 along with the measured maximum crack width at each load stage.

Table 4.3: Shear-deflection response of specimen M3

Load Stage	Description	Applied Shear (kN)	Deflection (mm)	Axial Load (kN)
L0	Balance self-weight	0	0	0
L1	Add axial load	0	0	500
L2	First flexural cracking	123	1.34	
L3	Hairline flexural cracks	153	1.72	
L4	More hairline cracks	225	3.27	
L5	First shear crack	242	3.80	
L6	Shear crack 0.15 mm	270	4.80	
L7	Shear crack 0.2 mm	291	6.06	
L8	First transverse hoop yielding	308	7.35	
L9	Shear crack 0.25 mm	325	8.40	
L10	Shear crack 0.25 mm	345	9.64	
L11	Shear crack 0.3 mm	367	10.93	
L12	Shear crack 0.5 mm	384	12.90	
L13	Peak Load	388	14.1	
L14	1.3 Δ_{peak}	340	17.80	
L15	1.8 Δ_{peak}	305	25.30	
L16	2.8 Δ_{peak}	248	40.10	
L17	5.7 Δ_{peak}	194	80.45	

The shear force versus deflection response is shown in Fig. 4.27. First flexural cracking of the specimen occurred during load stage 2 at a load of 123 kN and a deflection of 1.34 mm. The second hairline crack initiated at the top right corner of the column during load stage 4, at a load of 225 kN and a deflection of 3.27 mm. The second and third hairline crack initiated at the bottom left corner at the same load level. The column reached a maximum shear of 388 kN and a deflection of 14.7 mm followed by a sudden drop in shear, indicating a shear failure. The column was loaded further, in deflection control, up to a deflection of 80.45 mm which was 5.7 times the deflection at the peak. At this load stage the shear was 194 kN, which was 50% of the peak shear after which the test was stopped. The specimen was capable of resisting load up to this stage due to the deflection control that was imposed.

The compressive axial load was applied and maintained at 500 kN, the axial load versus applied shear is shown in Fig. 4.28.

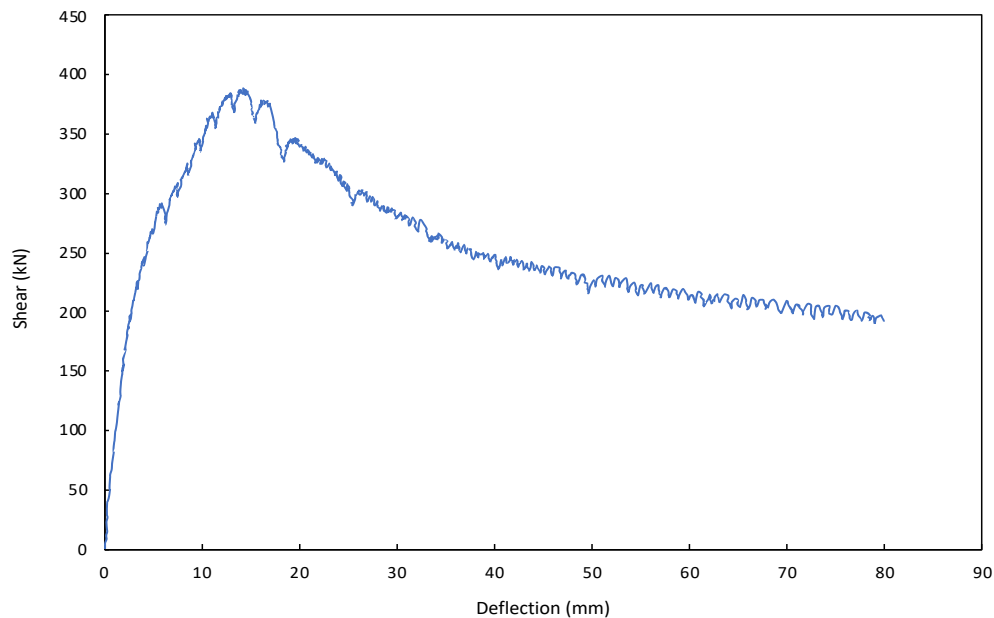


Figure 4.27: Shear versus deflection of specimen M3

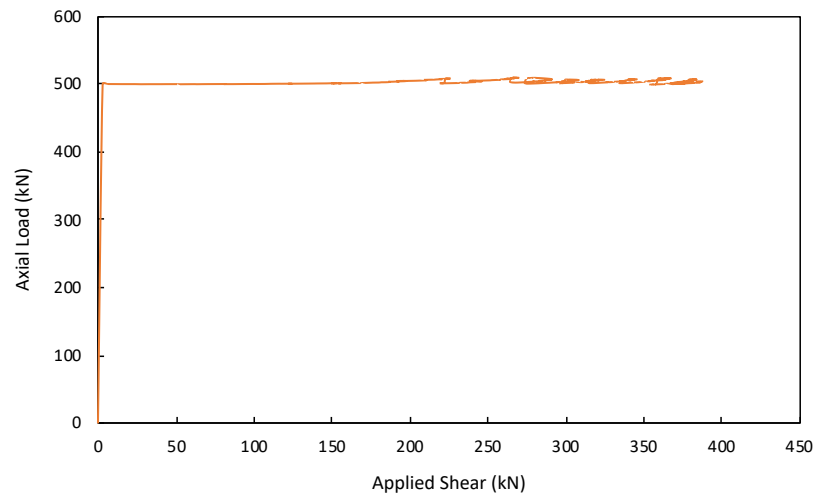


Figure 4.28: Applied load versus applied shear for specimen M3

4.4.2 Shear Failure

The shear failure can be seen in Fig. 4.29. The 1.0 mm wide critical shear crack started from the top west corner of the column and extended 500 mm towards the centerline. Another 0.6 mm wide critical crack was extending 400 mm towards the centerline, from the bottom east corner. A central 1.0 mm wide crack started approximately 300 mm from the west side and extended 200 mm from the centerline. The fourth transverse hoop on the east side located 350 mm from the face of the column, experienced significant yielding before shear failure occurred. The specimen was loaded further after the shear failure, up to a displacement of 80.45 mm. At this stage, the load had dropped to 50% of the peak shear level and the test was stopped. The specimen in the final displaced position is shown in Fig. 4.30.

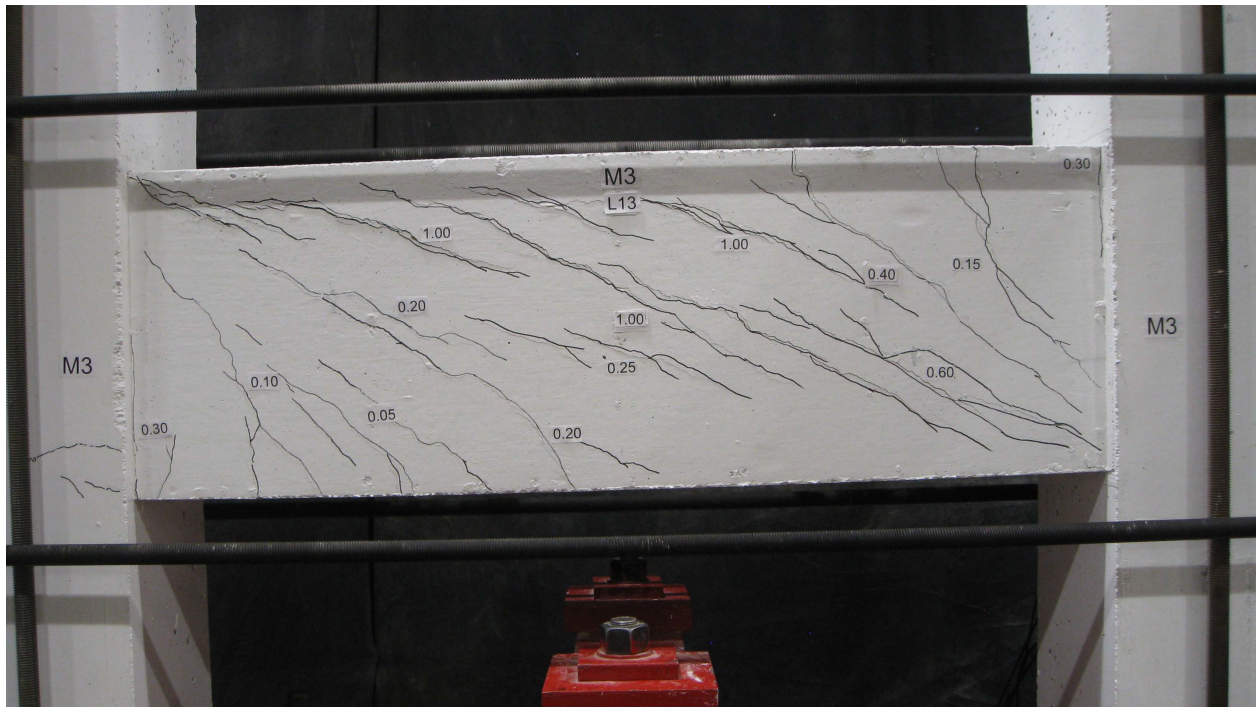


Figure 4.29: Shear failure of specimen M3



Figure 4.30: Specimen M3 in final displaced position

4.4.3 Crack Widths

The first shear cracks occurred at a load of 242 kN and a deflection of 3.80 mm. Two shear cracks located in the critical shear region on the east side formed at this load level. Similarly, one shear crack was formed on the west side. Strain gauges, SG1 and SG6, located 150 mm from the face of the column on the east and west side respectively, were experiencing strains approximately 35% of the yield of the No. 3 transverse hoops. Coinciding with the location of the initial shear cracks. None of the other hoops had picked up considerable strain at this point. The existing cracks extended and widened, during the subsequent load stages. The shear versus maximum crack widths for the east and west sides are shown in Fig. 4.31 and Fig. 4.32, respectively. At shears between 360 and 380 kN, maximum crack widths of 0.5 mm and 0.6 mm were observed on the west and east side, respectively. Before shear failure, a maximum flexural crack width of 0.25 mm was observed on the west side and east side. Shear cracks were consistently close in value between the west and east sides of the column. A critical 0.8 mm wide shear crack opened up when maximum shear was reached. The critical crack continued to grow to 1.2 mm after the column was pushed further in displacement control.

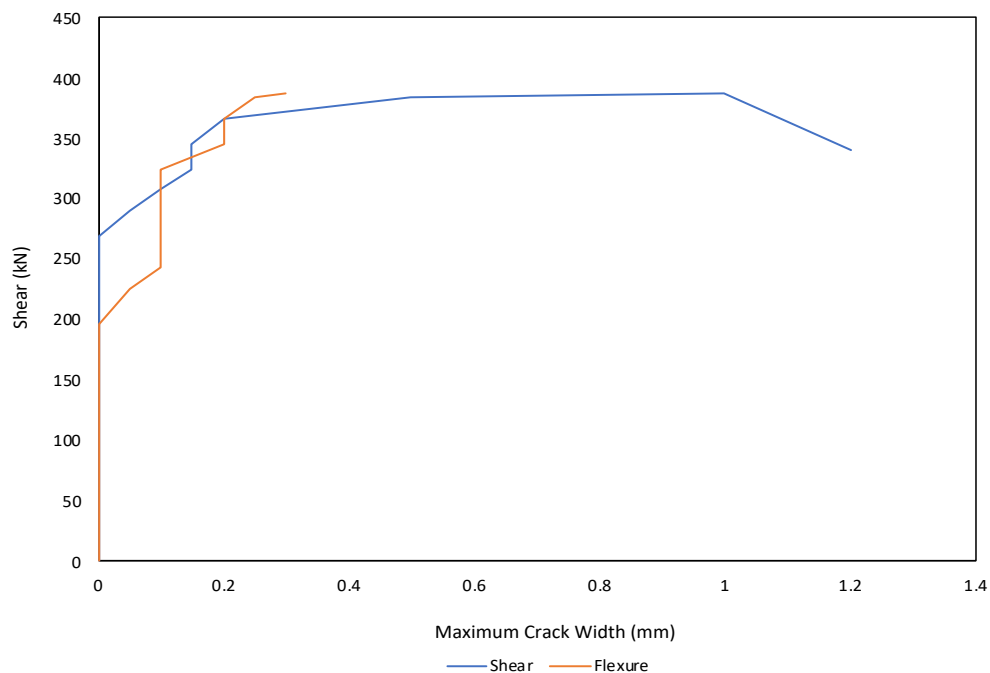


Figure 4.31: Shear versus maximum crack widths for west side of specimen M3

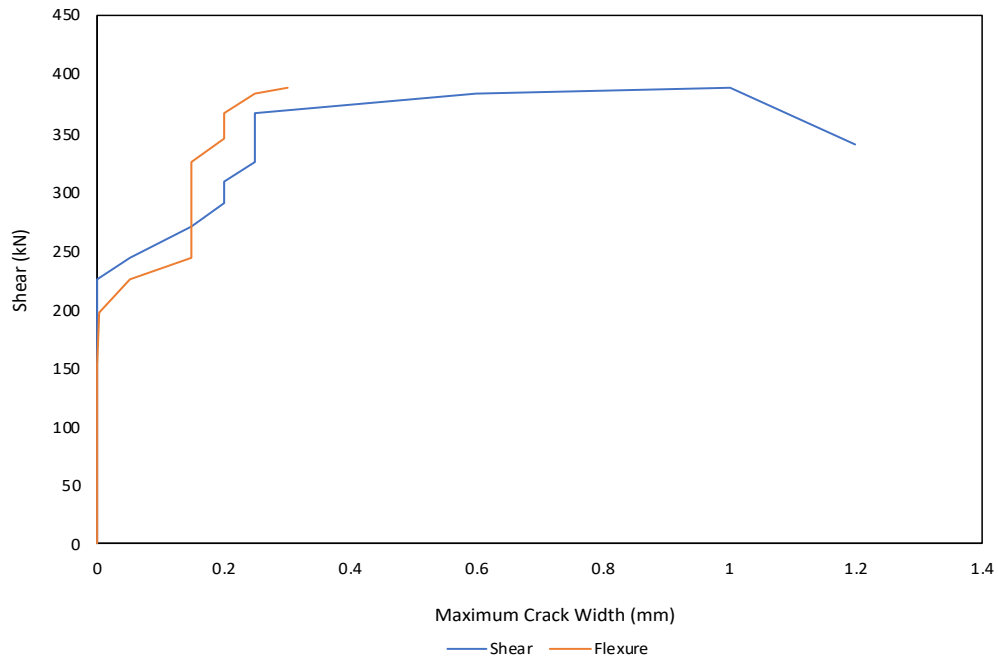


Figure 4.32: Shear versus maximum crack widths for east side of specimen M3

Figures 4.33 and 4.34 show the first shear cracking at 242 kN and at the shear level of 384 kN right before failure, respectively.



Figure 4.33: Crack pattern and widths at a shear of 242 kN for specimen M3

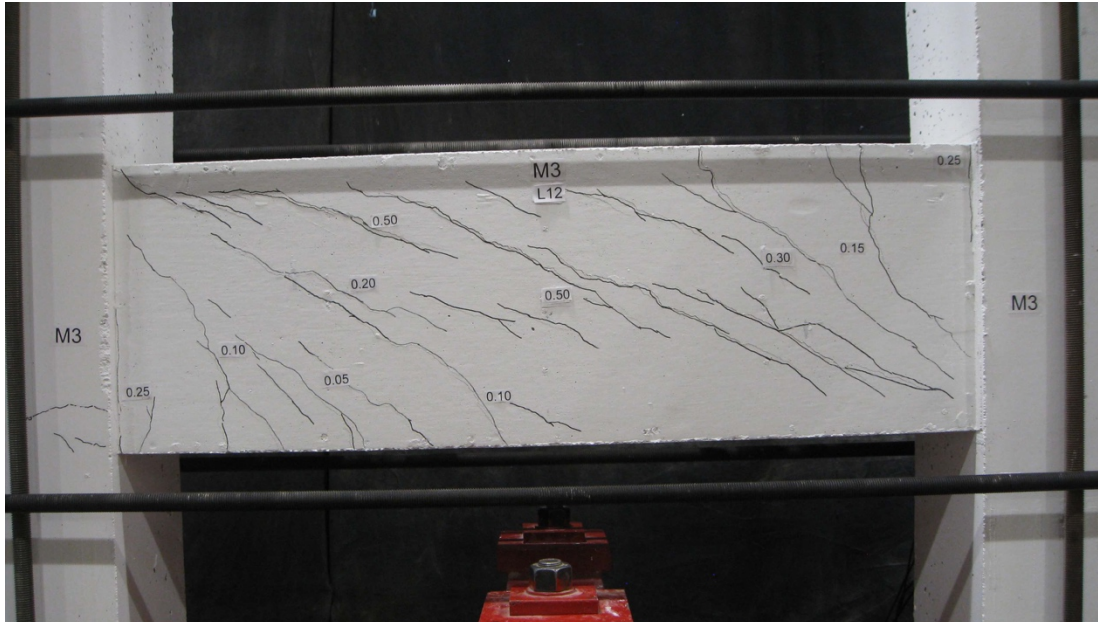


Figure 4.34: Crack pattern and width at a shear of 384 kN for specimen M3

4.4.4 Measured Strains

The shear versus strain relationships for the No. 3 hoops are shown in Fig. 4.35. Strain gauge, SG3, located on the hoop 50 mm away from the centerline of the column, was the first to yield. This first yielding of the transverse reinforcement occurred at a shear of 290 kN. It was noted that, at this shear level, the maximum shear crack width was 0.2 mm on the east end. On the east side strain gauges, SG1 and SG2, reached yielding at a shear of 337 kN and 326 kN, respectively. Thus, significant yielding had occurred on the east side before the peak shear was reached. On the west end strain gauge, SG4, yielded at a shear of 335 kN. Strain gauge, SG6, only reached a strain of 0.00126 at the peak shear level. Strain gauge, SG5, was malfunctioning thus no strain was recorded. After shear failure, strain gauge, SG6, yielded at a shear of 285 kN, when the critical shear crack had widened. As the column was pushed further in displacement control, strain gauge, SG3, was showing high strains and malfunctioned at a shear of 357 kN.

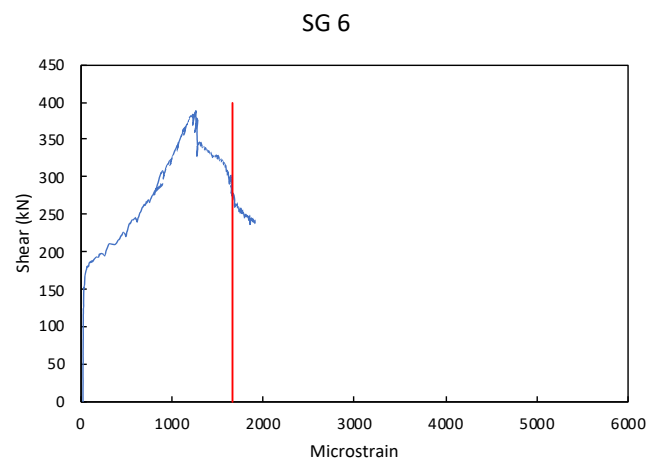
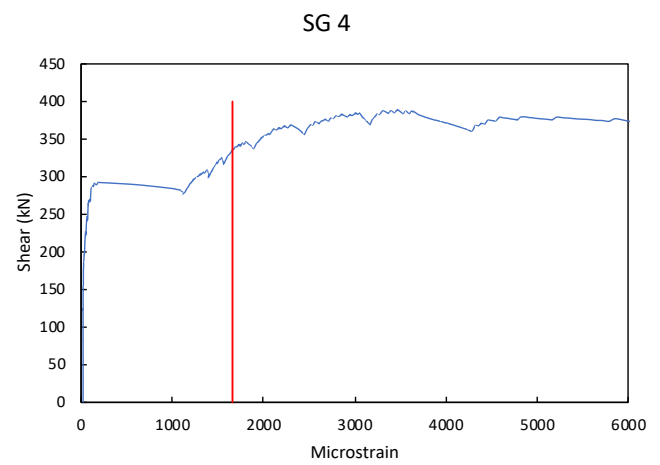
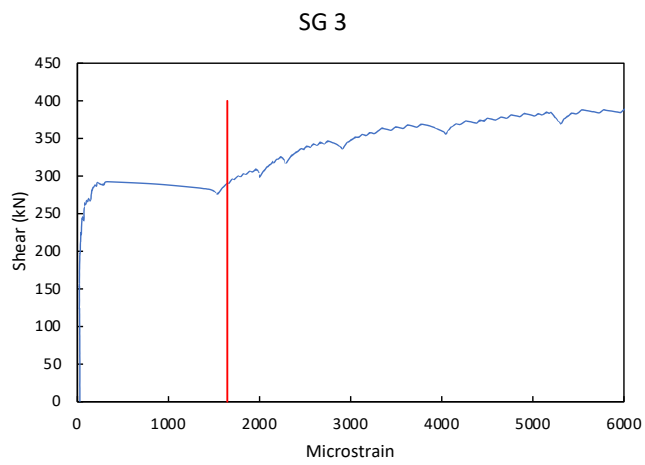
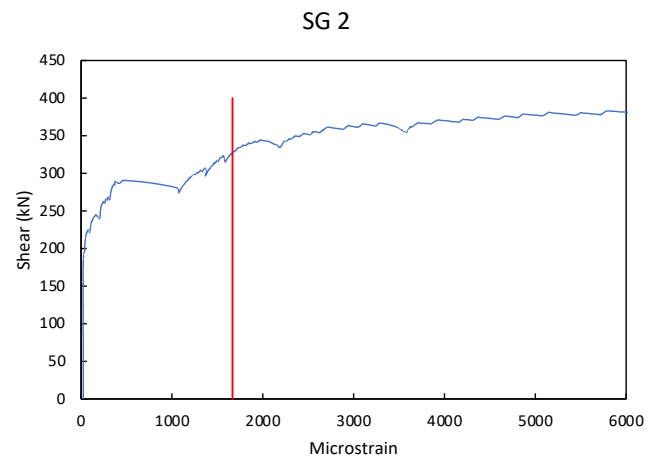
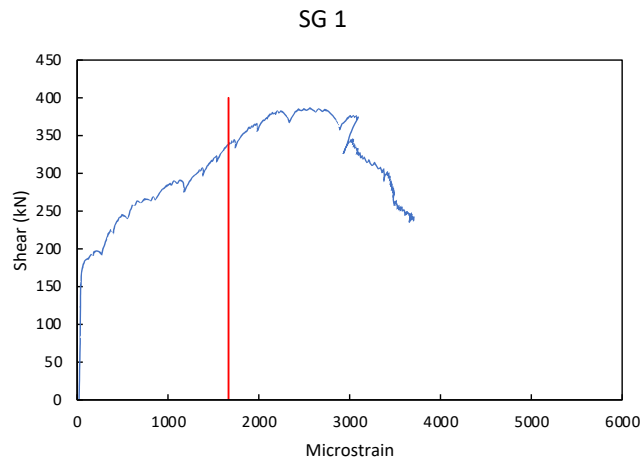


Figure 4.35: Shear versus strain for transverse hoops in specimen M3

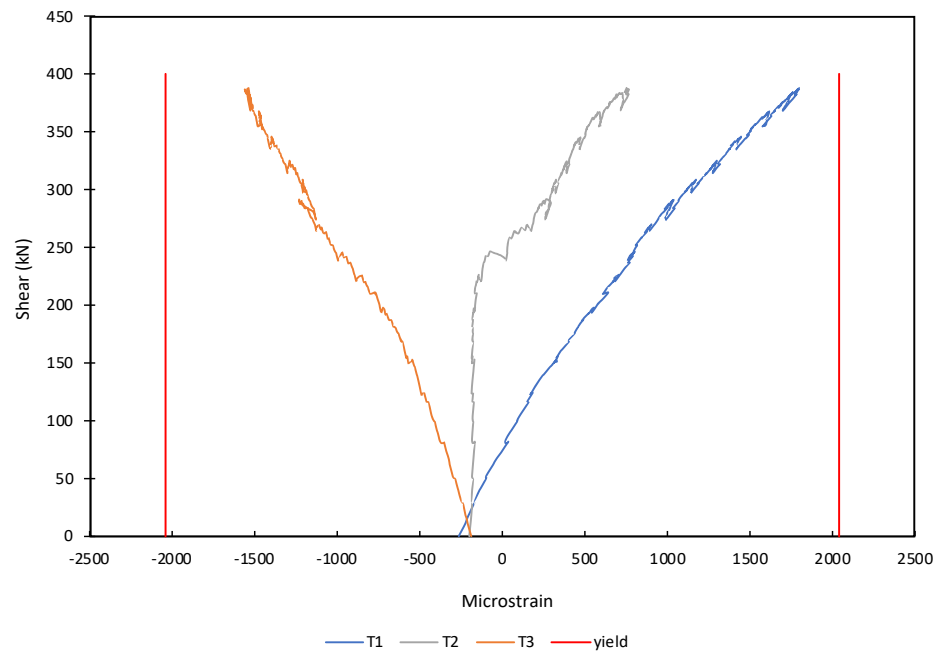


Figure 4.36: Shear versus strain for top longitudinal bar in specimen M3

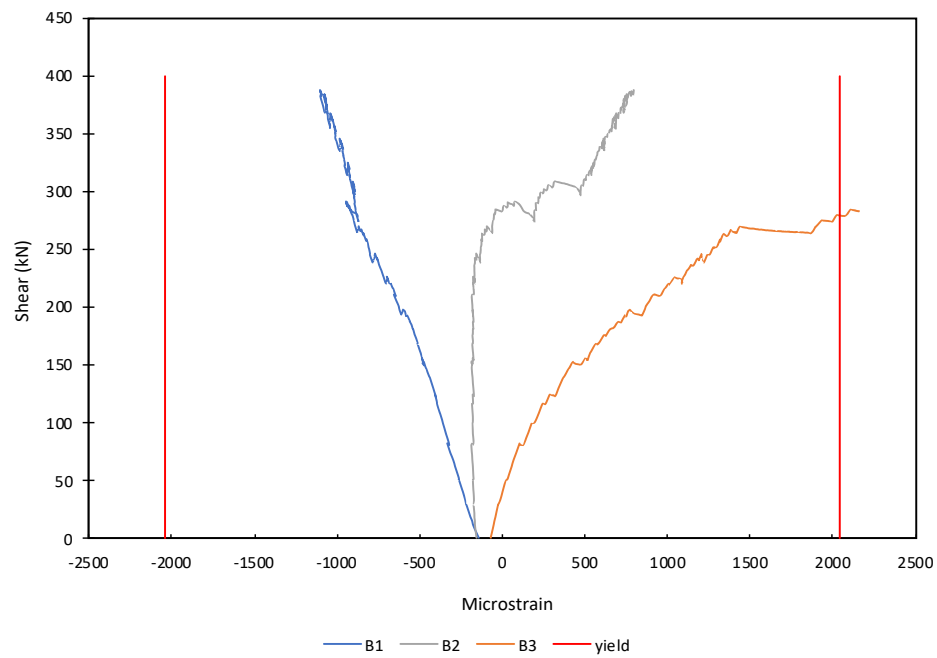


Figure 4.37: Shear versus strain for bottom longitudinal bar in specimen M3

Strain gauges were placed at three different locations on one 25M top bar and on one 25M bottom bar (see Fig. 3.27). Figures 4.36 and 4.37 show the shear versus strain relationships for these strain gauges. All strain gauges started with negative strains indicating compressive strains, as the column was under axial compression only. When the column was loaded in shear, the top east strain gauge, T1, experienced tensile strains at a shear of 80 kN. On the other hand, bottom east gauge, B1, experienced increasing compressive strains due to the moment. Similarly, bottom west gauge, B3, started experiencing tensile strains at a shear of 40 kN. Conversely, top east gauge, T3, experienced compressive strains. Central strain gauges, T2 and B2, stayed in compression up to a shear of 242 and 282 kN respectively, before they started seeing tensile strains. None of the strain gauges on the longitudinal 25M bars reached the yield strain of 0.0021 except for strain gauge, B3. Strain gauge, B3, yielded at a shear of 279 kN.

The bar elongations were measured by four LVDTs in order to obtain the average strains in the bars. The average strain was determined over a gauge length of 250 mm. All of the average strains, started negative, indicating compressive strains. All LVDTs were below the yield strain of 0.0021 for the 25M bars at the peak shear. Figure 4.38 shows the shear versus average strain relationships for each LVDT.

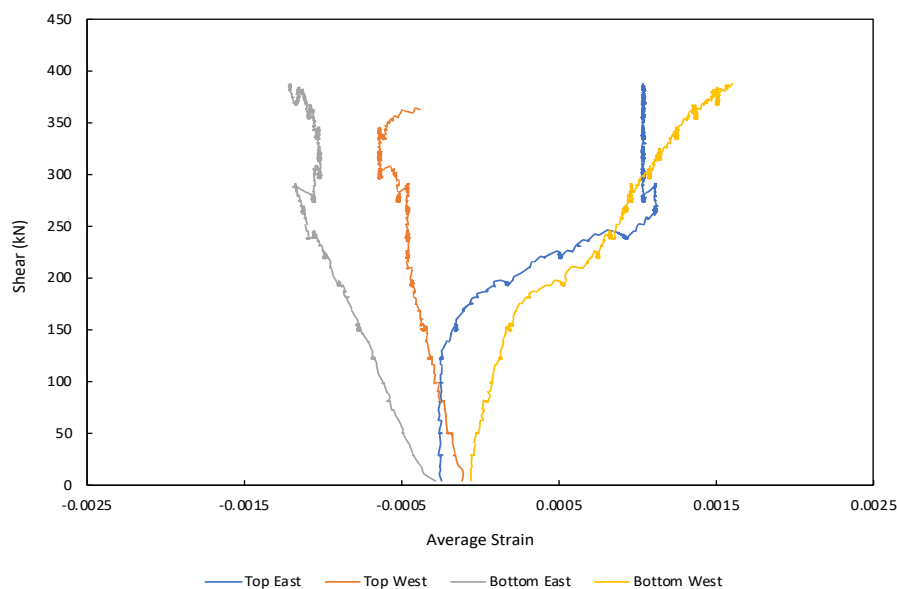


Figure 4.38: Average bar elongation strains for specimen M3

Figure 4.39 shows the results from the LVDTs, placed to form a rosette. M3 had two rosette sets, one on the west end and one on the east end (see Fig. 3.24). The horizontal strain, ϵ_x , at mid depth started negative under axial compression only. At a shear between 300 and 320 kN, ϵ_x , started growing considerably. At failure, the horizontal strain was 0.0005535 in tension on the west end and 0.0007235 in compression on the east end. The vertical strain, ϵ_y , remained negligible up to a shear of 242 kN when it started to increase, coinciding with the formation of the first shear crack during load stage 5. At a shear of 269 kN on the west end and 252 kN on east side, the vertical strain started increasing rapidly. The vertical strain reached a maximum of 0.00425 and 0.00553 on the west and east ends, respectively, when the specimen failed in shear. Both strains were higher than the yield strain of 0.0016 of the No. 3 transverse hoops. The strain gauges located on the hoops close to the location of the vertical LVDTs, were yielding at failure. The principal tensile strain, ϵ_1 , at failure was 0.551% on the west end and 0.727% on the east end. Shear strain, γ_{xy} , at failure was 0.450% on the west side and 0.745% on the east side. The principal angle, θ_p , at failure was 32.7° on the west end and 23.9° on the east end. It was noted that the angle of the critical shear crack near the rosette at failure was 26.8° on the west side and 25.0° on the east side.

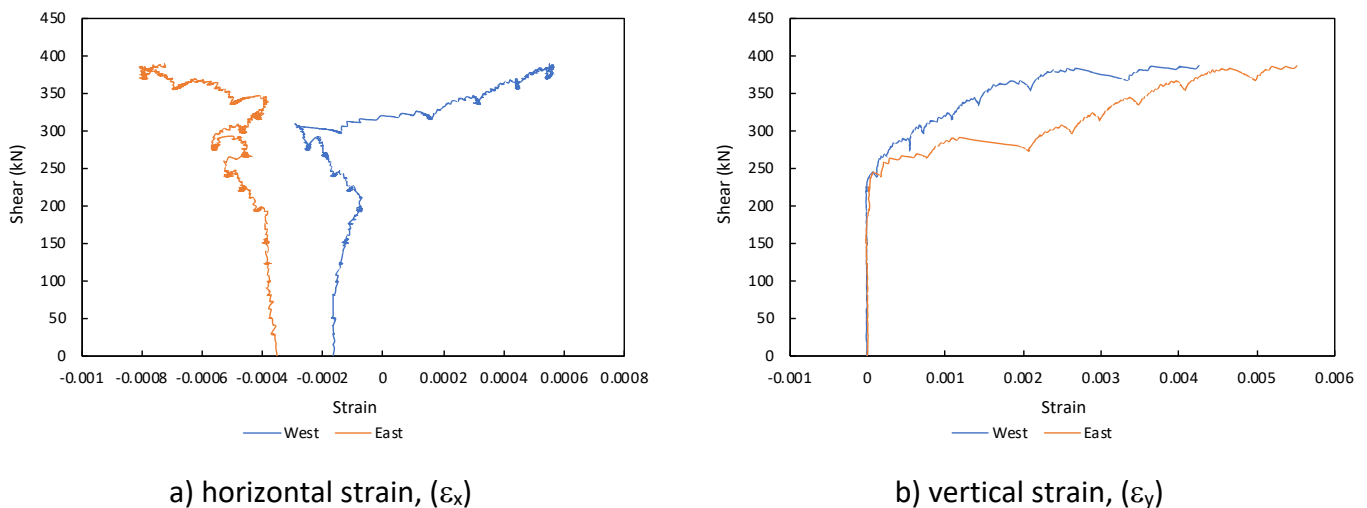
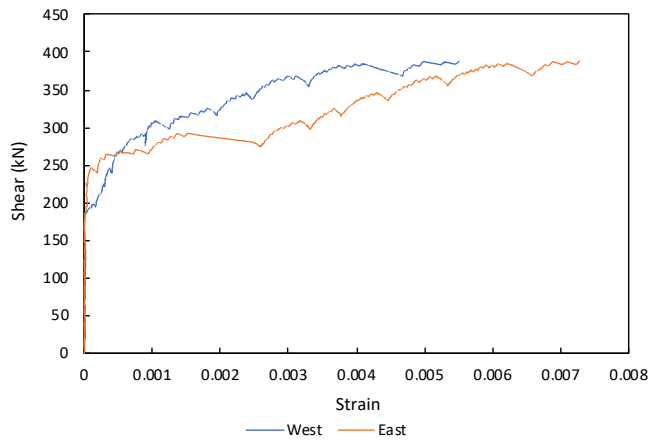
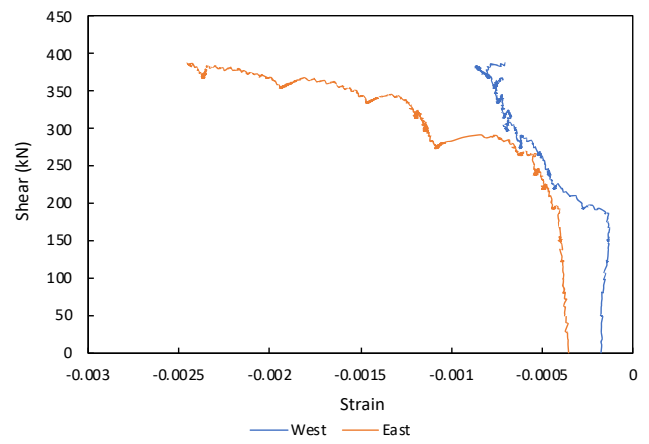


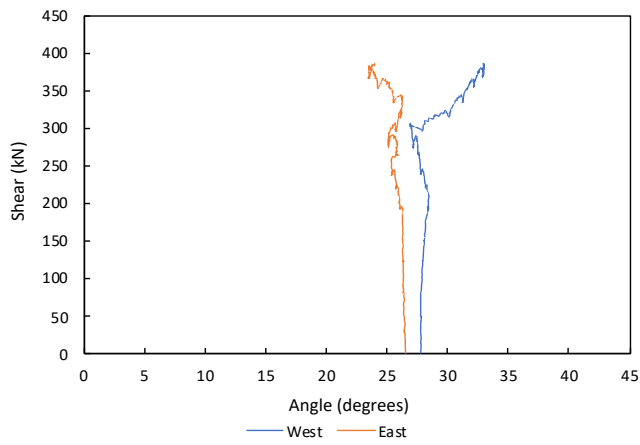
Figure 4.39: Principal strain and angle from specimen M3 rosettes



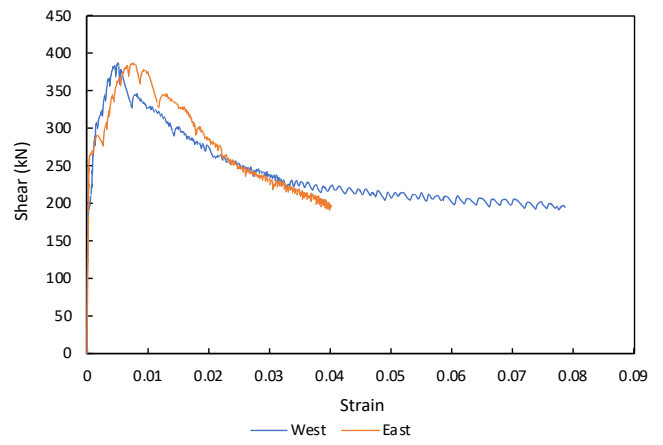
c) principal tensile strain, (ϵ_1)



d) principal compressive strain, (ϵ_2)



e) principal angle, (θ_p)



f) shear strain, (γ_{xy})

Figure 4.39 cont.: Principal strain and angle from specimen M3 rosettes

4.5 Response of Specimen M4

4.5.1 Shear-Deflection Response

The shear versus deflection response is given in Table 4.4 along with the measured maximum crack width at each load stage.

Table 4.4: Shear-deflection response of specimen M4

Load Stage	Description	Applied Shear (kN)	Deflection (mm)	Axial Load (kN)
L0	Balance self-weight	0	0	0
L1	Add axial load	0	0	500
L2	First flexural cracking	150	1.53	
L3	Hairline flexural cracks	200	2.41	
L4	First shear crack	226	3.11	
L5	Shear crack 0.1 mm	252	3.78	
L6	Shear crack 0.15 mm	278	4.82	
L7		300	5.72	
L8	Shear crack 0.2 mm First transverse hoop yielding	321	6.99	
L9	Shear crack 0.25 mm	351	8.40	
L10	Shear crack 0.25 mm	384	10.09	
L11	Shear crack 0.3 mm	417	11.90	
L12	Peak Load Yielding of all transverse reinforcement	459	14.20	
L13	1.2 Δ_{peak}	417	16.99	
L14	1.8 Δ_{peak}	338	26.10	
L15	2.8 Δ_{peak}	275	39.70	
L16	4.7 Δ_{peak}	205	66.31	
L17	5.7 Δ_{peak}	175	80.52	

The shear force versus deflection response is shown in Fig. 4.40. First flexural cracking of the specimen occurred during load stage 2 at a load of 150 kN and a deflection of 1.53 mm. The first signs of hairline inclined cracking were observed at a shear of 226 kN. The column reached a maximum shear of 459 kN and a deflection of 14.20 mm followed by a sudden drop in shear to 432 kN, indicating a shear failure. The column was loaded further, in deflection control, up to a deflection of 80.52 mm which was 5.7 times the deflection at the peak. The column was capable of resisting load due to the deflection control that was imposed. At this stage the shear was 175 kN, that was 38% of the peak shear after which the test was stopped.

The compressive axial load was applied and maintained at 500 kN, the axial load versus applied shear is shown in Fig. 4.41.

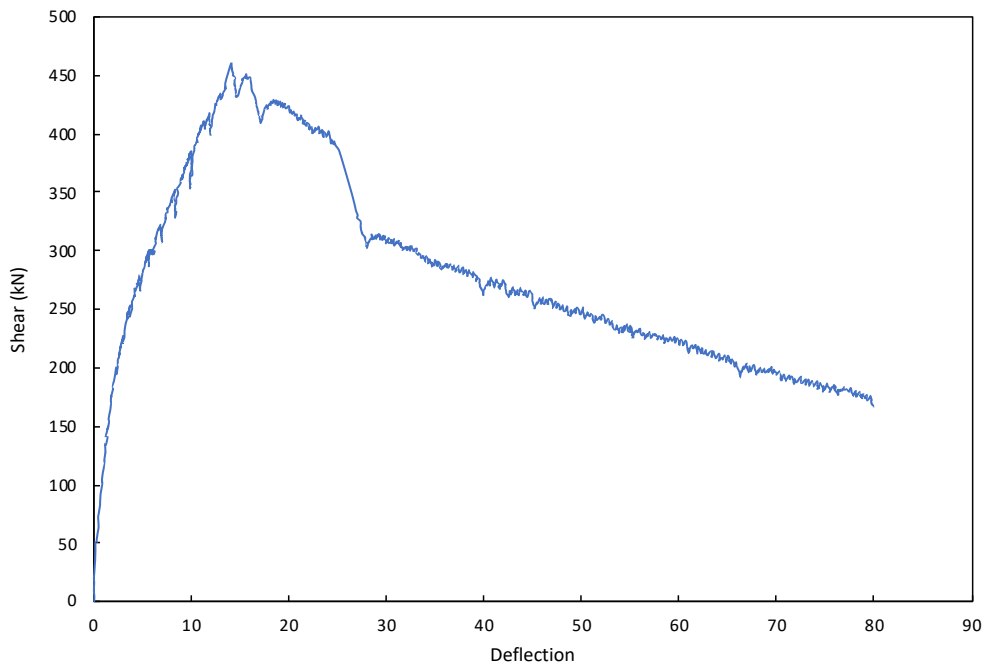


Figure 4.40: Shear versus deflection of specimen M4

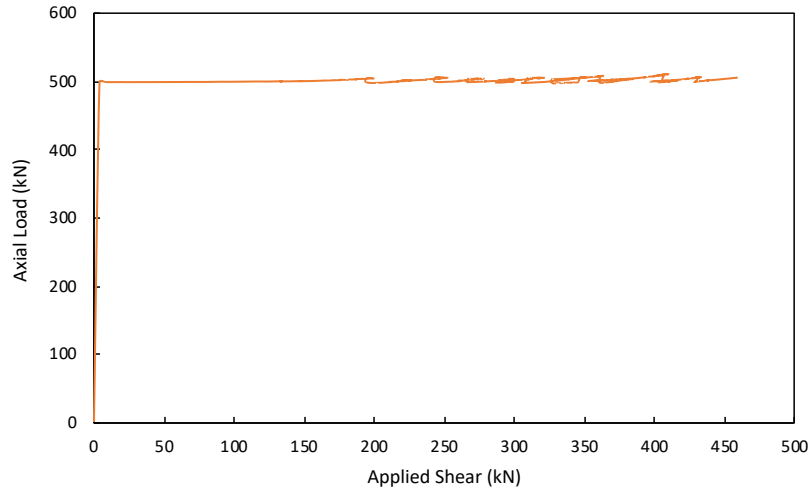


Figure 4.41: Applied load versus applied shear for specimen M4

4.5.2 Shear Failure

The shear failure can be seen in Fig. 4.42. There were two critical shear cracks, one on each end, when maximum shear was reached. The 0.25 mm wide crack on the west end was inclined at 28.6° . The crack extended from the top left corner of the column towards the column's centerline. The 0.35 mm wide crack on the east end was inclined at 27.7° . The crack extended 400 mm from the bottom right corner into the column. All transverse hoops were well beyond yield before shear failure occurred. The specimen was loaded further after the shear failure, up to a displacement of 80.52 mm. At this stage, the load had dropped to 38% of the peak shear level and it was decided to stop the test. The specimen in the final displaced position is shown in Fig. 4.43.

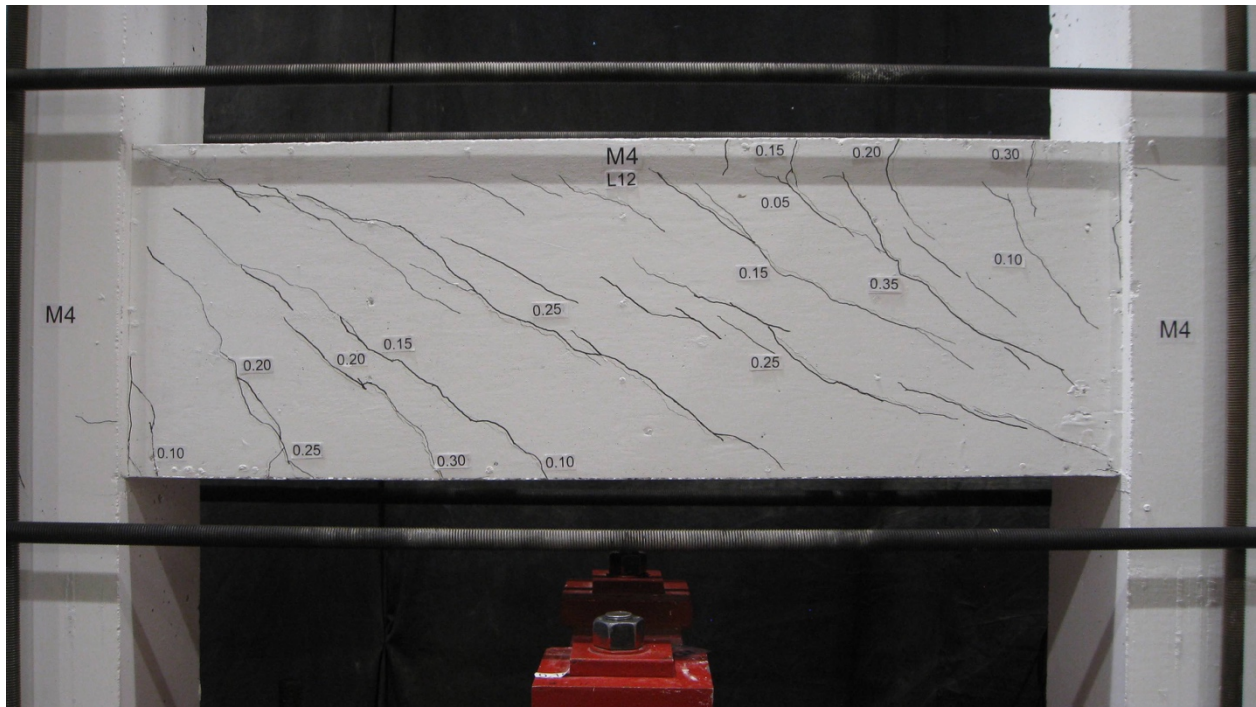


Figure 4.42: Shear failure of specimen M4



Figure 4.43: Specimen M4 in final displaced position

4.5.3 Crack Widths

The first shear cracks occurred at a load of 226 kN and a deflection of 3.11 mm. Two 0.05 mm shear cracks located in the critical shear region on the east side formed at this load level. Similarly, one 0.05 mm shear crack was formed on the west side. Only strain gauge, SG1, located 262.5 mm from the column end on the east side was experiencing a noticeable strain at this load stage. The strain was approximately 15% of the yield strain of the No. 3 hoops. All strain gauges were experiencing negligible strains at this level. In the subsequent load stages, more cracks were observed. The cracks were uniform and controlled. The maximum shear crack width recorded before shear failure was 0.3 mm. The shear versus maximum crack widths for the east and west sides are shown in Fig. 4.44 and Fig. 4.45, respectively. At a shear of 417 kN, maximum crack widths of 0.2 mm and 0.3 mm were observed on the west and east side, respectively. Before shear failure, maximum flexural crack widths of 0.25 mm and 0.3 mm were seen on the west side and east side, respectively. Shear cracks were consistently close in value between the west and east sides of the column. The column was pushed further in displacement control, post shear failure. The maximum shear crack width was 0.35 mm.

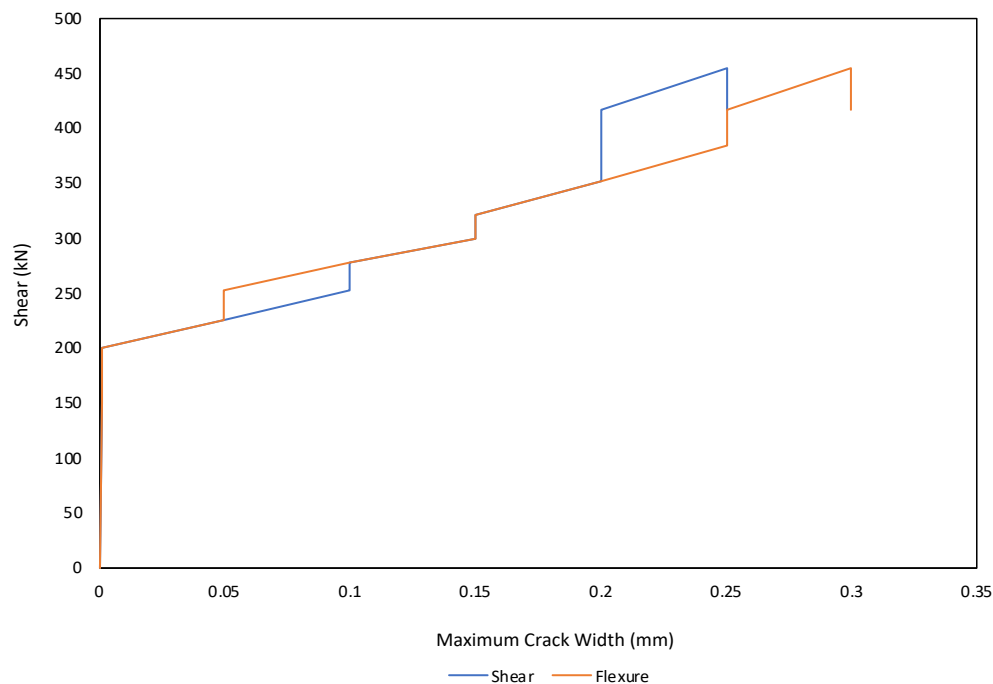


Figure 4.44: Shear versus maximum crack widths for west side of specimen M4

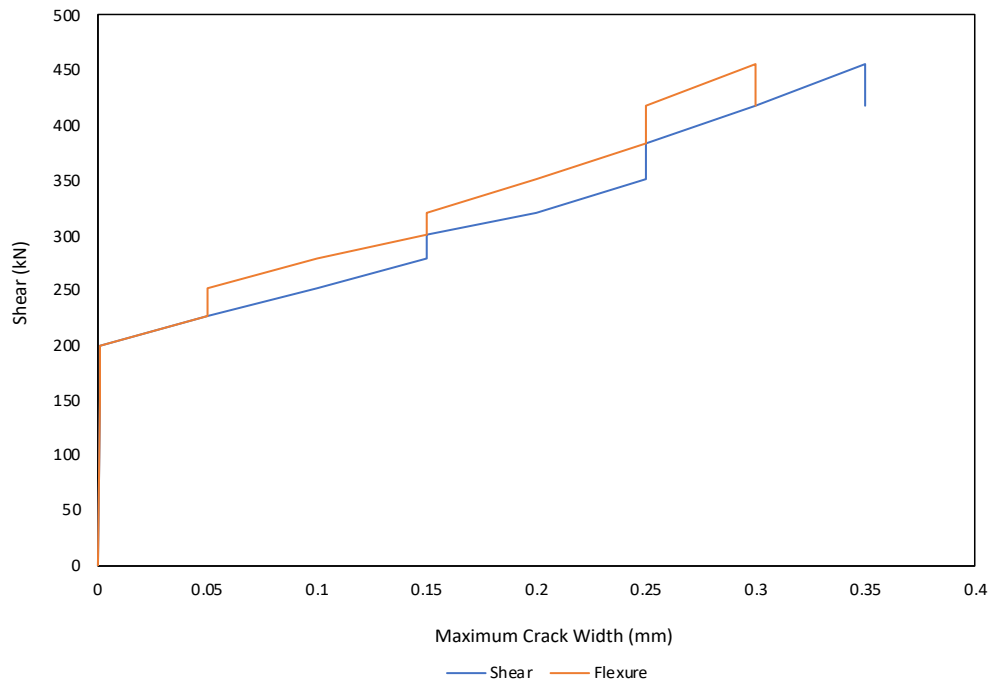


Figure 4.45: Shear versus maximum crack widths for east side of specimen M4

Figures 4.46 and 4.47 show the first shear cracking at 226 kN and at the shear level of 417 kN before shear failure occurred, respectively.



Figure 4.46: Crack pattern and widths at a shear of 226 kN for specimen M4

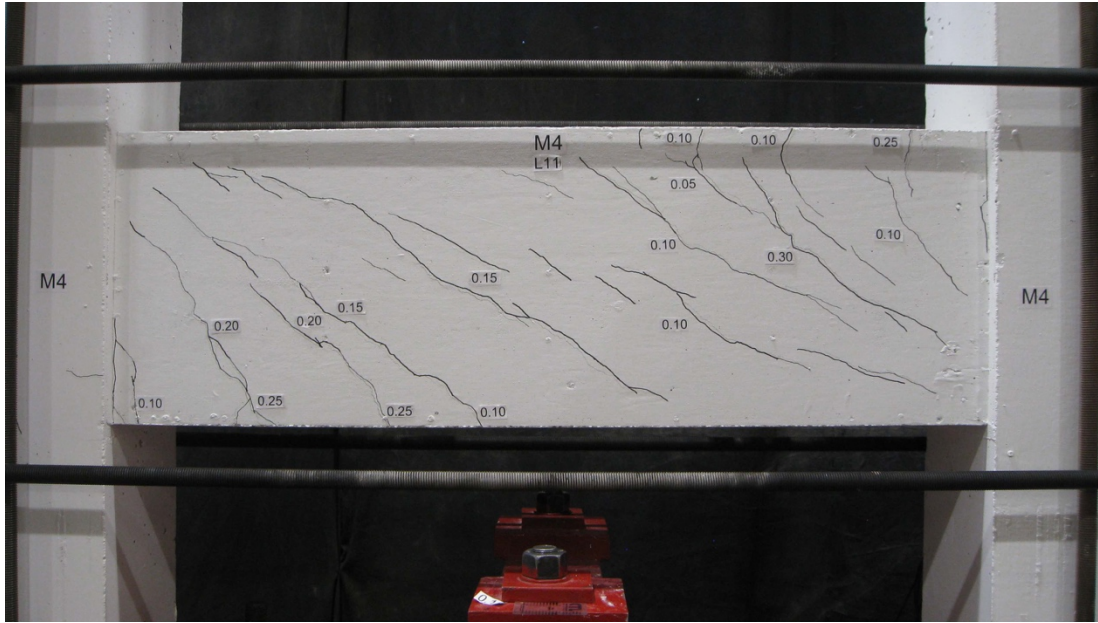


Figure 4.47: Crack pattern and width at shear of 417 kN for specimen M4

4.5.4 Measured Strains

The shear versus strain relationships for the No. 3 hoops are shown in Fig. 4.8. Strain gauge, SG5, located on the hoop 412.5 mm away from the west end of the column, was the first to yield. It was observed that, at this shear level, the shear crack crossing this hoop, had a width of 0.15 mm. This first yielding of the transverse reinforcement occurred at a shear of 327 kN. On the east side strain gauge, SG3, was the first to reach yield at a shear of 406 kN. Strain gauges, SG1 and SG2, reached yielding at a shear of 428 kN and 409 kN, respectively. Significant yielding had occurred on the east side before shear failure. On the west end strain gauge, SG4, yielded at a shear of 382 kN. Strain gauge, SG6, was malfunctioning thus no strain was recorded. All strain gauges reached yield before the shear failure. When maximum shear was recorded, the average strain experienced by all strain gauges was 0.00235, except for strain gauge, SG5. Strain gauge, SG5, was experiencing a strain of 0.00476. Twice the strain on the other four strain gauges. After shear failure, at a shear of 257 kN all strain gauges malfunctioned except strain gauge, SG1. The maximum strain reached by strain gauge, SG1 was 0.00397.

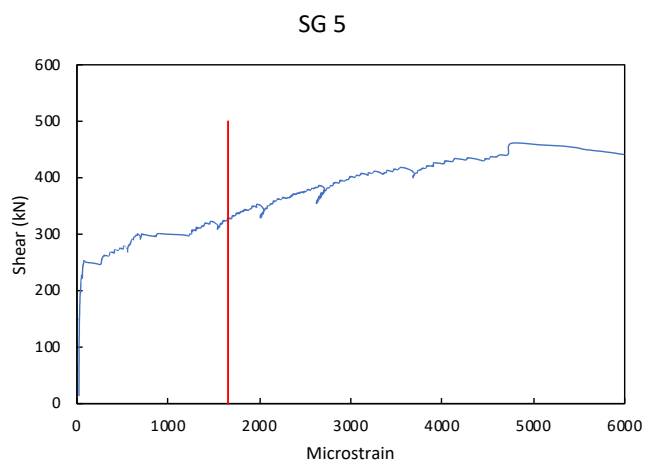
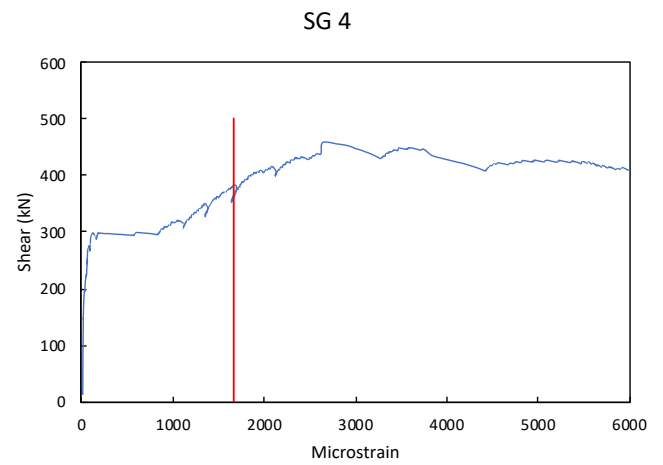
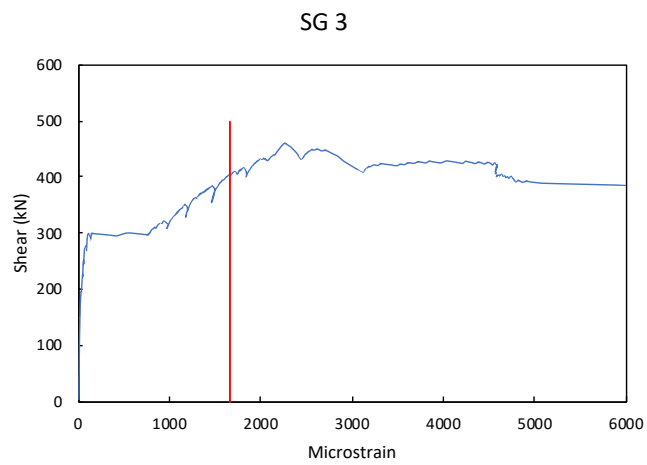
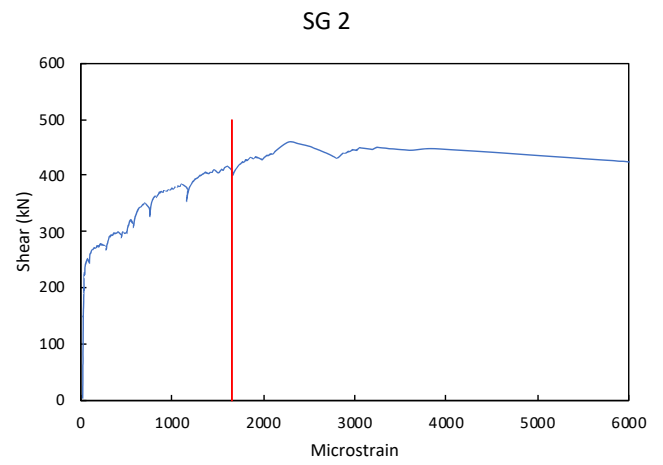
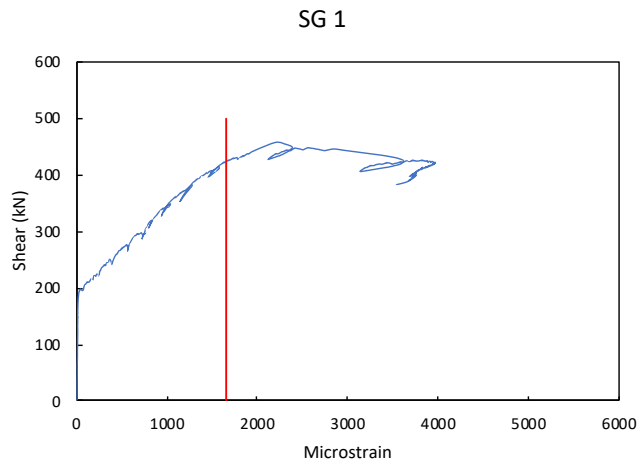


Figure 4.48: Shear versus strain for transverse hoops in specimen M4

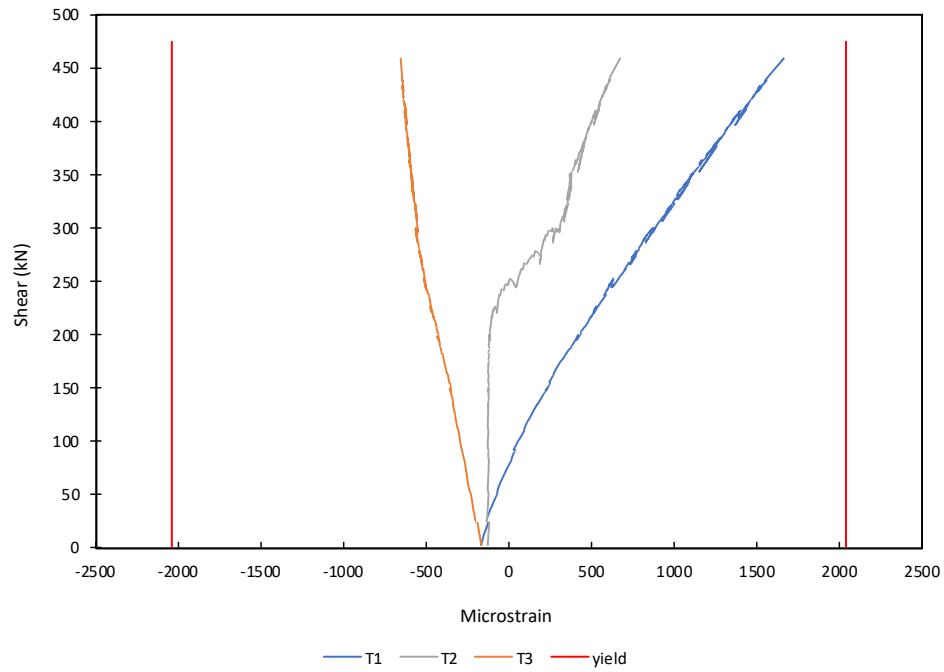


Figure 4.49: Shear versus strain for top longitudinal bar in specimen M4

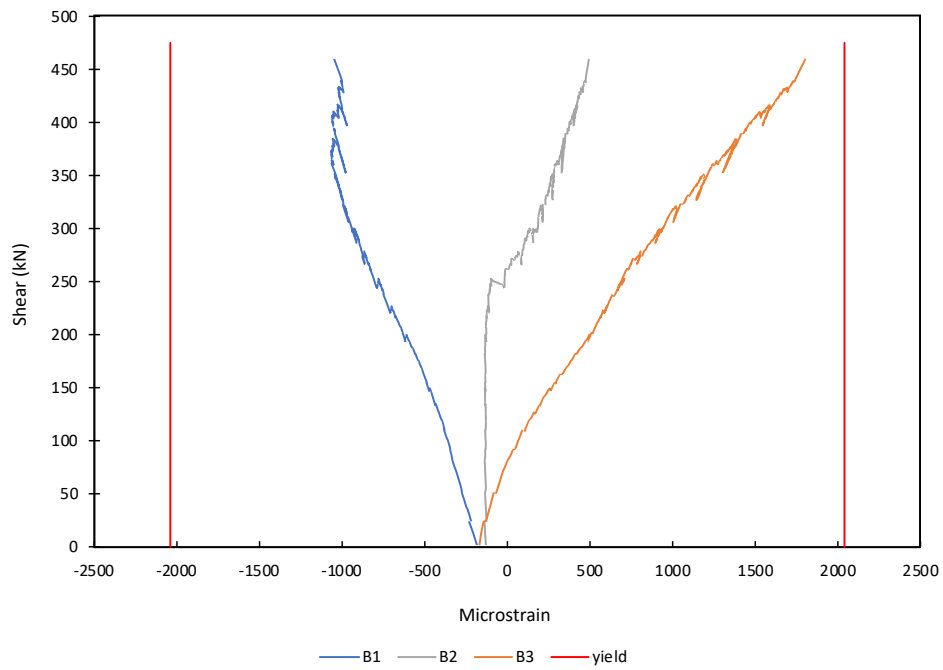


Figure 4.50: Shear versus strain for bottom longitudinal bar in specimen M4

Strain gauges were placed at three different locations on one 25M top bar and on one 25M bottom bar (see Fig. 3.27). Figures 4.49 and 4.50 show the shear versus strain relationships for these strain gauges. Before shear was applied, the column was under axial compression only. All strain gauges started with negative strains. When the column was loaded in shear, the top east strain gauge, T1, experienced tensile strains at a shear of 76 kN. Due to the moment, bottom east gauge, B1, experienced compressive strains. On the other end, the bottom west gauge, B3, experienced tensile strains at a shear of 82 kN and the top east gauge, T3, experienced increasing compressive strains. Central strain gauges, T2 and B2, stayed in compression up to a shear of 245 and 262 kN respectively, before they experienced tensile strains. None of the strain gauges on the longitudinal 25M bars yielded.

The bar elongations were measured by four LVDTs in order to obtain the average strains in the bars. The average strain was determined over a gauge length of 250 mm. when maximum shear was reached, the highest average strain was 0.00341 on the top east LVDT. All other LVDTs were below the yield strain of 0.0021 of the 25M bars. Figure 4.51 shows the shear versus average strain relationships for each LVDT.

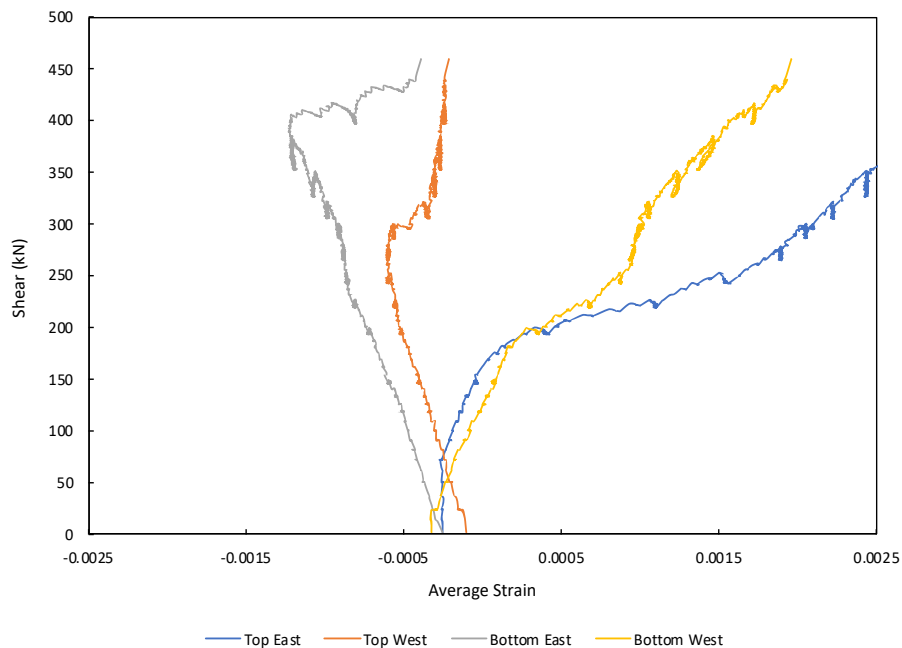


Figure 4.51: Average bar elongation strains for specimen M4

Figure 4.52 shows the results from the LVDTs, placed to form rosette sets, on specimen M4. M4 had two rosette sets, one on the west end and one on the east end (see Fig. 3.24). The horizontal strains, ϵ_x , at mid depths started negative under axial compression. At a shear of 275 kN, ϵ_x started growing. The horizontal strain increased to tensile strains of 0.0001427 and 0.0001481 on the west and east ends, respectively. These strains were observed, when maximum shear was reached. The vertical strain, ϵ_y , remained negligible up to a shear of 250 kN on the west end and 200 kN on the east end. At this load level the vertical strain started to increase due to increasing tensile strains. Coinciding with the formation of the first inclined shear crack between load stage 4 and load stage 5. The vertical strain reached a maximum of 0.00430 and 0.00386 on the west and east ends, respectively, when the specimen failed in shear. Vertical strains on both ends of the column, were higher than the yield strain of 0.0016 of the No. 3 transverse hoops. All strain gauges were yielding at failure. The principal tensile strain, ϵ_1 , at failure was 0.607% on the west side and 0.527% on the east side. Shear strain, γ_{xy} , at failure was 0.647% on the west end and 0.538% on the east side. The principal angle, θ_p , at failure was 30.0° on the west side and 30.0° on the east side. It was noted that the angle of the critical shear crack near the rosette at failure was 28.6° on the west side and 27.7° on the east side.

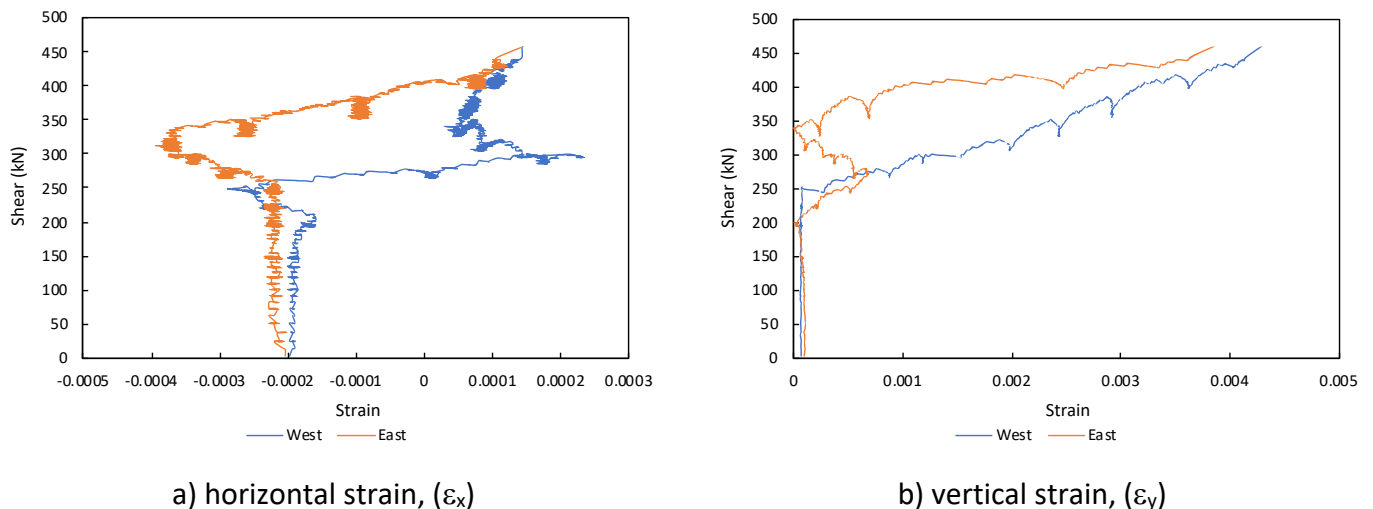
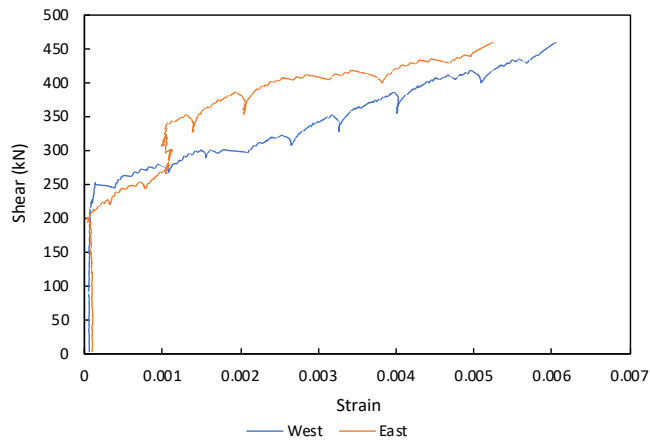
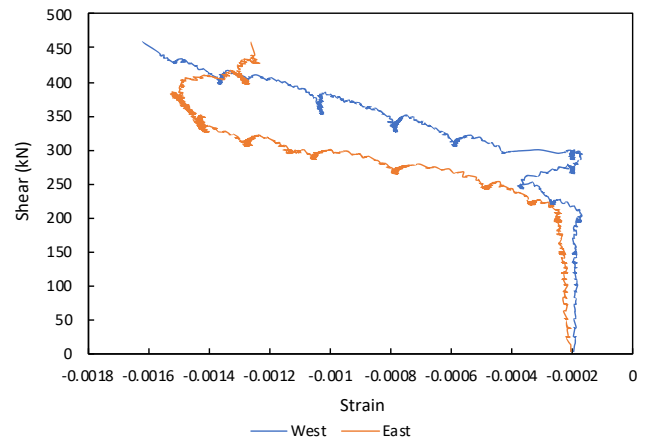


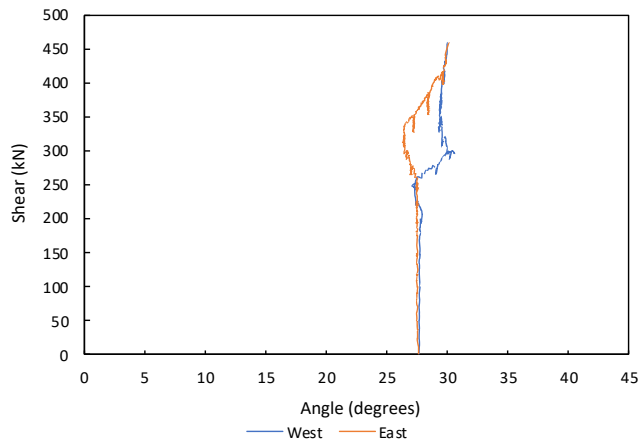
Figure 4.52: Principal strain and angle from specimen M4 rosettes



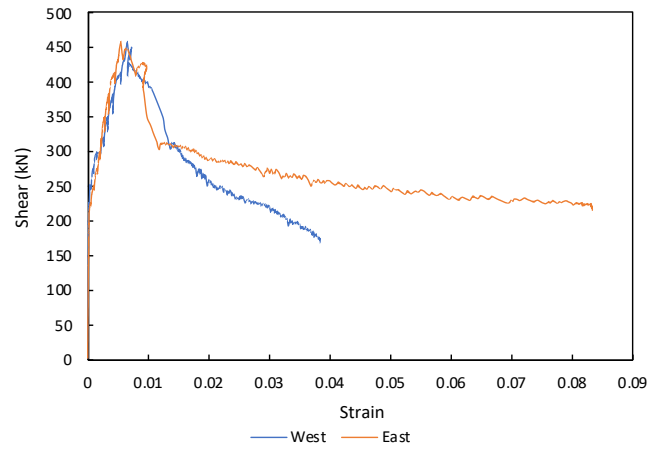
c) principal tensile strain, (ϵ_1)



d) principal compressive strain, (ϵ_2)



e) principal angle, (θ_p)



f) shear strain, (γ_{xy})

Figure 4.52 cont.: Principal strain and angle from specimen M4 rosettes

5 Analysis of Results

5.1 Discussion and Comparison of Experimental Results

5.1.1 Shear-Deflection Responses

A comparison of the shear-deflection responses of the four columns is shown in Fig. 5.1.

Column M1 reached the lowest peak shear of 339 kN, and it can be observed that it had the lowest post-cracking stiffness. Column M2 reached a higher peak shear of 366 kN and had a stiffer post-cracking response compared to M1. Specimen M3 had a post-cracking stiffness similar to that of M2 and reached a peak shear of 388 kN. Column M4 had the highest post-cracking stiffness of the four columns and reached a significantly higher peak shear of 459 kN.

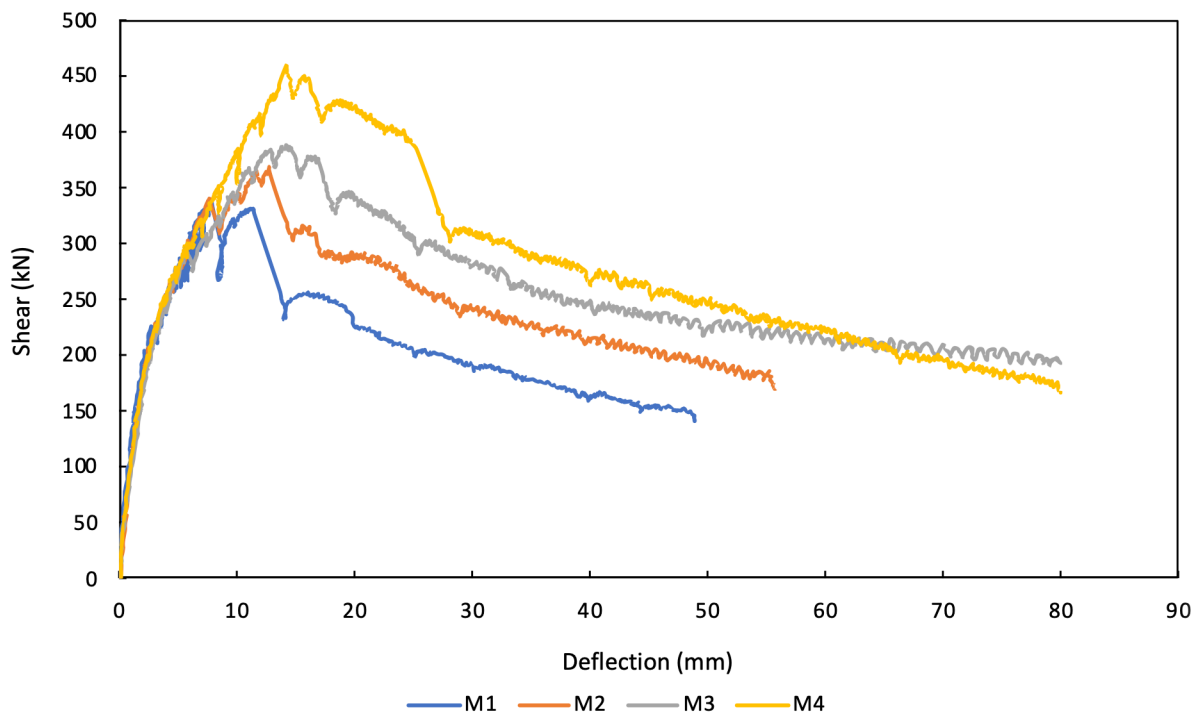


Figure 5.1: Shear-deflection responses of column specimens

Increased amounts of transverse hoops resulted in increased shear capacities and larger deflections at maximum shear as shown in Table 5.1.

Table 5.1: Comparison of peak shears and deflections of column specimens (hoop spacings given in brackets)

	M1 (200 mm)	M2 (150 mm)	M3 (100 mm)	M4 (75 mm)
Peak Shear (kN)	339	366	388	459
Peak Deflection (mm)	7.62	12.56	14.10	14.20
Shear reinforcement ratio (%)	0.284	0.379	0.568	0.757

5.1.2 Crack Widths

The development of shear cracking is summarized in Fig. 5.2. At a shear of 225 kN, the shear crack widths in M1 and M2 were 0.10 mm. These were larger than the shear crack widths of 0.05 mm in column M3 and M4 at this load level. Beyond this load level and for comparable shears, M1 had significantly wider shear cracks than the other columns, with M4 having smaller crack widths than the other columns. The transverse hoops were effective in reducing the shear crack widths when comparing specimens M4 to M1. At failure M1 had a critical shear crack width of 1.0 mm compared to 0.8 mm for M2, 0.5 mm for M3 and 0.35 mm for M4. The maximum recorded shear crack widths were 1.5 mm for M1 and 1.2 mm for M3. No shear crack widths were recorded beyond the shear failure load stage for specimens M2 and M4 due to excessive spalling of the cover concrete. The maximum recorded shear cracks are shown on a larger scale in Fig 5.3. The shear crack patterns at failure are shown in Fig 5.4 for all specimens.

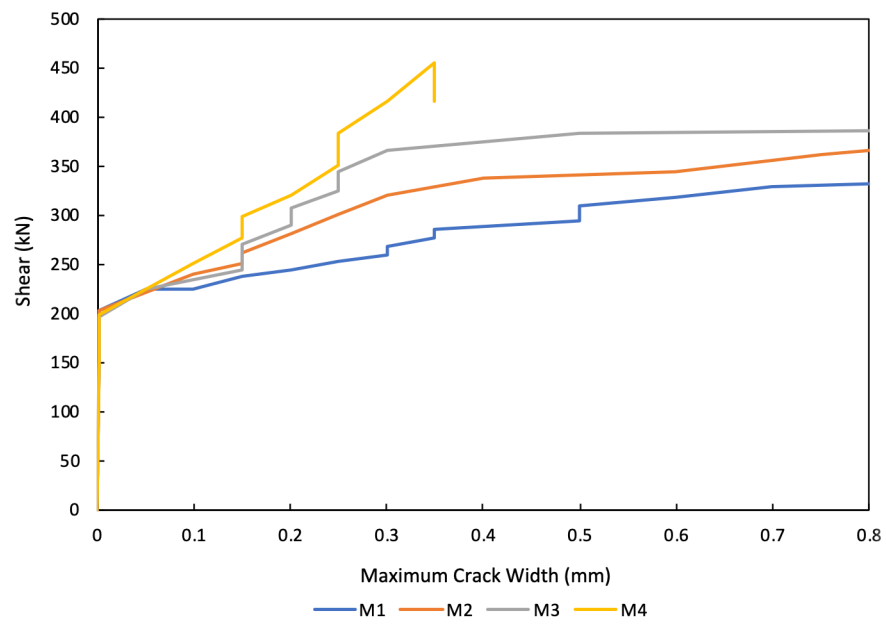


Figure 5.2: Shear versus maximum shear crack width for specimens M2, M3 and M4

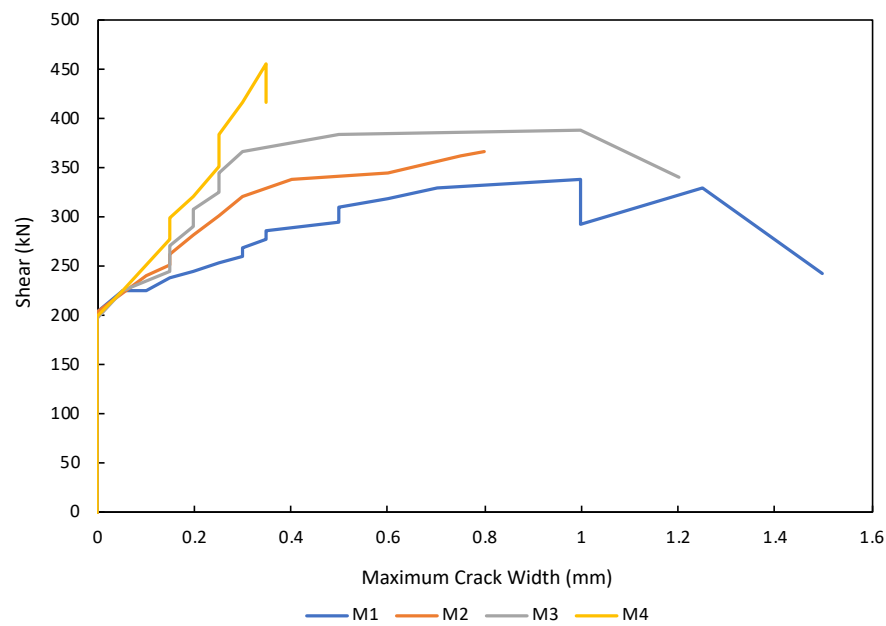
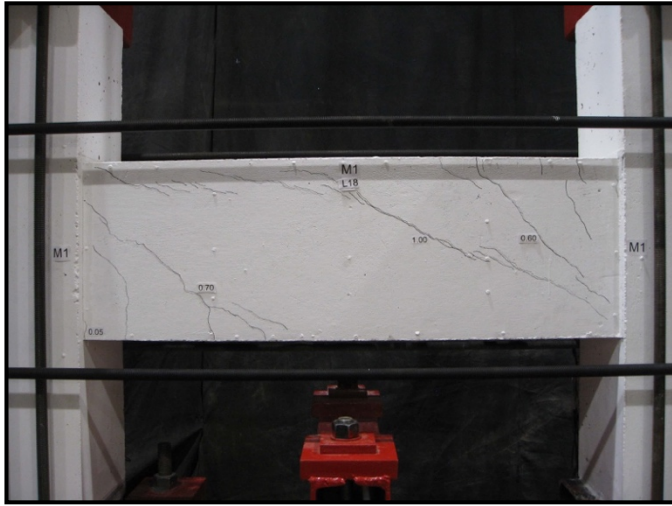
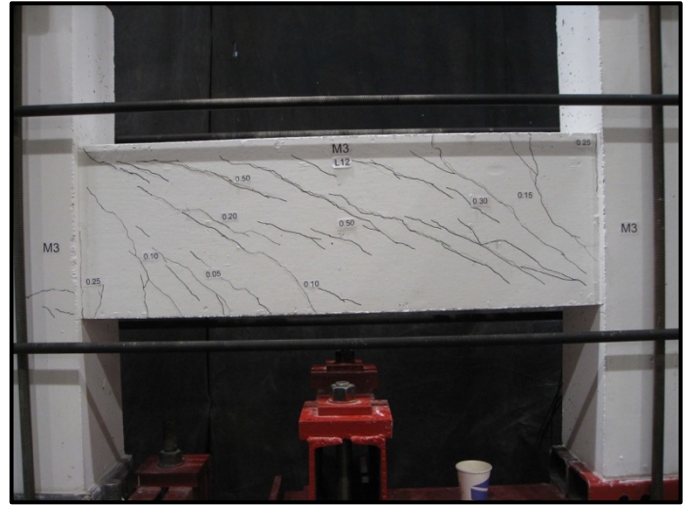


Figure 5.3: Shear versus maximum shear crack widths for specimens M1, M2, M3 and M4



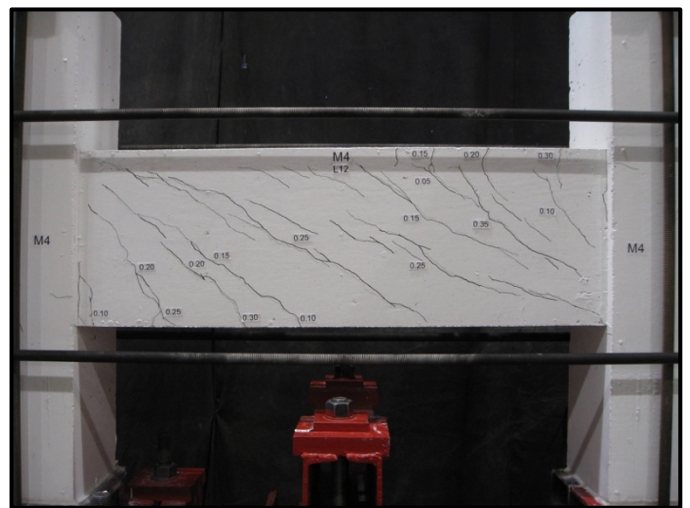
M1



M3



M2



M4

Figure 5.4: Shear crack patterns at maximum shear

Figure 5.5 shows the flexural cracks on the west and east sides for all four columns, respectively. Up until first cracking all four columns exhibited similar behaviour. Beyond first cracking M3 and M4 had significantly higher flexural cracks than M1 and M2. Both M3 and M4 reached maximum flexural cracks of 0.3 mm. M2 saw maximum flexural cracks of 0.15 mm compared to 0.05 mm for M1. In general, flexural crack patterns were identical between the west and east ends of the columns except for column M1 which showed a maximum of 0.05 on the west side compared to 0.02 on the east side.

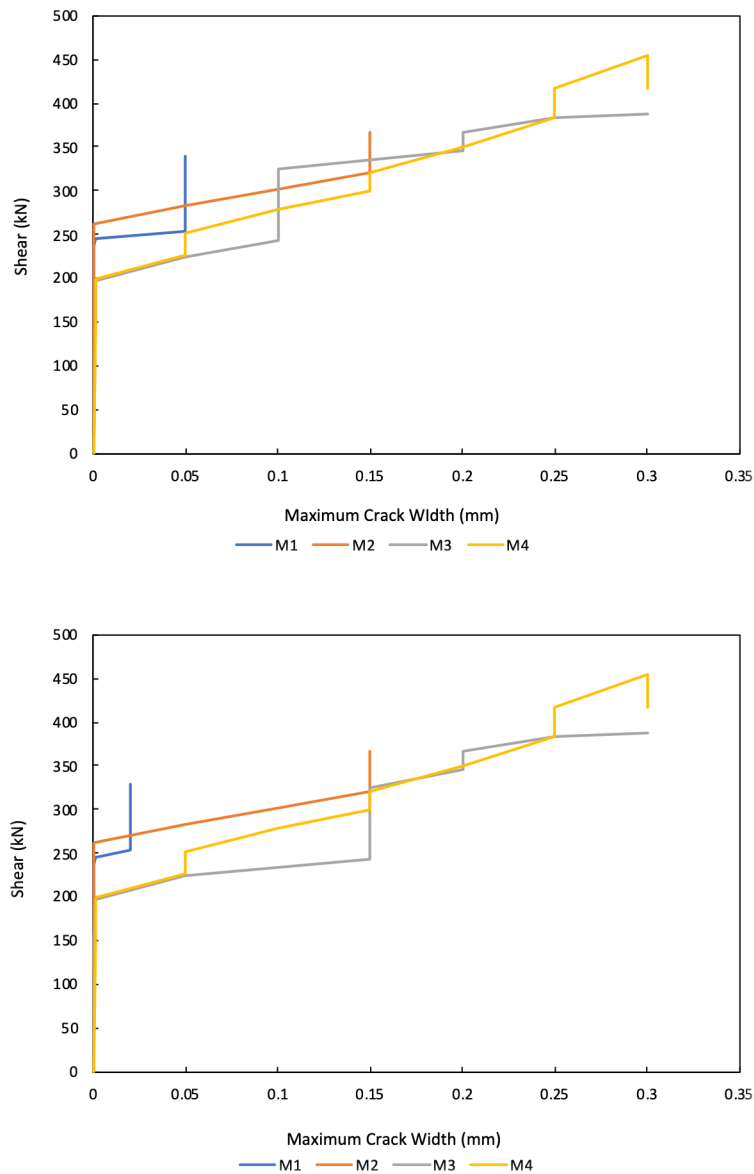


Figure 5.5: Maximum flexural crack widths, west end (top) east end (bottom)

5.2 Predicted Shear Capacities from Sectional Analyses

This section presents predictions from three sectional design approaches. The first two approaches are based on MCFT to predict the shear strength of reinforced concrete members namely: the Canadian Highway Bridge Design Code (CSA, 2019) general and simplified method as well as the computer program Response 2000 (Bentz, 2000 and 2001 and Bentz and Collins, 2015). In addition, the code provisions of the American Concrete Institute (ACI) (ACI Committee 318, 2019) were also used to predict the shear capacities.

5.2.1 Shear Resistance Predicted Using Canadian Highway Bridge Design Code

The nominal shear resistance was determined using the general method of the Canadian Highway Bridge Design Code (CSA, 2019). This design approach has its basis in the Modified Compression Field Theory (Bentz and Collins, 2006; Collins et al., 1996). The critical shear section was located at a distance equal to the effective shear depth, d_v , from the end of the column. This effective shear depth was taken as 72% of the height, h , of the column cross section. The primary objective of this analysis was to determine the nominal shear resistance, V_n , of the columns. As such, material resistance factors, ϕ_s and ϕ_c , were taken as 1.0 for this analysis. An iterative procedure was used in order to determine, V_n , at the critical section, the steps of which are described below:

Step 1: A value for the nominal shear resistance, V_n , was assumed.

Step2: Determine the longitudinal strain, ε_x :

$$\varepsilon_x = \frac{\frac{M_n}{d_v} + V_n - 0.5N_f}{2(E_s A_s)} \quad (5.1)$$

Where, M_n , is the moment at the critical shear section corresponding to, V_n and, N_f , is the axial load applied on the column, A_s , is the area of reinforcing steel on the tension half of the section and E_s , is the elastic modulus of the reinforcing steel.

Step 3: Determine the factor, β , that takes into account the shear resistance of the diagonally cracked concrete:

$$\beta = \frac{0.4}{1 + 1500\varepsilon_x} \quad (5.2)$$

Step 4: Calculate the angle of principal compression, θ :

$$\theta = 29 + 7000\varepsilon_x \quad (5.3)$$

Step 5: Calculate the nominal shear resistance provided by the diagonally cracked concrete, V_c :

$$V_c = \beta\sqrt{f'_c}b_vd_v \quad (5.4)$$

Where, f'_c , is the concrete compressive strength determined from material testing, b_v , is the effective web width, (250 mm for the columns considered) and d_v , (288 mm for the columns considered) taken as 0.72 times the column cross section depth (400 mm).

Step 6: Calculate the nominal shear resistance provided by the vertical steel hoops, V_s :

$$V_s = \frac{f_y A_v d_v \cot \theta}{s} \quad (5.5)$$

Where, f_y , is the yield stress of the hoop reinforcement determined from material testing, A_v is the cross-sectional area of the two hoop legs and s , is the uniform hoop spacing.

Step 7: Calculate the nominal shear resistance:

$$V_n = V_c + V_s \quad (5.6)$$

Step 8: The nominal shear resistance, V_n , calculated in Step 7 was compared with the assumed value in Step 1. This procedure is repeated until the solution converged.

5.2.1.1 CHBDC General Method Results

The predicted nominal shear resistance, $V_{predicted}$, by the general method described above is shown in Table 5.2. The reported values are the predicted shear resistances at the critical section, d_v , from the end of the column. Comparing the predictions to the experimental shear, V_{test} , it is clear that the general shear design method of the 2019 CHBDC consistently gives conservative shear predictions. The $V_{test}/V_{predicted}$, ranged from 1.24 to 1.44, with columns M1 and M2 being predicted slightly more conservatively than columns M3 and M4.

Table 5.2: Comparison of predicted shear capacities using CHBDC general method with shear achieved during testing

	M1	M2	M3	M4
$\epsilon_x \times 10^3$	0.299	0.366	0.499	0.632
β	0.276	0.258	0.229	0.205
θ (deg.)	31.1	31.6	32.5	33.4
V_c (kN)	122	113	99	89
V_s (kN)	113	147	213	274
$V_{predicted}$ (kN)	235	261	312	363
V_{test} (kN)	339	366	388	459
$V_{test}/V_{predicted}$	1.44	1.40	1.24	1.26

5.2.1.2 CHBDC Simplified Method Results

The nominal shear resistances were also determined using the simplified method of the CHBDC (CSA, 2019). For non-prestressed components not subjected to axial tension, and provided that the specified yield strength of the longitudinal reinforcement does not exceed 400 MPa and the design concrete strength does not exceed 60 MPa, the value of the angle of inclination, θ , shall be taken as 42° and the value of, β , shall be 0.18 for members with at least the minimum amount of transverse reinforcement required. The predicted nominal shear resistances, $V_{predicted}$, by the simplified method are shown in Table 5.3. Comparing the predictions to the

experimental maximum shears, V_{test} , it is clear that the simplified shear design method of the 2019 CHBDC is overly conservative. The $V_{test}/V_{predicted}$, ranged from 1.63 to 2.17, with columns M1 and M2 being predicted at 50% or less of their actual capacity.

Table 5.3: Comparison of predicted shear capacities using CHBDC simplified method with shear achieved during testing

	M1	M2	M3	M4
β	0.18	0.18	0.18	0.18
θ (deg.)	42.0	42.0	42.0	42.0
V_c (kN)	80	79	78	78
V_s (kN)	76	102	153	204
$V_{predicted}$ (kN)	156	181	231	282
V_{test} (kN)	339	366	388	459
$V_{test}/V_{predicted}$	2.17	2.03	1.68	1.63

5.2.2 Shear Resistance Predicted Using Response 2000

The shear resistance was determined using the Response 2000 (Bentz and Collins, 2015) sectional analysis program discussed in Section 2.2.2. The predicted nominal shear resistances using Response 2000 are shown in Table 5.4. These values correspond to a critical shear section located at a distance equal to the effective shear depth, d_v , from the end of the column and a shear span of 0.6 m. For each specimen the corresponding concrete strength from the results of testing concrete cylinders in compression was used. For the reinforcing steel the material properties obtained by testing samples of the reinforcing bars were used for all specimens. The Response 2000 design input and analysis results for column M1 are shown in Fig. 5.6.

Table 5.4: Response 2000 nominal shear predictions compared to maximum experimental shears

	M1	M2	M3	M4
$V_{predicted}$ (kN)	256	311	385	453
V_{test} (kN)	339	366	388	459
$V_{test}/V_{predicted}$	1.32	1.18	1.01	1.01

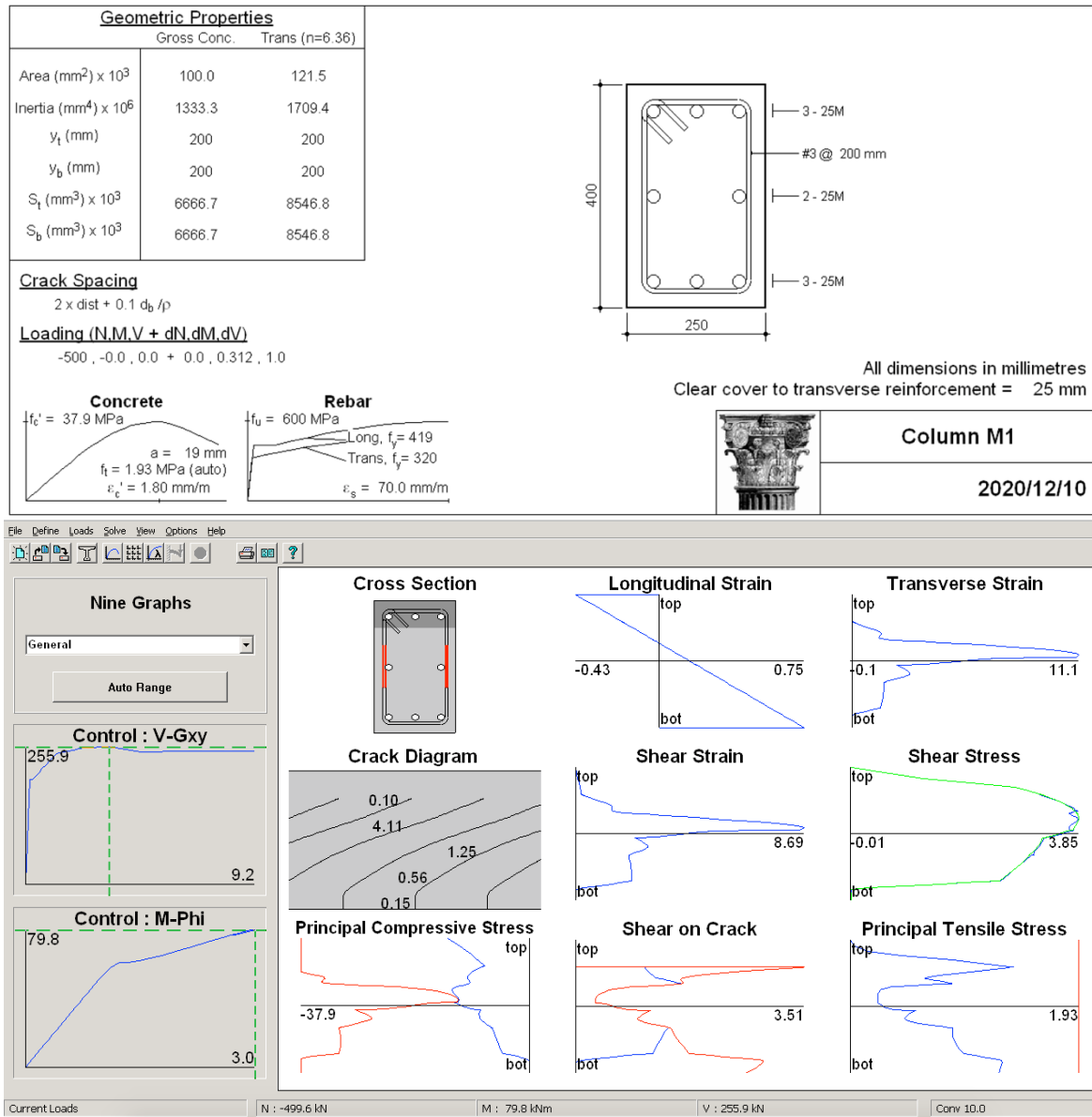


Figure 5.6: Response 2000 predictions for column M1, input data (top), predicted response (bottom)

5.2.3 Shear Resistance Predicted Using ACI Committee 318 (2019) Provisions

The ACI code provisions (see Section 2.2.3) present the following equation for calculating, V_u , for members subjected to combined shear, moment, and axial compression (ACI Committee 318, 2019):

$$V_u = V_c + V_s \quad (5.7)$$

$$V_s = \frac{A_v f_{yt} d}{s} \quad (5.8)$$

For member subjected to axial compression, with at least the minimum amount of transverse reinforcement required. V_c , is evaluated as follows:

$$V_c = \left[2\lambda\sqrt{f'_c} + \frac{N_u}{6A_g} \right] b_w d \quad (5.9)$$

Alternatively, the following expression may be used:

$$V_c = \left[8\lambda(\rho_w)^{\frac{1}{3}}\sqrt{f'_c} + \frac{N_u}{6A_g} \right] b_w d \quad (5.10)$$

Where, N_u , is the axial load applied to the section, A_g , is gross cross-sectional area, f'_c , is concrete compressive strength, b_w , is the web width of the section, and d , is the effective depth of section. ρ_w , is the longitudinal reinforcement ratio and may be taken as the sum of the areas of longitudinal bars located more than two thirds of the overall member depth away from the extreme compression fiber. The term, λ , is a modification factor to account for lightweight concrete and is taken as 1.0 for normal weight concrete. A_v , is the area of transverse reinforcement within the spacing, s , and f_{yt} , is the yield stress of the transverse steel.

The predicted nominal shear resistances, $V_{predicted}$, using the ACI 318-19 code provisions, using Eq. 5.9, are shown in Table 5.5. Comparing the predictions to the experimental shear, V_{test} , it is clear that the ACI 318-19 shear provisions are relatively conservative. The $V_{test}/V_{predicted}$, ranged from 1.50 to 1.30.

Table 5.5: Comparison of predicted shear capacities using ACI (ACI Committee 318, 2019) with maximum shear achieved during testing

	M1	M2	M3	M4
V_c (kN)	151	150	149	149
V_s (kN)	75	100	150	201
$V_{predicted}$ (kN)	226	250	299	349
V_{test} (kN)	339	366	388	459
$V_{test}/V_{predicted}$	1.50	1.47	1.30	1.32

5.2.4 Comparison of Shear Resistance Predictions from Sectional Design Models

The predictions made by sectional analysis methods presented in this section are compared in Fig. 5.7.

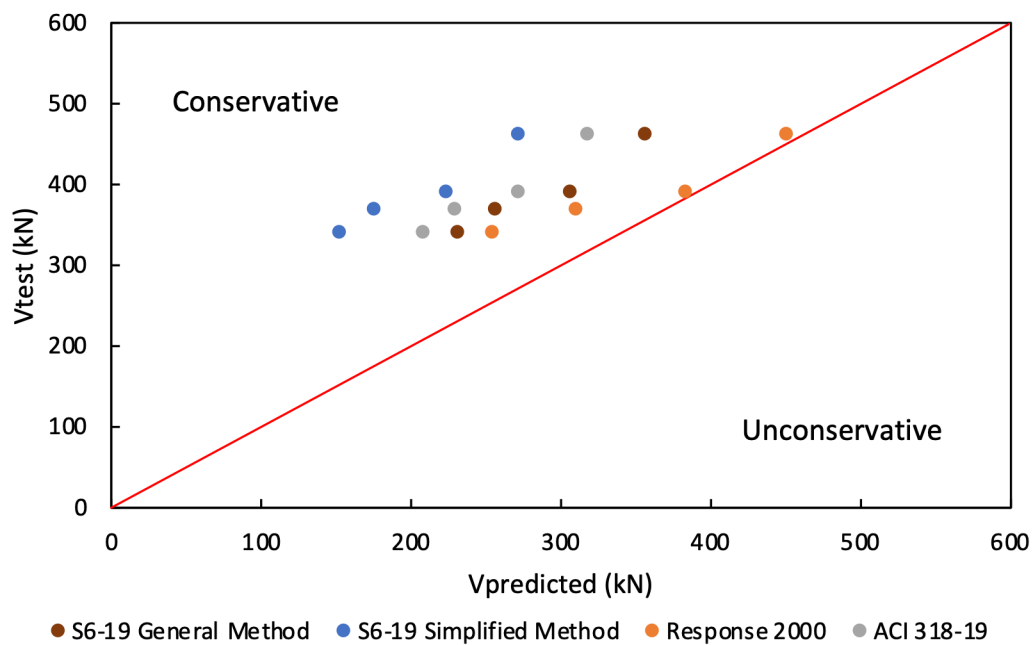


Figure 5.7: Comparison of predictions made by sectional analysis methods

5.3 Predicted Behaviour from Truss and Strut or Arch Models

The use of sectional models such as the variable angle truss model or the MCFT to predict the shear strength of RC columns does not consider the compressive arch action that is possible in the columns. This effect becomes important in columns with high axial loads and/or small aspect ratios. In this section, predictions using models from the literature that consider the arch action will be presented.

5.3.1 Approach of Priestley et al. (1994)

As outlined in Section 2.4.2 Priestley et al. (1994) proposed the following equation for calculating, V_u , for members subjected to combined shear, moment, and axial compression under cyclic lateral loads:

$$V_u = V_c + V_s + V_p \quad (5.11)$$

The concrete mechanism term is:

$$V_c = k\sqrt{f'_c}A_e, \text{ and } A_e = 0.8 A_g \quad (5.12)$$

Where, k , within plastic end regions depends on member's displacement ductility. The degradation factor is only applied to the concrete component.

Truss mechanism component for rectangular columns is:

$$V_s = \frac{A_v f_{yh} D'}{s} \cot 30^\circ \quad (5.13)$$

Where, D' , is the distance between centers of peripheral hoops.

The contribution of transverse reinforcement to shear strength is based on a truss mechanism using a 30° angle between the compression diagonals and the members longitudinal axis.

The shear component from the direct strut is:

$$V_p = P \tan \alpha = \frac{D - c}{2a} P \quad (5.14)$$

Where, D , is the overall depth of the section, c , is the depth of compression zone, and a , taken as, $L/2$, for a column subjected to reversed bending and taken as, L , for a column subjected to single bending.

The predicted nominal shear resistance, $V_{predicted}$, by Priestley et al. (1994) is shown in Table 5.6. Comparing the predictions to the experimental shears, V_{test} , it is clear that the shear resistance is overestimated. This approach overestimates the concrete and steel contribution. The concrete contribution was not reduced by the degradation factor, k , as the columns considered had no displacement ductility. The effective depth, D' , taken as the effective depth between peripheral hoops, to calculate the steel contribution, is approximately 20% higher than the effective depth suggested by the CHBDC (CSA, 2019) and the ACI (ACI Committee 318, 2019) provisions.

Table 5.6: Comparison of predicted shear capacities using the approach of Priestley et al. (1994)

	M1	M2	M3	M4
μ	1	1	1	1
k	0.29	0.29	0.29	0.29
V_c (kN)	143	141	139	139
V_s (kN)	139	185	278	371
V_p (kN)	106	106	105	105
$V_{predicted}$ (kN)	388	433	522	615
V_{test} (kN)	339	366	388	459
$V_{test}/V_{predicted}$	0.87	0.85	0.74	0.75

5.3.2 Truss-Arch Model by Pan and Li (2013)

The Truss-Arch Model explained in Section 2.4.3 considers the deformation compatibility between the truss and arch components in the column. The truss component consists of concrete and steel contribution based on the MCFT. The arch mechanism is assumed to be

related to a single compressive strut directed from the compression zone at the top toward that at the bottom. If the column is in double bending, the inclination of the strut is found from the line joining the centers of flexural compression at the top and at the bottom of the column. The arch contribution is derived from the condition of deformation compatibility between the truss model and the arch model. The full details of the deformability equations can be found in Section 2.4.3.3. The shear strength of a reinforced concrete column under monotonic loading is given by:

$$V_u = V_{ct} + V_s + V_a = (V_{ct} + V_s) \left(1 + \frac{K_a}{K_t} \right) \quad (5.15)$$

Table 5.7: Comparison of predicted shear capacities using the approach of Pan and Li (2013)

	M1	M2	M3	M4
V_{ct} (kN)	93	85	73	65
V_s (kN)	145	179	244	303
V_a (kN)	73	73	72	75
$V_{predicted}$ (kN)	311	337	389	443
V_{test} (kN)	339	366	388	459
$V_{test}/V_{predicted}$	1.09	1.09	1.00	1.04

The predicted nominal shear resistance, $V_{predicted}$, by Pan and Li (2013) is shown in Table 5.7. Comparing the predictions to the experimental shear, V_{test} ; the shear capacity is reasonably predicted. This approach slightly underestimates the shear strength of the column. The effective depth of the arch is derived by subtracting the thickness of concrete cover from the neutral axis depth of the section. However, in all tested columns in this series, the concrete cover did not spall at shear failure; therefore, the arch action was underestimated.

5.3.3 CHBDC General Method with Concrete Strut

The columns considered in this experiment had a small aspect ratio. It was evident that the axial load is providing an important benefit for such short columns. The approach by Pan and Li (2013) provides reasonable predictions but is cumbersome in terms of calculation. To account for the arch action shown in Fig. 5.8: a simpler approach would be to add a diagonal compressive strut component with the CHBDC (CSA, 2019) general method iterations. For a column in double bending, the inclination of the strut is found from the line joining the centers of flexural compression at the top and at the bottom of the column. To calculate the concrete strut component, the expression by Priestley et al. (1994) could be used:

$$V_p = P \tan \alpha = \frac{h - c}{L} P \quad (5.16)$$

The neutral axis depth, c , can be estimated using the expression proposed by Paulay and Priestley (1992):

$$c = \left(0.25 + 0.85 \frac{P}{f'_c A_g} \right) h \quad (5.17)$$

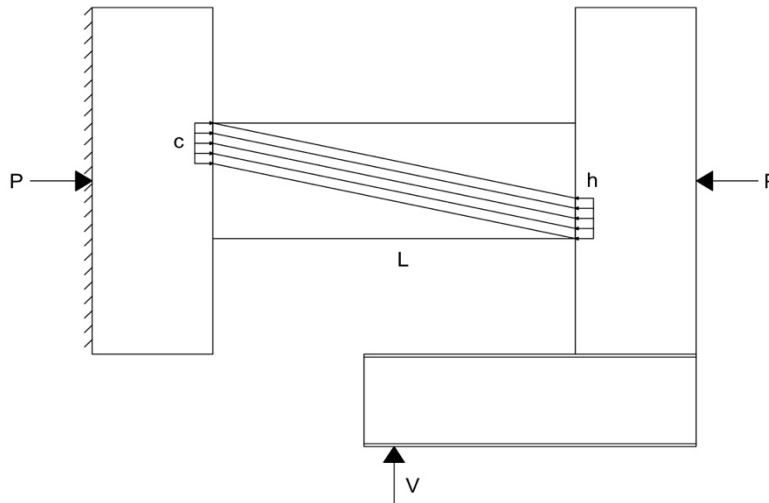


Figure 5.8: Idealized concrete strut for a typical specimen tested in this series

The depth of the neutral axis, c , obtained from the expression by Paulay and Priestley (1992) was compared to the depth of the compression zone corresponding to the maximum flexural resistance obtained by flexural and axial load analysis from Response 2000 (see Fig. 5.9). The predicted depth of compression using Response 2000 is approximately 140 mm. The value of the neutral axis depth, c , was determined analytically for each specimen and compared to the value determined in Eq. 5.17. This comparison is shown in Table 5.8. It was apparent that the expression provided reasonable estimates and it was decided to use the more accurate analytically determined value of, c , in the expression by Priestley et al. (1994) to calculate the concrete strut.

Table 5.8: Comparison of neutral axis depth

	M1	M2	M3	M4
$c_{priestley}$ (mm)	144.85	145.82	147.35	147.35
$c_{analytically}$ (mm)	135.60	137.87	141.46	141.46

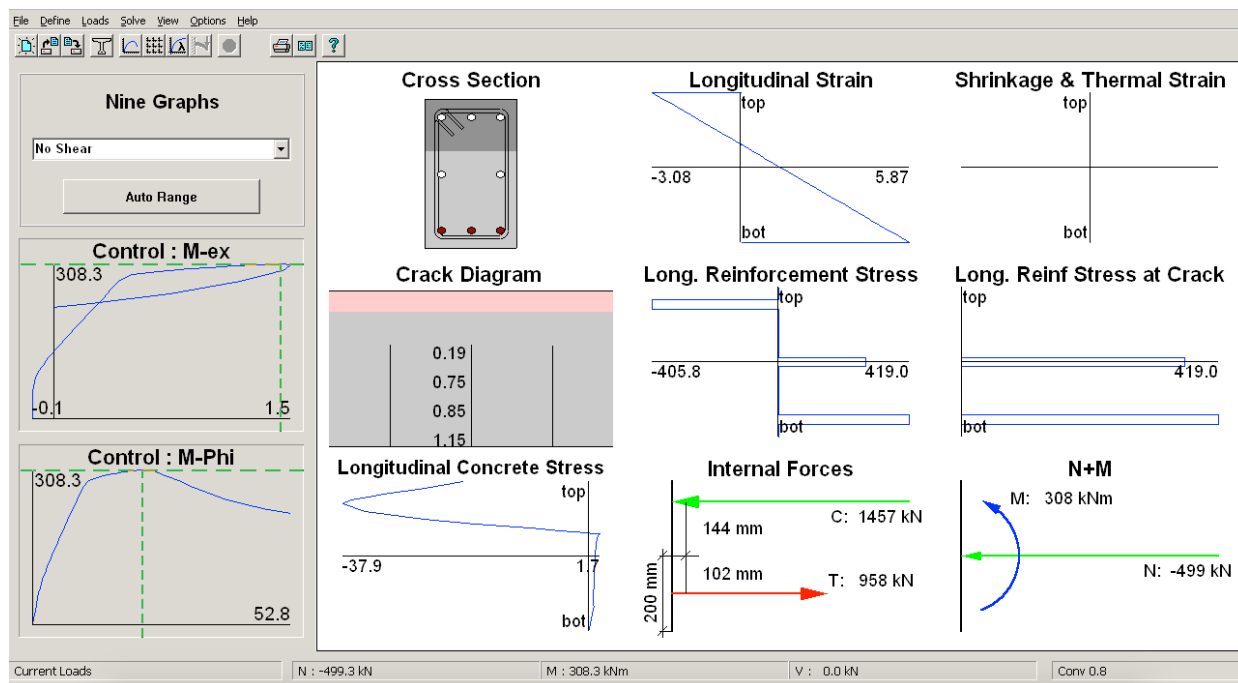


Figure 5.9: Response 2000 flexural analysis

The iterative procedure outlined in Section 5.2.1 is repeated with the contribution from the concrete strut, V_p , added in step 7.

The predicted nominal shear resistance, $V_{predicted}$, is shown in Table 5.9. Comparing the predictions to the experimental shear resistances, V_{test} , the predictions are better than predictions made in Section 5.2.1.1 when the strut contribution wasn't considered. With $V_{test}/V_{predicted}$ ranging from 0.99 to 1.08 instead of 1.24 to 1.44.

Table 5.9: Comparison of predicted shear capacities using CHBDC (CSA, 2019) general method with the superimposed concrete strut

	M1	M2	M3	M4
V_c (kN)	101	94	84	76
V_s (kN)	106	139	202	260
V_p (kN)	106	106	105	105
$V_{predicted}$ (kN)	313	339	391	441
V_{test} (kN)	339	366	388	459
$V_{test}/V_{predicted}$	1.08	1.08	0.99	1.04

5.3.4 Comparison of Shear Resistance Predictions from Truss and Strut Models

Figure 5.10 shows a comparison of all the truss and arch approaches considered in this section. The strut and arch methods gave accurate estimates when compared to the sectional models in Section 5.2, except for the model by Priestley et al. (1994). Comparing the predictions of the CHBDC (CSA, 2019) general method with and without the concrete strut. The predictions made in Section 5.3.3 were better than the predictions in Section 5.2.1.1 when the strut contribution wasn't considered.

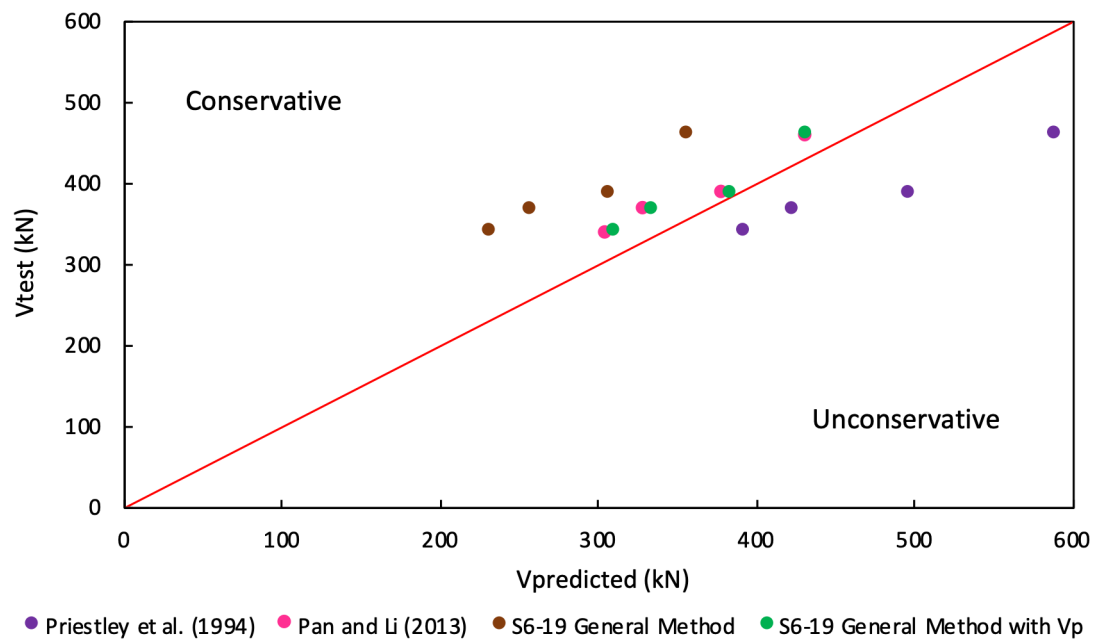


Figure 5.10: Comparison of the different truss and arch prediction models

5.4 Shear Response Predicted using Non-Linear Finite Element Analysis

An analysis of the test specimens was carried out using the 2D non-linear finite element software VecTor2 (Vecchio, 2018) discussed in Section 2.4. The program is based on the Modified Compression Field Theory (Vecchio and Collins, 1986) and uses a smeared rotating crack model. The analysis was carried out to investigate the full behaviour of the columns, including possible strut action provided by the constant axial load. The 2-D non-linear finite element analysis accounted for effects such as tension stiffening and compression softening as well as using more detailed material properties.

5.4.1 Finite Element Model

Before the analyses could be carried out, a finite element model for the column specimens was made using the pre-processor FormWorks (Wong, 2002). The finite element model used for all specimens is shown in Fig. 5.12. A combination of quadrilateral and triangular elements were used, with a maximum width and height of 100 mm. The longitudinal reinforcement in the column was modelled as discrete truss elements assumed to be perfectly bonded with the concrete, indicated by horizontal lines in the test region. Similarly, the vertical 20M and 10M bars in the wall, were modeled with vertical truss bars. The rest of the steel reinforcement including, the 10M horizontal bars in the wall and the 10M ties at the ends of the wall were modelled as smeared reinforcement layers in the concrete, that is, the steel was assumed to be uniformly distributed in these elements. The transverse hoops in the column were modeled by smeared reinforcement in the vertical direction. The transverse reinforcement ratio for each column was used to vary the amount of smeared vertical reinforcement in each specimen. Also shown in Fig. 5.12 are the 6-300 kN loads applied on both the moving and fixed walls of the specimen to represent the forces from the pre-tensioned clamps. The clamps were used to fix the specimen to the fixed beam (presented here by joints restrained in the x and y directions). On the other hand, the clamps fix the moving end of the specimen to the loading beam as shown in Fig. 5.11. The 500 kN constant axial load is applied by 2-250 kN point loads on both ends of the walls. The specimen was loaded by applying an upwards displacement to the

loading beam at the column centerline location. The axial load was applied in the first load stage and kept constant. Then the displacement needed to cause failure was applied in 20 load stages. After the VecTor2 analysis was complete the post-processor Augustus (Bentz, 2003) was used to visualize the results. The models used in analysis are summarized in Table 5.10. Information on these models can be found in the VecTor2 & FormWorks User's Manual, Second Edition (Wong et al., 2013). The ductile steel reinforcement stress-strain response consisted of three parts, an initial linear-elastic portion, a yield plateau and a non-linear strain-hardening phase. The concrete was modelled using a parabola for the pre-peak compression response and the modified Park-Kent post-peak compression response which takes into account concrete confinement. All material property inputs were taken directly from the material tests conducted as part of this experimental program. The modulus of elasticity of the reinforcement was assumed to be 200000 MPa.

Table 5.10: Models used in VecTor2

	Description	Model
Concrete	Compression Pre-Peak Response	Popovics (Normal Strength Concrete)
	Compression Post-Peak Response	Modified Park-Kent
	Compression Softening	Vecchio 1992-A (e1/e2-Form)
	Tension Stiffening	Modified Bentz 2003
	Tension Softening	Bilinear
	Confined Strength	Kupfer/Richart
	Dilation	Variable – Isotropic
	Cracking Criterion	Mohr-Coulomb (Stress)
	Crack Stress Calculation	Basic (DSFM/MCFT)
	Crack Width Check	Agg/2.5 Max Crack Width
	Crack Slip Calculation	Walraven
Reinforcement	Hysteretic Response	Nonlinear with Plastic Offsets
	Dowel Action	Tassios (Crack Slip)
	Buckling	Akkaya 2012
Bond	Hysteretic Response	Bauschinger Effect (Seckin)
	Concrete Bond	Eigenhausen
Analysis	Cracking Spacing	CEB-FIP 1978 - Deformed

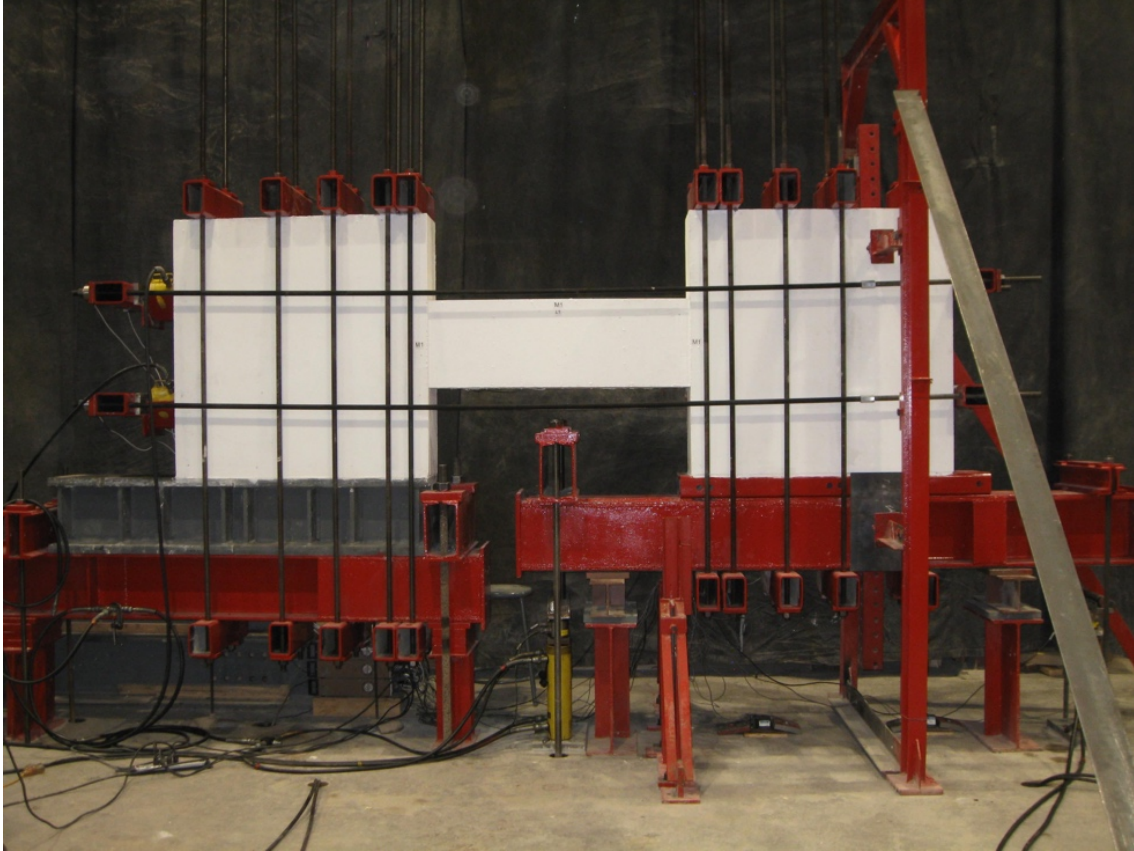


Figure 5.11: Photograph of McGill University testing frame

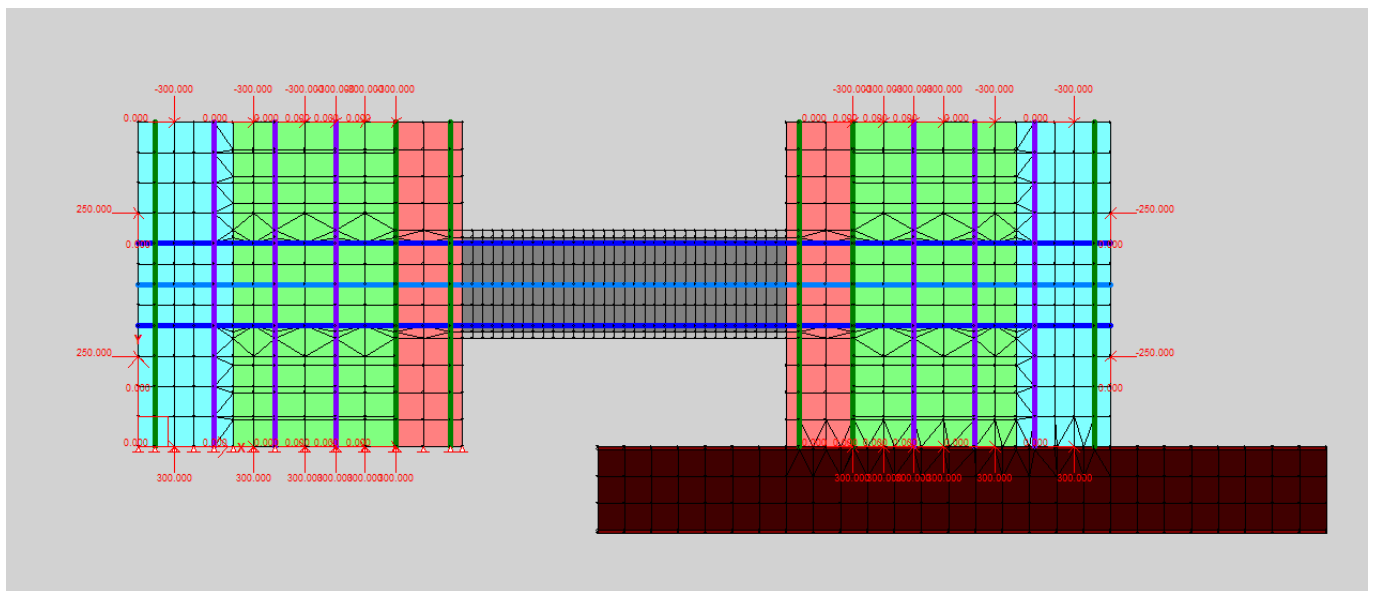


Figure 5.12: Finite element model for the column specimens

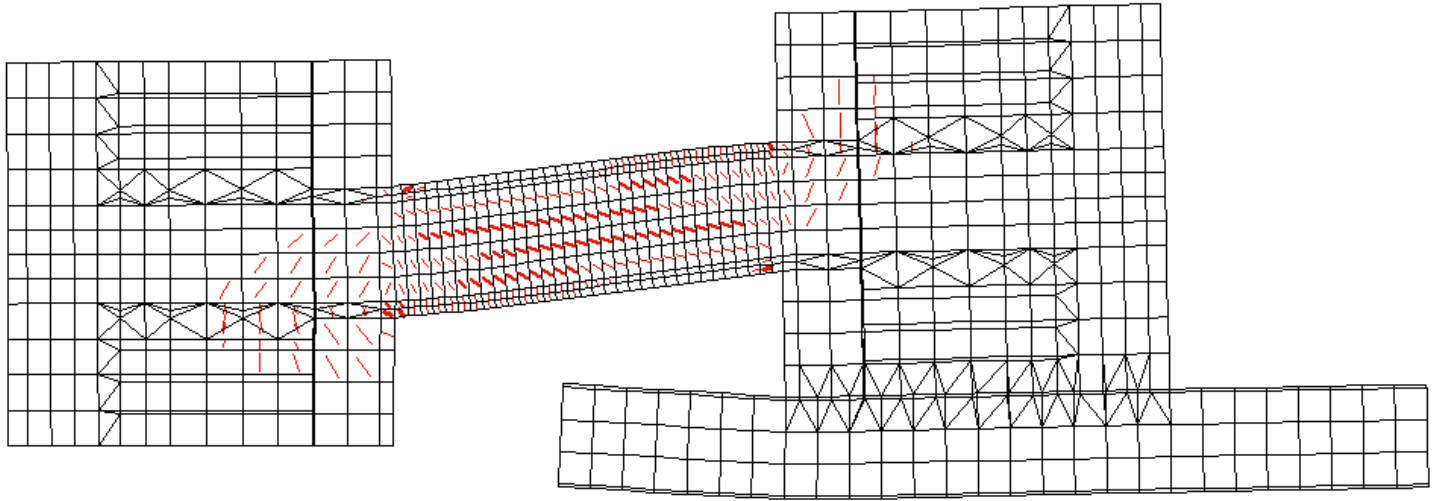


Figure 5.13: Predicted deflected shape and crack pattern of specimen M3 at predicted maximum shear

5.4.2 Comparison with Experimental Results

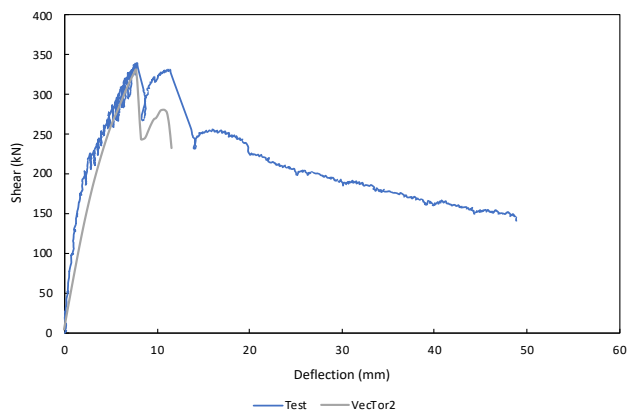
The predicted shear capacities of the four columns, using the finite element model are given in Table 5.11. The predicted deflected shape and crack pattern of specimen M3 at maximum shear is shown in Fig. 5.13. The predicted capacities were within 4% of the actual shear capacity observed during the experimental program except for specimen M3. The model predicted 415 kN for M3 which was an overestimation by 7% of the actual shear capacity of 388 kN.

Table 5.11: Comparison of predicted shear capacities from VecTor2 with shear capacities achieved during testing

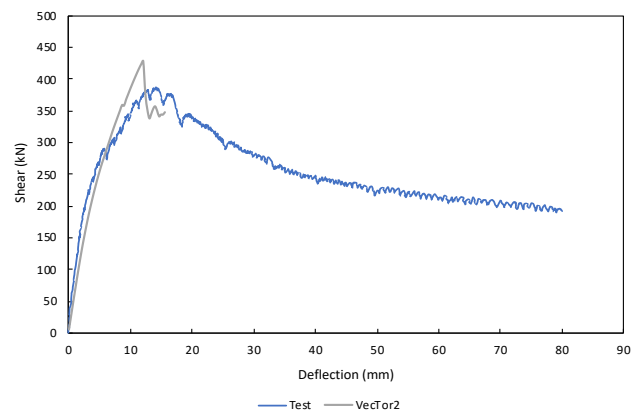
	M1	M2	M3	M4
V_{test} (kN)	339	366	388	459
$V_{Vec\ Tor2}$ (kN)	327	359	415	449
$V_{test}/V_{Vec\ Tor2}$	1.04	1.02	0.93	1.02

5.4.2.1 Shear-Deflection Responses

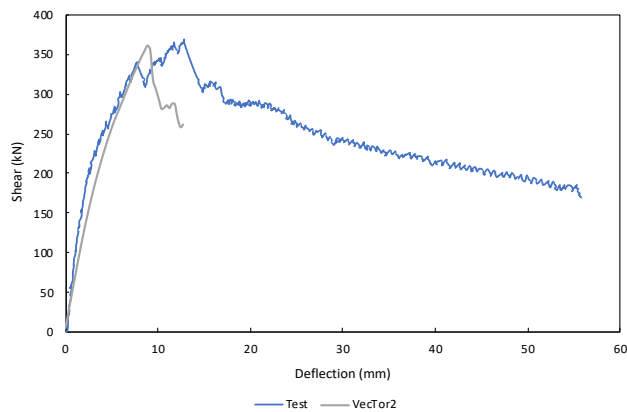
The shear-deflection responses predicted by the analysis follow the experimental results reasonably closely as can be seen in Fig. 5.14. The predictions made using VecTor2 provide reasonable estimates of the responses up to the maximum shear level, with the maximum shear for specimen M3 being slightly overpredicted.



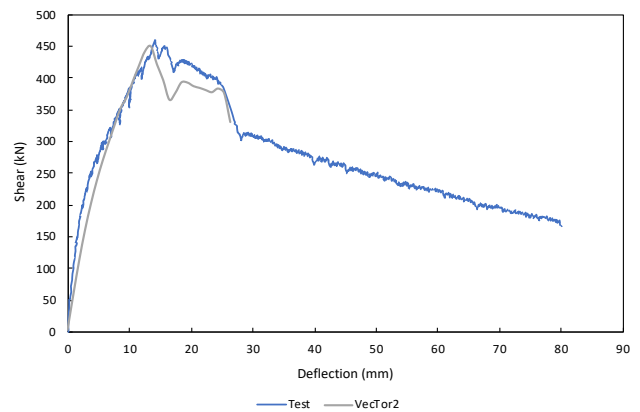
M1



M3



M2



M4

Figure 5.14: Comparison between VecTor2 predictions and experimentally determined shear deflection responses

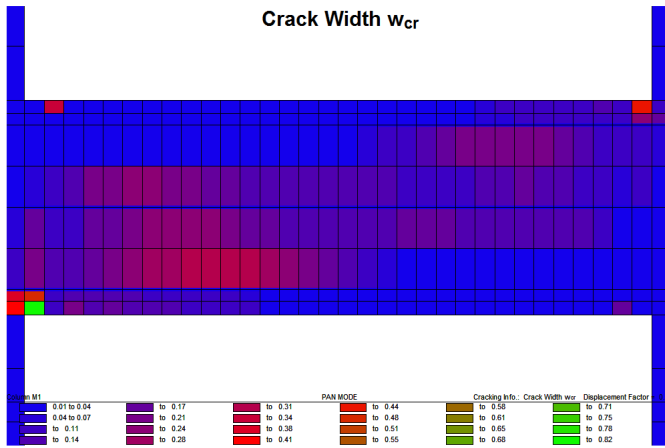
5.4.2.2 Crack Widths

It would be unreliable to compare crack widths predictions at the failure load. The specimens had undergone severe distress at this point. It was decided to pick a load level less than the failure load for all columns to compare the crack widths. Table 5.12 shows the predicted crack widths of all specimens at 80% of the maximum shear achieved during testing, V_{test} . The shear cracks observed during the experiment were read to the nearest 0.05 mm. It is important to note that it was difficult to get reliable flexural crack widths readings during testing, due to the fact that the maximum flexural cracks occurred at the interface with the wall.

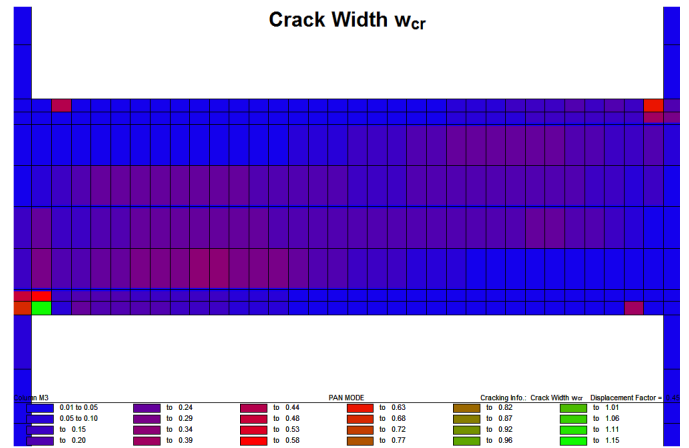
Table 5.12: Crack width predictions versus observed at $0.8V_{test}$ for all specimens

	$0.8V_{test}$ (kN)	Comparison of observed crack width vs predicted by VecTor2			
		Max Shear Crack Width (mm)		Max Flexure Crack Width (mm)	
		Observed	VecTor2	Observed	VecTor2
M1	271	0.30	0.30	0.05	0.13
M2	293	0.25	0.29	0.10	0.14
M3	310	0.20	0.29	0.15	0.17
M4	367	0.25	0.32	0.25	0.23

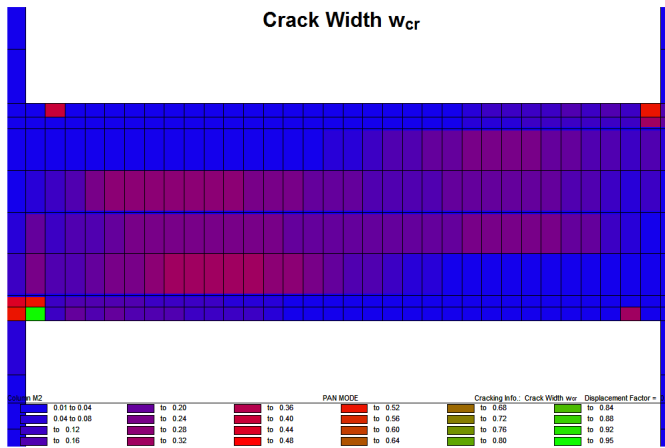
The crack width predictions are shown in Fig. 5.15. It is noted that all the predicted and measured crack widths reported in this section corresponded to a shear of $0.8V_{test}$. A maximum crack width of 0.3 mm was predicted for specimen M1 in the critical shear region on the west side and a maximum flexural crack width of 0.13 mm was predicted at this load level. During the experimental program M1 had a critical shear crack of 0.3 mm at this load level and a maximum flexural crack of 0.05 mm. A maximum shear crack width of 0.32 mm was predicted for column M4 and a maximum flexural crack of 0.23 mm as M4 saw the highest moment. For column M4, the measured critical shear crack was 0.25 mm, and the maximum measured flexural crack width was 0.25 mm.



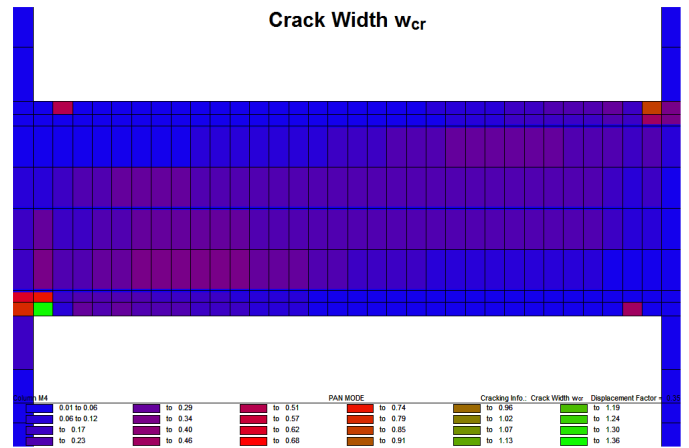
M1



M3



M2



M4

Figure 5.15: VecTor2 predicted crack widths for all specimens at a shear of $0.8V_{test}$

5.5 Experimental and Prediction Shear Strength Summary

The maximum shears for the four specimens are summarized in Table 5.13. As expected, as the amount of transverse reinforcement is increased, the shear capacity of the specimens also increases. Figure 5.16 shows a comparison of all the prediction methods considered. For the prediction models, the concrete cylinder strength for each particular specimen was used. The CHBDC (CSA, 2019) general method and Response 2000 assumed that the failure of the specimens occurred at 288 mm (effective depth, $d_v = 0.72 * h = 0.72 * 400 = 288$ mm) from the edge of the column section where the bending moment was equal to $0.312V$ ($M/V = 0.312$ m). A study of Fig. 5.16 and Table 5.12 indicates that the MCFT models (Response2000 and CHBDC General Method) provide conservative predictions.

Table 5.13: Experimental and prediction shear strengths of the specimens

		M1	M2	M3	M4
	$\rho_v f_y$ (MPa)	0.943	1.257	1.886	2.514
	Experimental (kN)	339	366	388	459
Sectional Analysis	S6-19 General Method (kN)	235	261	312	363
	S6-19 Simplified Method (kN)	156	181	231	282
	Response 2000 (kN)	256	311	385	453
	ACI 318-19 (kN)	226	250	299	349
Truss and Arch	Priestley et al. (1994) (kN)	388	433	522	615
	Pan and Li (2013) (kN)	311	337	389	443
	S6-19 General Method with V_p (kN)	313	339	391	441
NLFEA	VecTor2 (kN)	327	359	415	449

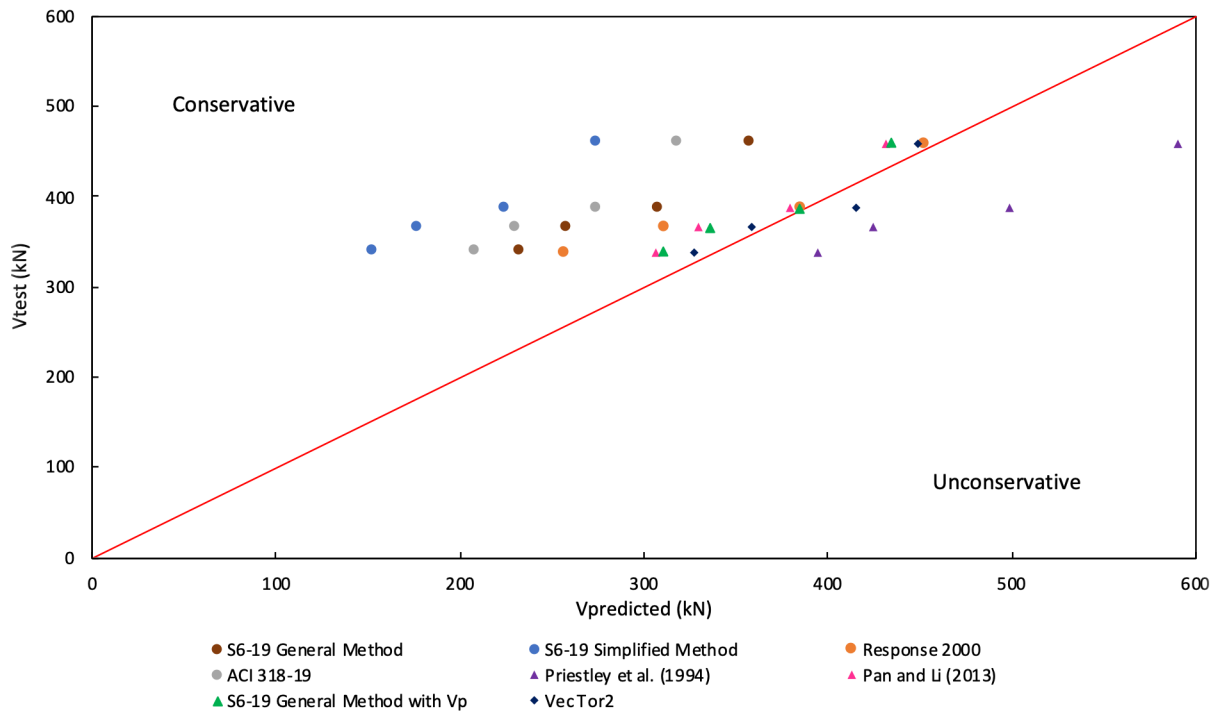


Figure 5.16: Comparison of experimental values and all prediction shear strengths models

As might be expected the most accurate estimates are made by VecTor2 with an average value of experimental/predicted of 1.00 and a coefficient of variation of 4.68%. Response 2000 has an average of 1.13 and a coefficient of variation of 13.42% while CHBDC general method has an average of 1.34 and a coefficient of variation of 7.47%. The CHBDC simplified method and ACI 318-19 expressions typically underestimated the shear capacity of the specimens with average value of experimental/predicted of 1.88 and 1.40, respectively. The S6-19 simplified method doesn't account for any benefit from the axial compression, the amount of longitudinal reinforcement or the relatively low moment-to-shear ratio and so is overly conservative. The truss and strut or arch methods, on the other hand, gave accurate estimates except for the model by Priestley et al. (1994) which overestimated the shear strength of the specimens for the reasons explained in Section 5.3.1. The model by Pan and Li (2013) had an average value of experimental/predicted of 1.06 and a coefficient of variation of 4.27%. This model is based on accounting for deformation compatibility between the truss component of the column and the arch. A phenomenon, crucially important for RC columns with small aspect ratios or high axial

loads. Finally, comparing the predictions of the CHBDC general method with and without the concrete strut. The predictions made in Section 5.3.3 were better than the predictions in Section 5.2.1.1 when the strut contribution wasn't considered. When the strut action was considered, the average experimental/shear was 1.05 compared to 1.34, and the coefficient of variation was 4.12% compared to 7.47%.

It is noted that one aspect that should be considered is the fact that, as the column deflects, the component resisting shear from strut-action decreases. Hence columns that will undergo significant deflections will reduce or eliminate this component and for larger deflections the P-delta effect must be considered.

6 Conclusions

Based on the experimental results and analysis predictions the following conclusions were made:

1. As expected, increased amounts of transverse hoops resulted in higher post-cracking stiffness, reduced crack widths at all load levels, increased shear capacities and larger deflections at maximum shear.
2. The use of the sectional design procedure in the 2019 Canadian Highway Bridge Design Code (CSA, 2019) resulted in conservative predictions of the failure shears, with an average value of $V_{test}/V_{predicted}$ of 1.34 for the general method and 1.88 for the simplified method.
3. The superposition of compressive struts on the sectional design models gave very good predictions of the maximum shear capacities. The model by Pan and Li (2013) had an average value of $V_{test}/V_{predicted}$ of 1.06. The 2019 Canadian Highway Bridge Design Code general method, with the addition of a concrete strut had an average value of $V_{test}/V_{predicted}$ of 1.05.
4. Non-linear finite element analysis using the VecTor2 software resulted in very accurate strength predictions with an average value of $V_{test}/V_{predicted}$ of 1.00. In addition, these non-linear finite element predictions provide detailed information on the complete response including deflections, steel strains, concrete strains and crack widths. These analyses also account for the strut effect directly by modelling the flow of compressive stresses in the column.
5. The strut or arch effect provided by the axial load is an important phenomenon for reinforced concrete columns with small aspect ratios or high axial loads. The sectional design approach is not capable of accounting for this effect.
6. The superposition of a strut component with the 2019 Canadian Highway Bridge Design Code general method provides a practical approach for assessing the shear strengths of shear-critical reinforced concrete columns with small aspect ratios or high axial loads, provided the columns are not subjected to significant deflections.

References

- AASHTO (1994). *AASHTO LRFD Bridge Design Specifications* (1st Edition). Washington, DC: American Association of State Highway and Transportation Officials.
- AASHTO (2014). *AASHTO LRFD Bridge Design Specifications* (7th Edition). Washington, DC: American Association of State Highway and Transportation Officials.
- ACI Committee 318 (1989). *Building Code Requirements for Reinforced Concrete (ACI 318-89) and Commentary (ACI 318 R-89)*. Detroit, MI: American Concrete Institute.
- ACI Committee 318 (2019). *Building Code Requirements for Structural Concrete (ACI 318-19)*. Farmington Hills, MI: American Concrete Institute.
- ASTM 615/615M (2016). *Standard Specification for Deformed and Plain Carbon-Steel Bars for Concrete Reinforcement*. West Conshohocken, PA: American Society for Testing and Materials.
- Bentz, E.C. (2000). *Sectional Analysis of Reinforced Concrete Members* (Doctoral dissertation, University of Toronto, Toronto). Retrieved from <https://tspace.library.utoronto.ca/bitstream/1807/13811/1/NQ49840.pdf>
- Bentz, E.C. (2001). *Response-2000 Manual*. Toronto: Department of Civil Engineering, University of Toronto.
- Bentz, E.C. (2003). *Augustus: Finite Element Post-Processor for VecTor2 and TRIX*. Toronto, ON: University of Toronto.
- Bentz, E.C. and Collins, M.P. (2006). Development of the 2004 Canadian Standards Association (CSA) A23.3 shear provisions for reinforced concrete. *Canadian Journal of Civil Engineering*, 33(5), 521-534. doi:10.1139/L06-005
- Bentz, E.C. and Collins, M.P. (2015). <http://www.ecf.utoronto.ca/~bentz/r2k.htm>. Response-2000 webpage. Last Accessed: 10/12/20.
- CEB-FIP (1978). *Model Code for Concrete Structures: CEP-FIP International Recommendations*. Paris: Comité Euro-International du Béton.

- Collins, M.P. and Mitchell, D. (1986). A Rational Approach to Shear Design – The 1984 Canadian Code Provisions. *ACI Journal*, 83(6), 925-933.
- Collins, M.P. and Mitchell, D. (1991). *Prestressed Concrete Structures*. Englewood Cliffs, NJ: Prentice Hall.
- Collins, M.P., Mitchell, D., Adebar, P., and Vecchio, F.J. (1996). A General Shear Design Method. *ACI Structural Journal*, 93(1), 36-45.
- CSA (1984). *Design of Concrete Structures for Buildings (CAN3-CSA A23.3-M84)*. Rexdale, ON: Canadian Standards Association.
- CSA (2009). *CSA G30.18: Carbon steel bars for concrete reinforcement*. Rexdale, ON: Canadian Standards Association.
- CSA (2014). *CSA A23.2-4C: Air Content of Plastic Concrete by the Pressure Method*. Rexdale, ON: Canadian Standards Association.
- CSA (2014). *CSA A23.2-5C: Slump and Slump Flow of Concrete*. Rexdale, ON: Canadian Standards Association.
- CSA (2014). *CSA A23.2-8C-14: Flexural Strength of Concrete (Using a Simple Beam with Third Point Loading)*. Rexdale, ON: Canadian Standards Association.
- CSA (2014). *CSA A23.2-9C-14: Compressive Strength of Cylindrical Concrete Specimens*. Rexdale, ON: Canadian Standards Association.
- CSA (2014). *CSA A23.2-12C-14: Making, Curing and Testing Compressive Test Specimens*. Rexdale, ON: Canadian Standards Association.
- CSA (2014). *CSA A23.2-13C-14: Splitting Tensile Strength of Cylindrical Concrete Specimens*. Rexdale, ON: Canadian Standards Association.
- CSA (2019). *Canadian Highway Bridge Design Code (CSA S6-19)*. Mississauga, ON: Canadian Standards Association.
- CSA Committee A23.3 (1994). *Design of Concrete Structures (CSA A23.3-94)*. Rexdale, ON: Canadian Standards Association.

CSA Committee A23.3 (2019). *Design of Concrete Structures (CSA A23.3-19)*. Mississauga, ON: Canadian Standards Association.

FIP Commission 3 on Practical Design. (1996). *FIP Recommendations 1996 - Practical Design of Structural Concrete*. London, UK: International Federation for Prestressing

Ichinose, T. (1992). A Shear Design Equation for Ductile R/C Members. *Earthquake Engineering and Structural Dynamics*, 21(3), 197-214.

Kim J., and Mander, J. (1999). *Truss Modeling of Reinforced Concrete Shear-Flexure Behavior* (MCEER-99-0005). Retrieved from <https://www.eng.buffalo.edu/mceer-reports/99/99-0005.pdf>

Kupfer, H. (1964). Erweiterung der Mörschschen Fachwerkanalogie mit Hilfe des Prinzips vom minimum Formänderungsarbeit (Extension to the Truss-Analogy of Mörsch using the Principle of Minimum Potential Energy). *CEB Bulletin d'Information*, No. 40.

Mitchell, D. and Collins, M.P. (1974). Diagonal Compression Field Theory – A Rational Model for Structural Concrete in Pure Torsion. *ACI Journal*, 71(8), 396-408.

Mitchell, D., Huffman, S., Tremblay, R., Saatcioglu, M., Palermo, D., Tinawi, R. and Lau, D. (2013). Damage to Bridges due to the February 27, 2010 Chile Earthquake. *Canadian Journal of Civil Engineering*, 40(8), 675-692, 10.139/12012-045.

OHBDC. (1991). *Ontario Highway Bridge Design Code* (3rd Edition). Downsview, ON: Ministry of Transportation.

Pan, Z., and Li, B. (2013). Truss-Arch Model for Shear Strength of Shear-Critical Reinforced Concrete Columns. *Journal of Structural Engineering*, 139(4), 548-560.

Paulay, T., and Priestley, M. (1992). *Seismic Design of Reinforced Concrete and Masonry Buildings*. New York: Wiley.

Priestley, M., Verma, R., and Xiao, Y. (1994). Seismic Shear Strength of Reinforced Concrete Columns. *Journal of Structural Engineering*, 120(8), 2310-2329.

- Vecchio, F.J. (2000). Disturbed Stress Field Model for Reinforced Concrete: Formulation. *ASCE Journal of Structural Engineering*, 126(9), 1070-1077.
- Vecchio, F.J. (2018). VecTor2 (Version 4.2) [Software]. Retrieved from <http://www.civ.utoronto.ca/vector>
- Vecchio, F. J. and Collins, M. P. (1986). The Modified Compression-Field Theory for Reinforced Concrete Elements Subjected to Shear. *ACI Journal*, 83(2), 219-231.
- Vecchio, F.J. and Collins, M.P. (1988). Predicting the Response of Reinforced Concrete Beams Subjected to Shear Using Modified Compression Field Theory. *ACI Structural Journal*, 85(3), 258-268.
- Walraven, J.C. (1981). Fundamental Analysis of Aggregate Interlock. *Proceedings of the American Society of Civil Engineers*, 107(11), 2245-2270.
- Watanabe, F., and Ichinose, T. (1991). Strength and Ductility Design of RC Members Subjected to Combined Bending and Shear. *Workshop on Concrete Shear in Earthquake*, (pp. 429-438). University of Houston, Houston, Tex.
- Watanabe, F., and Kabeyasawa, T. (1998). Shear Strength of RC Members with High-Strength Concrete. *ACI Special Publication*, 176(17), 379-396.
- Wong, P. S. (2002). *User Facilities for 2D Nonlinear Finite Element Analysis of Reinforced Concrete*, M.A.Sc. Thesis. Toronto, ON: Department of Civil Engineering, University of Toronto.
- Wong, P. S., Vecchio, F. J., and Trommels, H. (2013). *VecTor2 & FormWorks User's Manual (Second Edition)*. Retrieved from <http://www.civ.utoronto.ca/vector>
- Yoshimura, M., and Nakamura, T. (2003). Axial Collapse of Reinforced Concrete Short Columns. *The 4th U.S.-Japan Workshop on Performance-Based Earthquake Engineering Methodology for Reinforced Concrete Building Structures* (pp. 187-198). Toba, Japan: Pacific Earthquake Engineering Research Center.